UNIVERSIDADE DO ALGARVE

FACULDADE DE CIÊNCIAS E TECNOLOGIA

DESENVOLVIMENTO DE UM DETECTOR DE ALTA RESOLUÇÃO PARA IMAGEM MÉDICA COM RADIAÇÕES IONIZANTES

(Tese para a obtenção do grau de doutor no ramo de Física, especialidade em Física Médica)

PATRICK EMMANUEL SOUSA

Orientadora:
Doutora **Maria da Conceição Abreu e Silva**
Professora Catedrática da Faculdade de Ciências e Tecnologia da Universidade do Algarve.

Co-Orientador:
Doutor **Pedro Fernando Paulo Rato Mendes**
Investigador do Centro de Investigações Energéticas, Ambientais e Tecnológicas – Espanha.

Constituição do Júri:

Presidente: Reitor da Universidade do Algarve.

Vogais: Doutor **Rui Ferreira Marques**, Professor Catedrático da Faculdade de Ciências e Tecnologia da Universidade de Coimbra;
Doutor **Carmelo D'Ambrósio**, Investigador na Organização Europeia para a Pesquisa Nuclear – Suiça;
Doutor **João Manuel Coelho dos Santos Varela**, Professor Associado com Agregação do Instituto Superior Técnico da Universidade Técnica de Lisboa;
Doutor **Henrique Leonel Gomes**, Professor Associado da Faculdade de Ciências e Tecnologia da Universidade do Algarve;
Doutor **Luís Filipe dos Santos Garcia Peralta**, Professor Auxiliar com Agregação da Faculdade de Ciências da Universidade de Lisboa;
Doutora **Carla Maria Quintão Pereira da Silva**, Professora Auxiliar da Faculdade de Ciências e Tecnologia da Universidade do Algarve.

FARO
(2007)

UNIVERSITY OF ALGARVE

FACULTY OF SCIENCES AND TECHNOLOGY

DEVELOPMENT OF A HIGH RESOLUTION DETECTOR FOR MEDICAL IMAGING WITH IONIZING RADIATION

(A dissertation submitted in candidacy for the degree of Doctor of Physic)

PATRICK EMMANUEL SOUSA

FARO
(2007)

NOME: Patrick Emmanuel Sousa
FACULDADE: Faculdade de Ciências e Tecnologia
ORIENTADORA: Maria da Conceição Abreu e Silva
CO-ORIENTADOR: Pedro Fernando Paulo Rato Mendes
ANO: 2007
TÍTULO DA TESE:
Desenvolvimento de um detector de alta resolução para imagem médica com radiações ionizantes

RESUMO

Este trabalho apresenta o desenvolvimento de um protótipo de uma câmara gama projectado de forma a demonstrar as suas capacidades em imagem bidimensional de alta resolução. Em particular, a imagiologia molecular e a visualização de órgãos internos de pequenos animais são considerados.

O sistema proposto é um dispositivo compacto que oferece o potencial para uma resolução inferior ao milímetro. O sistema consiste numa câmara optoelectrónica híbrida – o tubo ISPA (*Imaging Silicon Pixel Array*) acoplado a uma electrónica específica. O tubo, originalmente desenvolvido para propósitos de física de altas energias no CERN, foi testado com sucesso no campo da imagiologia com radiação gama de baixa energia utilizando fontes radioactivas, demonstrando capacidades reais quer em resolução espacial quer em energia.

O primeiro sistema electrónico de leitura desenvolvido foi implementado para validar o conceito de imagem bidimensional. Uma das principais desvantagens deste sistema era seu tamanho e devido às restritas exigências necessárias de modo a empregar este tipo de detector em aplicações biomédicas por não físicos, um novo sistema de leitura compacto e apropriado foi projectado e construído.

Neste trabalho é apresentado uma nova geração em electrónica de leitura para o controlo e o processamento em tempo real de imagens com o tubo ISPA, que conduziu ao desenvolvimento de uma ferramenta importante em imagiologia digital.

Palavras-chave: Tubo ISPA; Fotodetector híbrido; Imagiologia gama; SPECT; Medicina Nuclear; Mini câmara gama.

TÍTULO DA TESE EM INGLÊS:
Development of a high resolution detector for medical imaging with ionizing radiation

ABSTRACT

This work presents the development of a prototype gamma camera system designed and built to demonstrate its capabilities in 2D high-resolution imaging. In particular, molecular and small-animal's organs imaging are considered.

The system proposed is a compact device that offers the potential for submillimeter resolution. It consists of a position sensitive photon detector (ISPA-tube) based on hybrid technology. The ISPA (Imaging Silicon Pixel Array)-tube, originally developed for high-energy physics purposes at CERN, has been successfully tested in the field of gamma ray imaging for low-energy photons using radioactive sources, demonstrating real capabilities in both spatial and energy resolution.

The system readout was first implemented to validate the concept of bidimensional imaging. One of the major drawbacks of this system was its size and due to the tight requirements of compactness necessary to employ this detector for biomedical applications, a new dedicated and compact readout system was designed. We report this new generation electronics for full control and real-time processing of the ISPA-tube.

This work has led to the development of an important tool in gamma detection and consequently to an improvement in imaging capabilities.

Keywords: ISPA-tube; Hybrid photon detector; Gamma imaging; Single-Photon counting; Nuclear Medicine; Mini gamma camera.

Acknowledgements

I wish first to express my sincere gratitude to Professor Maria Conceição Abreu, who supervised me in this research work. Her guidance, encouragement and strong support in all phases of this work were essential to make it possible. I am also grateful to her for giving me the opportunity to serve as a teaching assistant and, most of all, to show me the perspectives of the non-academic world, opening the gate for me to start a business on my own.

I thank my thesis coordinator, Pedro Rato Mendes, with whom I took my first steps at CERN in 1999 on the road to this research field. I thank him for his care and patience in the revision of this manuscript as well as all the physics I learnt from him over the past years.

Much of the material included in this thesis is the result of a most fruitful collaboration and participation of many individuals. I wish to thank the Department of Physics of the University of Algarve and the Laboratory for Instrumentation and Particle Physics (LIP) for research laboratory facilities. This work was supported in part by the National Institute for Nuclear Physics (INFN) of Rome3, Italy, the CERN in Geneva, Switzerland, and the Portuguese Foundation for the Science and the Technology (FCT) from the project POCTI/FNU/43672/2002 coordinated by Professor Luís Peralta. I thank him and Catarina Ortigão who were principally responsible for the Monte Carlo simulation based on GEANT3 presented in this work.

I especially acknowledge Ettore Rosso and Carmelo D'Ambrosio for their friendly cooperation, for introducing me to the ISPA project and for providing me with all the necessary conditions at CERN. I am very grateful to Federico Cindolo for the experienced advice concerning this work in all technical aspects. Their insight of the tube operation and their elegant ideas were very helpful as well as their comments and suggestions. They furnished the resources to complete this work.

I am thankful to the research group at the Engineering Faculty of INFN-Rome3 headed by Professor Francesco De Notaristefani, namely Valentino Orsolini Cencelli, Enrico D'Abramo and Giulia Hull for their valuable assistance and fundamental contribution. I especially thank Enrico D'Abramo for his massive efforts in supporting the electronic readout of this work. Our work together was a most enjoyable experience for me. Above all, I thank him for his friendship and great sense of humour.

During my PhD candidacy, I have been fortunate to share the laboratory facilities with a multitude of other people, too numerous to mention by name. I would like to express a sincere debt of gratitude to them, who with their friendship have helped me to take all the steps needed to reach this goal. Mostly to Dário Passos who was always there when needed and to Sónia Rodrigues who also helped me with GEANT4 simulation results presented here.

I acknowledge with thanks the support and interest of my family in this thesis, especially Natália Laranjinha. In particular my wife, Marlene, and my parents, Albino and Valentina, were a source of cheerfulness and motivation during this work. To them is dedicated this thesis.

I also address my thanks to Mr. Alan Frank Brigden for carefully and patiently revising the English language of the manuscript.

This material is based upon work supported by a PhD grant from the Portuguese Foundation for the Science and the Technology (FCT) under reference number SFRH/BD/6611/2001.

Contents

Chapter 1

Introduction 1

1.1. Overview 1

1.2. Objectives and contributions 2

1.3. Outline of this thesis 3

References 4

Chapter 2

Nuclear Medicine Imaging 5

2.1. Use of radioisotopes 5

2.2. Nuclear imaging techniques 8

2.3. Semiconductor cameras 10

2.3.1. The ISPA-tube 11

2.3.2. Worldwide cameras 14

2.4. Applications for the ISPA-tube 19

2.4.1. Radiotracers studies in small animals 19

2.4.2. Intraoperative radioguided surgery 19

2.4.3. Thyroid imaging 20

2.4.4. Scintimammography 20

References 21

Chapter 3

Properties of the ISPA-Tube 23

3.1. Collimator 23

3.1.1. Mechanical properties 24

3.1.2. Geometric properties 25

3.2. Crystal scintillator 28

3.2.1. Detection properties 31

3.2.2. YAP:Ce crystal scintillator operating principles 33

3.2.3. Monte Carlo simulations 35

3.3. Photocathode 39
3.3.1. Optical properties 40
3.3.2. Dark current 44
3.3.3. S20 photocathode operating principles 46
3.4. Electrostatic tube 48
3.4.1. Trajectories in the electric field 51
3.5. Silicon anode 52
3.5.1. The Omega3/LHC1 sensor chip 54
3.5.2. Photoelectron response 56
3.5.3. Spatial resolution 61
3.6. Readout chip 61
3.6.1. The Omega3/LHC1 readout chip 62
3.6.2. Architecture and operation 65
3.7. Summary discussion 68
References 70

Chapter 4

Readout Electronics System 75

4.1. The old readout system 75
4.2. The new prototype system 78
4.2.1. Front-end card 79
4.2.2. ISPA back card 79
4.2.3. Piggy back board 81
4.2.4. S9007 board 82
4.2.5. USB card 83
4.3. Logic programming 84
4.4. Summary discussion 86
References 86

Chapter 5

Application Software 89

5.1. The visual basic interface program 89
5.1.1. The protocol handler 90
5.1.2. The settings panels 92

5.1.3. The data acquisition panel 93
5.1.4. The data analysis panel 94
5.1.5. The support panel 95
5.2. Position estimation and image reconstruction 98
5.3. Wide area scanning system 102
5.4. Summary discussion 104

Chapter 6

ISPA-Tube Performance 105

6.1. Laboratory setup 105
6.2. Radioactive source measurements on silicon sensor 107
6.2.1. Leakage current 107
6.2.2. Sensor depletion voltage 108
6.2.3. Electrostatic tube high voltage adjustment 109
6.2.4. Energy spectrum analysis 110
6.3. Electrical measurements on readout chip 114
6.3.1. Detector noise offset 114
6.3.2. Timing calibration 115
6.3.3. Threshold measurements 116
6.4. Position measurements 118
6.4.1. Setup procedure 118
6.4.2. Cluster size and spatial resolution 121
6.5. Image comparison evaluation 124
6.6. Summary discussion 129
References 131

Chapter 7

Discussion and Conclusion 133

7.1. Conclusion 133
7.2. Scientific research contributions 134
7.3. Future developments 135
7.4. Partnership 136

List of figures

Figure 2-1: Two nuclear medicine images examples. (left) Planar bone scan of a 17 year old basketball player with persistent foot pain. Tc-99m was administrated intravenously. The bone scan shows a hot spot (arrow) in the left foot representing a stress fracture that is too small to be seen on a conventional x-ray exam; (right) Planar gamma imaging/x-ray combination image of a mouse [JLab, 2004]. The radiotracer (Tc-99m) is trapped in cells containing the transferred gene in the lungs and liver. 9

Figure 2-2: (left) Photograph of the ISPA proximity-focused tube that creates 1:1 images; (right) Photograph of the ISPA cross-focused tube that creates 4:1 images. In both designs, the tube is connected to a small printed circuit board with a flat cable connection to the readout electronics. For a correct/safety utilization procedure, the tube is mounted inside a protective envelope to avoid light entrance and electrical discharge. 12

Figure 2-3: Operating principle of the ISPA proximity tube. The photons generated in the scintillating detector are converted at the photocathode into photoelectrons and accelerated onto the silicon anode. The global analogue signal taken from the detector plane provides information on the total charge created in the detector. This signal is used to operate the tube in the self-triggering mode. The binary read-out of the pixel electronics provides position information and allows 2-D imaging. 13

Figure 2-4: Medipix2 hand-held probe head (with the collimator removed) connected to a small footprint printed circuit board, with flat cable connection to the readout electronics. The chip is bonded to a CdTe pixel detector. Extracted from [P. Russo et al., 2003]. 15

Figure 2-5: (left) Photograph of the per-operative compact imager (POCI); (right) Application test of the camera in a radio-guided operative cancer surgery.....15

Figure 2-6: (left) Photograph of the eZ-SCOPE AN portable gamma camera; (right) Imaging application of gene expression in a representative mouse. 16

Figure 2-7: Image comparison between (b) the eZ Scope (CdZnTe) camera and (c) a standard Anger camera (NaI). Data are produced by using (a) a 1.7 mm hollow phantom with a radioactivity concentration of 0.74 MBq/cc of Tc-99m. Collection times are 5 s for (b) and 10 min for (c). 16

Figure 2-8: (a) Photograph of the MGC500 mini gamma camera; (b) Image comparison of a 1 mm hollow S-shape phantom between the MGC500 (left) and a conventional gamma camera (right). Data are produced with a radioactivity concentration of 30 MBq of Tc-99m. Collection time is 2 s in each case. 17

Figure 2-9: (a) Photograph of the Digirad 2020tc Imager; (b) Comparison of images taken with the Digirad 2020tcTM (left) and a conventional gamma camera (right) with comparable collimators and imaging times. 18

Figure 3-1: Photograph and technical design of the ISPA parallel-hole tungsten collimator. The septa is 60 μm thick. 25

Figure 3-2: Optical photon spectra (middle column) and image reconstruction (right column) of a 122 keV point-source using three different tungsten collimators (left column). The collimator thickness and the source-collimator distance were fixed at 1 cm. The hole diameter is 0.6 mm. The image reconstruction with the parallel hole collimator presents a cross shape due the non-absorption of the radiation through the septa. 27

Figure 3-3: X-ray energy spectrums of a cadmium-109 point-source captured using XR-100T-CZT detector with and without the ISPA parallel-hole tungsten collimator (rippled foils). Integrals of both peaks have been calculated over the 22 keV energy peak and a ratio of 1:72 has been measured. 27

Figure 3-4: Linear attenuation coefficients (cm^{-1}) for standard YAP:Ce scintillator. Extracted from [R. Pani et al., 1995]. 28

Figure 3-5: Electronic bands structure of inorganic crystals. Extracted from [C. Ortigão, 2003]. 30

Figure 3-6: Optical transmittance of YAP:Ce (0.37 mm, 52 mm and 104 mm) single crystal scintillators, adapted from [F. de Notaristefani et al., 1998]. The emission spectrum (1), as reported in [C. D'Ambrosio et al. 2000] for a 2 mm-thick YAP:Ce crystal, is shown in relative scale of intensity. 32

Figure 3-7: Top view of the ISPA detector. The YAP:Ce crystal coated with aluminium in an 'O' ring shape (19 mm-inner diameter) is visible. This aluminium coating extends to the lateral side. About 70% of the incident window (front + lateral sides) is aluminium coated. 33

Figure 3-8: Absorption Efficiency of YAP crystals. Extracted from [Bicron YAP:Ce Brochure, @2002 Saint-Gobain Industrials Ceramics & Plastics, Inc]. 34

Figure 3-9: Energy resolution as a function of photon energy [C. Ortigão, 2003]. Red dots corresponds to experimental results taken with ^{109}Cd and ^{241}Am radioactive sources.....36

Figure 3-10: Spatial resolution as a function of the YAP crystal thickness for 122 keV energy photons [C. Ortigão, 2003]. 37

Figure 3-11: Sensitivity as a function of the YAP crystal thickness for 122 keV energy photons [C. Ortigão, 2003]. 37

Figure 3-12: Spatial resolution as a function of the distance radius of the source position relative to the centre of the crystal [C. Ortigão, 2003]. 38

Figure 3-13: Intensity profile of the light photons that penetrates into the photocathode for (left) one and (right) 8771 absorbed gamma photons of 60 keV with centred normal incidence. The fraction of light per unit of energy that goes through the interface scintillator-photocathode and meets the active region of the silicon detector is almost 7 ph/keV. Courtesy of Sónia Rodrigues [Sónia Rodrigues, 2005].....38

Figure 3-14: Alkali photocathode band model. EG corresponds to the forbidden-band gap energy and Ea is the electron affinity. Extracted from [Photonis PMT's application book, 2002] 39

Figure 3-15: Quantum efficiency of the S20-photocathode evaporated on a Quartz window and on the YAP:Ce window (measured by DEP company). 42

Figure 3-16: Radiant sensitivity of the S20-photocathode evaporated on a Quartz window and on the YAP:Ce window. 43

Figure 3-17: Absorption, transmission, reflection and spectral sensitivity with wavelength. Extracted from [B. P. Varma and C. Ghosh, 1973]. 44

Figure 3-18: Number of dark current pulses per second per centimeter squared as function of temperature for S20-photocathode. Extracted from [Photonis PMT's application book, 2002]. 45

Figure 3-19: Absorption coefficient α as a function of the wavelength λ of the incident photons for the S20 photocathode. Extracted from [Photonis PMT's application book, 2002]. 46

Figure 3-20: Transmission efficiency as a function of the thickness of the photocathode S20 for an incident light wavelength of λ = 370 nm.....47

Figure 3-21: (left) Photograph of the silicon detector mounted and wire-bonded onto the ceramic carrier manufactured by Kyocera in Japan. It is of the Pin Grid Array (PGA) type. An O-ring plate/cover (right) is then glued onto the ceramic carrier for integration on the electrostatic tube and for grounding purposes.....49

Figure 3-22: Distribution of the equipotential lines along a simple design reproducing of the ISPA proximity focussing tube. Maxwell S-V version 3.1.04. 49

Figure 3-23: Photograph of the proximity focusing tube and the polypropylene casing. This HV shield casing has a centered hole to adapt the collimator. Three springs are visible around it and they are useful to lean the collimator on the scintillator. The groove cavity is for the tube and collimator high voltage cables. 50

Figure 3-24: Lambertian distribution of photoelectron intensity 51
Figure 3-25: Photoelectron spatial deviation at silicon anode as function of photocathode surface emission angles. For a maximum emission angle of $\varphi = 90^{o}$, the spatial deviation is 225 μm. 52

Figure 3-26: (top) Photograph of the OMEGA3/LHC1 sensor; (bottom) Photograph of the pixel cells. 55

Figure 3-27: Cross sectional view of the sensor chip (sizes not to scale) 55

Figure 3-28: Current-voltage characteristics of the reverse biased sensor chip. Extracted from [Iztok Ljubljana, 2000]. 56

Figure 3-29: Backscattering distribution of 20 keV incident electrons from the silicon detector back-plane. The total backscattered energy is 2.1 keV. Simulated with CASINO version 2.42. 57

Figure 3-30: Intensity distribution of the transmitted energy through the 500 nm-thick ohmic layer of the silicon detector back-plane (CASINO version 2.42). The results are normalized for 1 electron of 20 keV. 58

Figure 3-31: Interaction volume in silicon at 20 keV, simulated with CASINO version 2.42. Red lines correspond to backscattered electrons. The absorption energy varies from 20 keV (yellow) to 3.62 eV (blue). An initial electron cloud of $r_i \sim$ 2.5 μm lateral spread radius is formed. 58

Figure 3-32: Photoelectrons density depth profile along the incident track direction, simulated with CASINO version 2.42. 59

Figure 3-33: Maxwell electric field calculation for the reverse biased (70V) OMEGA3/LHC1 pixel detector with the appropriate geometry, electrode pattern and potentials. A schematic drawing of the final cloud radius due to the holes diffusion process is presented. Besides the detector thickness, sizes are to scale. 60

Figure 3-34: (Left) Hybrid pixel detector. (Right) : Photograph taken with a scanning electron microscope of a column of solder bumps (ϕ 28 μm) on the readout cell after reflow. 62

Figure 3-35: Layout and photograph of a single readout cell. The bump pad is the octagonal on the left. 62

Figure 3-36: Block diagram of the Omega3/LHC1 readout electronics in a single cell. 63

Figure 3-37: (Left) Photograph of an Omega3/LHC1 pixel detector readout chip of size 8.72 × 9.12 mm^2, covering an active area of 8 × 6.35 mm^2 that comprise a matrix of 12 × 16 pixel cells with dimension 50 × 500 μm^2; (Right) Photograph of the silicon detector bump bonded onto the readout chip (ref. CERN-EX-0206005). As referred to in Sub-Chapter 3.4, this

assembly is mounted and wire-bonded onto a Pin Grid Array (PGA) ceramic carrier. At the bottom of the chip, where the chip periphery is located, two rows of wire-bonding pads are visible, which provide the connections to the external data and bias lines. Refer to schematics on Figure 3-34 for structural overview. 66

Figure 4-1: Photograph of the existing ISPA-tube imaging setup at CERN. (A) HP workstation; (B) analog NIM modules; (C) VME readout modules; (D) tube high voltage regulated DC power supplies; (E) pulse generator; (F) Cooling fan; (G) tube anode power supply and readout card power voltages; (H) multichannel analyser; (I) RD19/Omega3 readout card; (J) ISPA proximity focusing tube mounted on a test board; (K) tungsten collimator; (L) preamplifier; (M) tube housing. 76

Figure 4-2: Schematics overview of the VME based setup for the Omega3/LHC1 pixel detector operation with radioactive sources (left) and with electrical test-input signals (right). Not to scale. 77

Figure 4-3: Complete Omega3/LHC1 readout sequence of one pixel in a column with the required timing for the signals test and strobe. The strobe signal is a NIM signal of approximately 2 μs, the test pulse has a length of 12 μs and a height of ~5V. 77

Figure 4-4: Schematic overview of the setup with a block-readout architecture. Not to scale. 78

Figure 4-5: (left) ISPA front-end card; (right) Omega3/LHC1 chip test card..... 79

Figure 4-6: Photograph of the ISPA Back Board. The PCB has been commercially purchased and the surface mounted device (SMD) has been achieved at the INFN laboratories of Rome 3, in Italy. 80

Figure 4-7: Photograph of the PCB for the new ISPA front-end card. 80

Figure 4-8: Photograph of the Piggy Back Board. 82

Figure 4-9: Photograph of the S9007 Board. 83

Figure 4-10: Photograph of the USB card. 84

Figure 4-11: Photograph of the Omega3/LHC1 chip test card (see figure 4.5) connected with the logic analyzer probes. 85

Figure 4-12: View of the logic analyser's display (Philips PM3580) during a chip readout of the mask and test flip-flop memories (operation mode 3). The left column shows the designation of the probes connected on the Omega3/LHC1 chip test card (refer to Tables 3.6 and 3.7) and the right column shows the corresponding level state at the X vertical line. Only even data lines (D0:D16) are probed. 85

Figure 5-1 Diagram of the application software for the ISPA-tube prototype system. 89

Figure 5-2: Serial data packet format. 90

Figure 5-3 Screenshot of the settings option menu. The chart shows an automatic scan of the efficiency detection versus the threshold voltage. All the chip control bias voltages can be tuned stably and effectively in the same way. 92

Figure 5-4: Screenshot of the data acquisition option menu. The chart shows bad pixels that are masked. 93

Figure 5-5: Screenshot of the data analysis option menu. The 2D/3D contour maps shows the reconstructed image obtained by processing the centre of gravities of 10000 events. Each event corresponds to a 2D binary map of hit pixels 94

Figure 5-6: Screenshot of the support's main panel. 96

Figure 5-7: Screenshot of the support's maps panel. 96

Figure 5-8: Screenshot of the support's voltages panel 97

Figure 5-9: Screenshot of the support's images panel 97

Figure 5-10: (a) Raw image obtained from one single photon event in the ISPA tube (16 x 128 pixels). A total of 200 hits are registered, where 103 pixels (red colour) are tagged noisy; (b) Raw image obtained after removing noisy pixels. A total of 97 hits is registered, where 24 pixels are considered isolated; (c) Centre of gravity position of the 73 remaining pixels; (d) Distribution of the variance of the hit pixels around the centre of gravity, assuming a Gaussian probability density distribution of 99.7% ($\pm 3\sigma_{X,Y}$) 99

Figure 5-11: Position estimation of a single photon event convolved with a Gaussian point spread function. Projections along X and Y axes are also shown. 101

Figure 5-12 Fluxogram of the methodology used in the image reconstruction analysis. 101

Figure 5-13: Image reconstruction of a 1 mm hole collimator, processed with a different number of single photon events. 102

Figure 5-14: Photograph of the ISPA setup with the XY positioning table. 103

Figure 5-15: Screenshot of the XY positioning control module. This form is a call out module from the "multiple image" button on the data acquisition panel (refer to Figure 5.4). It allows setting all the parameters needed to achieve a mosaic image of multiple sizes of the detector active region. Each axis

can be individually controlled with regard to its speed motor, rotational direction, step size and step mode (full/half). 103

Figure 6-1: (left) Schematic overview of the laboratory setup; (right) Photograph of the setup mounted at the UALG physics laboratory. A radioactive source alignment centred on top of the test detector is being performed. 106

Figure 6-2: I-V characteristics of the test detector. 107

Figure 6-3: Test detector (left) CV and (right) RV measurements at 1 kHz frequency. The full depletion occurs at 15 V. 108

Figure 6-4: ISPA tube pixel chip response versus sensor bias voltage at 20 kV high voltage. Around 10% of the pixels are noisy or corrupted. 109

Figure 6-5: ISPA-tube pixel chip response versus high voltage applied with the sensor in full depletion mode. Around 10% of the pixels are noisy or corrupted. 110

Figure 6-6: (left) Cadmium-109 spectrum. The combined X-ray peak (21.9, 22.1 and 24.9 keV) with the intensity based on the yield ratio is clearly visible. With an energy of the incoming X-rays greater than the absorption edge of the crystal scintillator, a characteristic X-ray from the YAP:Ce window is produced; (right) Americium-241 spectrum. An energy resolution of 22.6% FWHM at 59.5 keV most probable energy value was calculated. 111

Figure 6-7: (left) Cobalt-57 spectrum of a weak source; the gamma emission line corresponding to 122 keV is located around channel 4500. Clearly visible is the Compton edge due to 122 keV photons scattering in the detector before escaping; (right) Europium-152 spectrum. A distorted shape of the combined X-ray lines (39.5 and 40.1 keV) in superposition with the Compton edge due to 122 keV photons scattering is visible. 111

Figure 6-8: X-ray fluorescence of (a) Rubidium, (b) Molybdenum, (c) Barium and (d) Terbium. The gamma emission peak of the Americium excitation source is visible in some spectra. 112

Figure 6-9: Zoom of the spectral distribution of the (left) Cd-109 radioactive source and the (right) Mo-42 XRF; Photoelectron peaks are visible with a minimum of 2 photoelectrons just above the electronic noise cut off. 112

Figure 6-10: Photoelectron numbers versus the energies of total absorption peaks for several gamma and X-ray emissions. 113

Figure 6-11: Variation of the average firing pixels as a function of the amplitude of the threshold voltage for an offset measurement at room temperature. Neither a pulse nor charge was injected at the test input. 114

Figure 6-12: Required timing for the signals test, strobe, delay output and clock out. 115

Figure 6-13: Threshold calibration measurements for an applied voltage steps at the test input of one row. Starting from the offset threshold value, the threshold is moving linearly until ~6000 e- and then the dependence becomes exponential. 116

Figure 6-14: (left) test-pulse response curve of a single readout cell; (right) Numerically differentiated response curve data with Gaussian data fit. 117

Figure 6-15: Experimental schema of the position measurement setup with details of the two-hole phantom lead collimator. With this configuration setup, the extrinsic spatial resolution can be studied. 119

Figure 6-16: Spectrum of the ^{241}Am. The full energy peak corresponding to 60 keV centers at N_{meas} = 104 photoelectrons. 119

Figure 6-17: (left column) Sum of all the matrix (16 × 128) hit patterns (20 000 events) acquired using the tungsten collimator; (right column) Reconstructed image of the two-hole phantom (~0.35 mm in diameter and distant of ~1 mm). The image (8.0 × 6.4 mm^2) is obtained by accumulating the center-of-gravity of 20 000 gamma events. Image pixel size: 62.5 × 50.0 μm^2 120

Figure 6-18: (left column) Sum of all the matrix (16 × 128) hit patterns (20 000 events) acquired without using the tungsten collimator. The phantom is placed directly on top of the crystal scintillator. The mask map of unwanted pixels that corresponds to the white pixels on the bottom image is visible. 171 pixels are registered as noisy; (right column) Reconstructed image of the two-hole phantom (~0.35 mm in diameter and distant of ~1 mm). The image (8.0 × 6.4 mm^2) is obtained by accumulating the center-of-gravity of 20 000 gamma events. Image pixel size: 62.5 × 50.0 μm^2 120

Figure 6-19: Number of hits per gamma event. The average number N_{hit} is 67 hits/event. 121

Figure 6-20: Centre of gravity residuals projection along the X-axis. The FWHM value is indicated. 122

Figure 6-21: Intensity distribution of the two-hole phantom image taken along X and Y axis. 123

Figure 6-22: Intensity distribution of the two-hole phantom taken along line A. 123

Figure 6-23: (left) Photographs of the setup using the Anger camera. The collimator is centred and aligned on top of a one of the 59 photomultiplier tubes symbolized with circle marks. A small container with the radioactive substance inside is placed on top of the collimator; (right) Photographs of the setup using the ISPA camera. The two 1 mm distant holes on the lead phantom are visible. 124

Figure 6-24: Spectrum of the Tc-99m isotope obtained with the Anger gamma camera SPECT. K-lines x-ray fluorescence of the lead phantom are visible.....125

Figure 6-25: Phantom image taken with the conventional Anger camera SPECT. Image acquisition parameters: Tc-99m (48 MBq), 5 minutes static, 512 × 512 matrix, image pixel size = 0.6 × 0.6 mm^2, FoV = 307.2 × 307.2 mm^2, counting rate = 2800 cpm. 125

Figure 6-26: Spectrum of the Co-57 source obtained with the ISPA gamma camera.....126

Figure 6-27: Phantom image taken with the ISPA gamma camera. Image acquisition parameters: 10 minutes static, 128 × 128 matrix, image pixel size = 62.5 × 50.0 μm^2, FoV= 8.0 × 6.4 mm^2, counting rate = 1400 cpm.....126

Figure 6-28: Image comparison between (top) a standard Anger camera (NaI) and (bottom) the ISPA-tube. Data are produced by using a two-hole lead phantom of ~0.35 mm distant of ~1 mm. Collection times are 5 minutes equivalent. The number of gamma events detected is 14000 counts for the SPECT system and 2800 counts for the ISPA system. Note that the profile intensities in X- and Y- axis of the two images are not related to single gamma events. 128

List of tables

Table 2-1: Common radioisotopes used in Nuclear Medicine imaging. 7

Table 2-2: Summary of the characteristics of different semiconductor gamma cameras. 18

Table 3-1: Sensitivity, spatial resolution and energy resolution of the ISPA parallel-hole tungsten collimator (rippled foils). Monte Carlo simulation results were obtained using a 122 keV point source photons placed at 1 cm from the collimator. Four collimator thicknesses were used. 26

Table 3-2: Important properties of some single crystal scintillators. Adapted from [Hamamatsu Photonics KK PMT's Handbook, p.88, 1999] and [Bicron Crystals Catalog, @2005 Saint-Gobain Industrials Ceramics & Plastics, Inc]. 29

Table 3-3: Typical characteristics of standard photocathodes. Adapted from [Hamamatsu Photonics KK PMT's handbook, 1999]. Type of window 1. Borosilicate 2. Synthetic silica 3. UV 4. MgF2 42

Table 3-4: Properties of silicon diodes. Extracted from [C. D'Ambrosio and H. Leutz, 2003]. 53

Table 3-5: Characteristics of the sensor chip processing for the OMEGA3/LHC1 detector [Iztok Ljubljana, 2000]. 56

Table 3-6: Different bias voltages and digital signals required for the Omega3 chip operation. 64

Table 3-7: The Omega3/LHC1 readout chip operation modes. 67

Table 6-1: Overview of the equipment models available in the ISPA laboratory setup. 106

Table 6-2: (left) gamma sources; (right) Americium-241 XRF (X-ray fluorescence) source. 110

Table 6-3: Bias voltages for the tube operation. 119

Acronyms

ADC	– **A**nalog-to-**D**igital **C**onverter
ALICE	– **A** **L**arge **I**on **C**ollider **E**xperiment
ASIC	– **A**pplication-**S**pecific **I**ntegrated **C**ircuit
CASINO	– Monte **CA**rlo **SI**mulation of electro**N** trajectory in s**O**lid
CPM	– **C**ounts **P**er **M**inute
DSP	– **D**igital **S**ignal **P**rocessor
FoV	– **F**ield **o**f **V**iew
FPGA	– **F**ield **P**rogrammable **G**ate **A**rray
HLD	– **H**igh **L**evel **D**iscriminator
HPD	– **H**ybrid **P**hoton **D**etector
HV	– **H**igh **V**oltage
ISPA	– **I**maging **S**ilicon **P**ixel **A**rray
LHCb	– **L**arge **H**adron **C**ollider **b**eauty
LLD	– **L**ow **L**evel **D**iscriminator
LVDS	– **L**ow **V**oltage **D**ifferential **S**ignalling
MIPS	– **M**illion **I**nstruction **P**er **S**econd
NIM	– **N**uclear **I**nstrumentation **M**odules
PAW	– **P**hysics **A**nalysis **W**orkstation
PBB	– **P**iggy **B**ack **B**oard
PCB	– **P**rinted **C**ircuit **B**oard
PET	– **P**ositron **E**mission **T**omography
PGA	– **P**in **G**rid **A**rray
PI	– **P**lanar **I**maging
POCI	– **P**er-**O**perative **C**ompact **I**mager
PSD	– **P**osition **S**ensitive **D**iode
PSF	– **P**oint **S**pread **F**unction
RICH	– **R**ing **I**mage **CH**erenkov
RMS	– **R**oot-**M**ean-**S**quare
SMD	– **S**urface **M**ounted **D**evice
SPECT	– **S**ingle **P**hoton **E**mission **C**omputed **T**omography
VHDL	– **V**ery high speed integrated circuit **H**ardware **D**escription **L**anguage
YAP:Ce	– **Y**ttrium-**A**luminium **P**erovskite doped with **C**erium

Chapter 1
Introduction

1.1 Overview

The Large Hadron Collider (LHC) is currently being built at CERN[1], the world's largest particle physics laboratory situated near Geneva, Switzerland. This huge particle accelerator will bring protons into head-on collision at higher energies (14 TeV) than ever achieved before, allowing scientists to have a much greater understanding of the Universe. Placed at strategic interaction points, particle detectors play an important role making possible the quantification of such collision interactions. CERN experiments seek for answers and along the way questioning our existence, answers at CERN have changed our daily lives, giving us new technologies in different domains such as electronics, mechanics, software, accelerators, vacuum, etc. A continuous improvement of these technologies is required in the field of tracking devices for elementary particle physics. New detectors require faster electronics, very good spatial resolution and minimal noise.

It is in this context and with the aim of taking advantage of the existing technology at CERN for high particle physics that the topic of this study emerges. In this collaborative research activity, we intend to do a technology transfer of the gamma detection devices for medical applications and we propose in this work a gamma camera prototype that belongs to the family of hybrid photon detector (HPD) tubes. The originality of this camera concept is the implementation of a silicon detector array, the Omega3/LHC1 chip [Heijne et al., 1996], as the tube anode. Previous work with the first laboratory prototype led us to believe that the tube would have excellent performance for high resolution imaging in the field of nuclear medicine, with spatial resolution values below 1 millimeter. In fact, ionising radiation is widely used in medical diagnostic techniques and this camera could be approved as a general-purpose small field-of-view gamma camera suitable for a variety of non-invasive applications. This represents a real opportunity to innovate the technology in this field since the present state-of-the-art in

[1] CERN, European Organization for Nuclear Research; http://www.cern.ch, 2007.

nuclear medicine imaging (excluding Positron Emission Tomography) suffers from poor spatial resolution (a few millimeters) and still consists of upgrades of the standard gamma camera introduced by Anger in 1958 [Anger, 1958]. Their performances do not fulfil the requirements for detection of early stage tumours and only after practically forty years, progress in detector technology has led to the development of a new generation of pixel imaging devices but still few are commercially available in the market nowadays. Despite their small effective area, pixel detectors are becoming a standard in new detector designs. An important feature of the proposed camera is in fact its small size and the significant achievement of this collaborative work is the development of a compact portable readout system which increases the ease with which it can be manoeuvred, thus improving its utility.

1.2 Objectives and contributions

The aim of this thesis is to project, develop, construct and make operative a new prototype gamma imaging system based on improvements and upgrades of an existing one at CERN. In support of this we have set the following objectives:

1. Characterize the performance parameters of the existing system for gamma imaging with the HPD encapsulated with the Omega3/LHC1 chip.
2. Study the collimator and crystal scintillator efficiencies of the HPD with Monte Carlo techniques.
3. Study the electrostatic field of the HPD and the charge collection in the Omega3/LHC1 pixel detector with an electric field simulation program.
4. Improve the reconstruction algorithm and develop a new graphical interface in Visual Basic for Windows.
5. Integrate and program new electronics cards to substitute the present VME-NIM based readout system.
6. Develop a graphical interface, based on visual basic for windows, to control the readout system.
7. Implement an automated X-Y positioning table for measurements and wide area imaging purposes.
8. Demonstrate the utility of the system for high-resolution gamma imaging.

In addition, one of the requirements of this system is to be able to adapt, in the near future, to a recent HPD prototype tube manufactured at Photonis-DEP, Netherlands [Photonis-DEP, 2006]. This HPD is encapsulated with the new LHCb pixel readout chip [Aglieri Rinella et al., 2006] and was developed for the Ring Imaging Cherenkov counters of the LHCb experiment at CERN.

My thesis contributions range from issues such as electronic characterising data, numerical simulation and readout acquisition/analysis software programming, to fundamental studies and measurements with the pixel hybrid photon detector. It includes objectives stated above with items numbers 1, 3, 4, 7 and 8, and with a small contribution in Monte Carlo simulations (item 2). The most important challenge of the thesis proposal in this collaborative research activity, was the integration of new readout electronics cards, and particularly its programming (objectives items 5 and 6). I was involved at this stage and was given the task of testing circuits and analysing embedded systems programmed in Visual Basic to address their problems.

1.3 Outline of this thesis

This work describes the development of a high-resolution gamma imager dedicated to small field-of-view (FoV) studies. It has been essentially structured around technical details about each component present in the system, in order to provide the reader with comprehensive information on photon detection physics.

Chapter 2 is an introduction to nuclear medicine imaging and provides a short description of the ISPA-tube and other comparable semiconductor detectors with imaging techniques based on single photon counting. In Chapter 3 the structural aspects of the ISPA-tube are fully described together with the physical processes that contribute to the image reconstruction. Chapter 4 details the readout electronics system especially designed for this application. This chapter is followed by the description of the developed software enabling easy system-integration. An approach to the mathematical method of image reconstruction is also included in Chapter 5. Chapter 6 presents the laboratory measurements carried out and reports on the performance characterization of the ISPA-tube. The potential evaluation of this gamma camera is explored in a clinical comparison study with a SPECT camera. Finally, the conclusions of the measurements on the gamma camera prototype are presented in Chapter 8. This includes possible improvements for continued research.

References

[Aglieri Rinella et al., 2006] G. Aglieri Rinella et al., **Performance Studies of Pixel Hybrid Photon Detectors for the LHCb RICH Counters**, Nucl. Phys. B (Proc. Suppl.) 150, p. 285-289, 2006.

[Anger, 1958] H. O. Anger, **Scintillation camera**, Rev. Sci. Instr., vol. 29, p. 27, 1958.

[Heijne et al., 1996] E. Heijne et al., **LHC1 A semiconductor pixel detector readout chip with internal tunable delay providing a binary pattern of selected events**, Nucl. Instr. Meth. in Phys. Res. A 383, p. 55-63, 1996.

[Photonis-DEP, 2006] Photonis-DEP, **New developments at PHOTONIS**, conference PAVI 06, Milos, Greece, May 2006.

Chapter 2

Nuclear Medicine Imaging

Since the production of radioisotopes, scintigraphic detection of metabolic functions or diseases has led to the study of the physiology of organs and tissues, and a new scientific field was born: Nuclear Medicine. It deals with the use, application and imaging of radioactive materials primarily focused on the functional imaging of organs and not on the anatomic imaging because the spatial resolution of radionuclide examinations is still limited, part of it by the gamma detection system. Much of the clinical nuclear medicine imaging is simple Planar Imaging (PI) but the availability of new radionuclides and the progress in detector technology has led to the development of other techniques such as Single Photon Emission Tomography (SPECT) and Positron Emission Tomography (PET). The main differences in the three methods arise from detector geometry and image processing: simpler in PI and more elaborate in SPECT and PET, where Fourier analysis and backprojection algorithms are necessary. However, the methodology remains the same: single photon counting. This chapter focuses only on planar imaging since it is directly related with the application proposed in this work. The following topics are briefly introduced just to provide a minimal background information to the reader. They cover the basic aspects of nuclear medicine, including the use of radioisotopes, their diagnostic applications and finally their radiation detection with a description of the ISPA-tube and recent examples of comparable imaging cameras available in the market.

2.1 Use of radioisotopes

Radioisotopes or radioactive isotopes are unstable isotopes of an element that decays or disintegrates spontaneously, emitting several types of radiation. They are used in diagnostic as radioactive tracers which emit gamma rays from within the body, i.e. the presence and movement of the radioisotope in the body can be detected by monitoring the emission of the gamma rays. Administered by injection or inhalation, the isotope is linked to a chemical compound (radiopharmaceutical) which is absorbed by specific

organs. The radiopharmaceutical is then chosen in such a way that this compound is preferably absorbed by the organ in which we are interested. Thus, the region under study becomes an active source of radiation. With a specific detector, an image can be produced by capturing an intensity map of the gamma radiation emission.

The image sharpness, contrast and signal-to-noise ratio will depend on the metabolic properties of the object under study, but most of all, will depend on the energy and radiation dose of the selected radioisotope. Sharpness is related to the resolution of the image and can be defined as a degree of clarity in terms of focus and contrast. It is considered desirable for an image to have good sharpness.

For imaging, the radioisotope must emit gamma rays of sufficient energy to escape from the body since it is partly absorbed within the patient. Another consideration related to the sensitivity variation of the detector in function of the incident energy must also be made, taking into account that photons that are not absorbed by tissues must definitively be by the detector. So if the energy is raised too high, the sensitivity of a detector will diminish. On the contrary, a decrease in the energy will increase the angle of scattered photons and consequently degrade the contrast of the image.

All these contradictory requirements must be taken into account to reach a suitable energy. “Suitable” because the desired quality of an image is dependent on its intended task, in the context that it must gives to the clinician the necessary information to help her/him perform a correct diagnosis.

Furthermore, the intensity of the radiation is responsible for the signal-to-noise ratio and the minimisation of the radiation dose to the patient must then be considered. For this reason, radiotracers are generally short half-lived (which is the time in which the activity is reduced by 50%) isotopes and the amount given to a patient is just sufficient to obtain the required imaging before its decay. The patient is irradiated from the time the dose of radioactive material is administered until it is eliminated from the body, leaving no trace that the exam was ever done. The radiation exposure is quite small and is less intense than conventional radiological examinations. It does not raise any type of reaction in the patient, neither does it disturb the process measured, but in all cases, the dose is calculated. For research in non-human studies, the limit quantity of radiopharmaceuticals used can be omitted, but normally the source is kept at low intensity due to the necessary collimation (see Section 3.1 – Collimator) and due to the type of detector used with respect to efficient detection.

As mentioned above, the choice of the radioisotope depends on the type of examination one wants to perform. Hundreds of radioisotopes are available in Nuclear Medicine and they require a generator, a reactor or a cyclotron for production. Table 2-1 presents a list of the commonly used radioisotopes in Nuclear Medicine.

Radionuclide	Gamma-ray energy (keV)	Half-life	Production	Diagnostic Imaging
Technetium-99m	141 (89%)	6.01 h	Generator	Skeleton, myocardium, salivary, thyroid, lungs, gastric, liver, brain, spleen, bone marrow, kidney, gall bladder
Xenon-133	81 (38%)	5.24 d	Reactor	Lungs
Gallium-67	93 (39%) 185 (21%) 300 (17%) 394 (5%)	78.26 h	Cyclotron	Inflammation
Thallium-201	135 (2.6%) 167 (10%)	72.91 h	Cyclotron	Myocardium
Iodine-131	80 (3%) 284 (6%) 364 (81%)	8.04 d	Reactor	Thyroid, liver, kidney
Iodine-123	159 (83%)	13.27 h	Cyclotron	Thyroid
Krypton-81m	190 (67%)	13 s	Cyclotron	Lungs
Indium-111	171 (90%) 245 (94%)	2.81 d	Cyclotron	Brain, colon

Table 2-1: Common radioisotopes used in Nuclear Medicine imaging.

Iodine-131 was the earliest and was used to diagnose thyroid diseases. Nowadays, the radioisotope most widely used is technetium-99m, employed in some 80% of all nuclear medicine procedures. The main reason is mostly due to the fact that it can be made easily without requiring a reactor or a cyclotron. Instead a so-called “generator” is used, a lead pot enclosing a glass tube containing the radioactive material needed for imaging. Technetium-99m has a half-life of six hours which is long enough to examine metabolic processes yet short enough to minimise the radiation dose to the patient. Technetium-99m is a very good candidate to study the application of the proposed work since its gamma ray emission energy is 140 keV, energy value that can easily escape the human body and can be accurately detected by our gamma camera.

The quality of the radiopharmaceuticals as a *messenger* that brings information of the organ functioning from the inside to the outside of the body provides us with a powerful non-invasive diagnostic tool.

2.2 Nuclear imaging techniques

With the use of radionuclides, a large number of diagnostic procedures can be done just by selecting the appropriate radiopharmaceutical that will be absorbed by a specific organ. It can be used to visualize blood flow obstruction, to study pulmonary ventilation, to assess bone growth and to diagnose abnormal organ function. By identifying abnormal tissue in terms of its cellular activity, smaller tumours can be detected before morphological changes show up in conventional techniques such as x-rays or magnetic resonance imaging. Abnormal tissues, especially cancer cells, have a different cellular activity than normal one, and therefore uptake different amounts of the radioactive substance, with a consequent smaller or larger gamma emission. The existence of so-called *hot* spots of high metabolic activity or *cold* spots of low metabolic activity can thus indicate the presence of abnormal or cancerous cells in normal tissue. Also, the time evolution of the uptake in tissue can give valuable information about the specific contribution of the traced substance to cellular activity. By making sequential images of the distribution over a period of time, an unusual pattern or rate of isotope movement could indicate malfunction in the organ. The use of functional imaging methods can therefore allow an earlier detection of otherwise unobserved small tumours, with a consequent improvement of cure probability, all adding to a better life quality for the patient.

Radiopharmaceuticals can be also used as an intraoperative diagnostic tool to assist in surgery, identifying the metastatic cells and helping surgeons to achieve better precision in tumour mass excision. It might be usable in the same manner as a counting probe, although that a counting probe is not capable of providing a visual indicator of the location of a tumour.

A third and major imaging technique in radiopharmacy is the development of the radiopharmaceutical itself. The development of novel tracers is a vital step in the study of diseases and can be achieved through molecular imaging of small laboratory animals, such as mice and rats. Also, mouse models of human diseases are providing important clues to the causes, diagnosis and treatment of these. Along with imaging instrumentation, typical mice radiopharmaceutical laboratory studies that involves the administration of a radiotracer followed by the animal dissection to examine the internal organs, is less required. It is instead replaced by studying the time-activity behaviour of

a radiotracer *in vivo*, offering a vast improvement in data quality. Examples of some nuclear medicine images are shown in Figure 2-1.

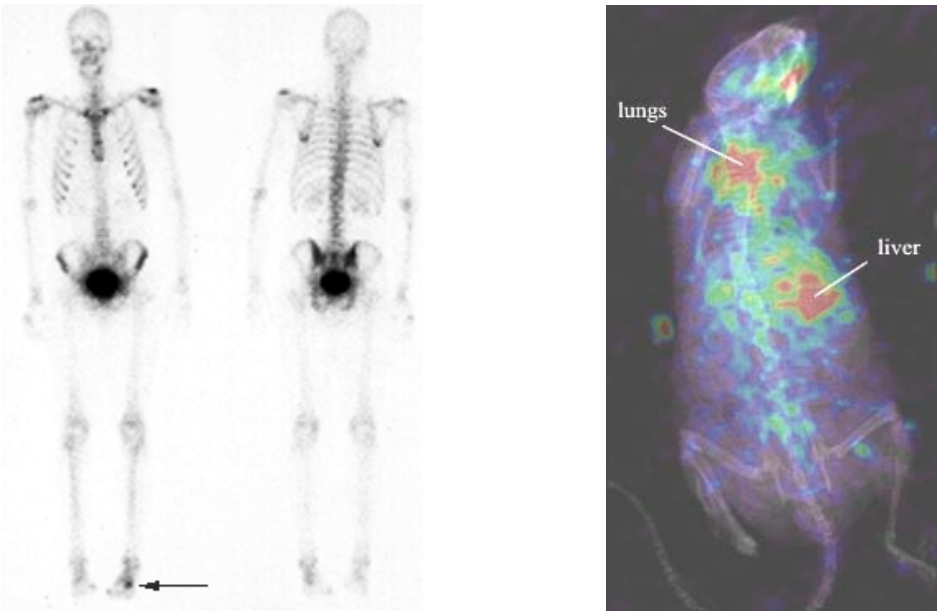

Figure 2-1: Two nuclear medicine images examples. (left) Planar bone scan of a 17 year old basketball player with persistent foot pain. Tc-99m was administrated intravenously. The bone scan shows a hot spot (arrow) in the left foot representing a stress fracture that is too small to be seen on a conventional x-ray exam; (right) Planar gamma imaging/x-ray combination image of a mouse [JLab, 2004]. The radiotracer (Tc-99m) is trapped in cells containing the transferred gene in the lungs and liver.

2.3 Semiconductor cameras

The molecular nature of Nuclear Medicine offers almost unlimited possibilities for new diagnostic discoveries. However, the use of such resource is limited by what we consider the worst disadvantage of Nuclear Medicine imaging compared to other modalities: poor spatial resolution. The poor spatial resolution is a consequence of limitations of the gamma camera and its collimators. Nowadays, Nuclear Medicine cameras equipped with the highest resolution collimators present a spatial resolution of 3-4 mm. This is clearly insufficient for early detection screening of abnormal organ function as discussed previously, or for small animal imaging studies, where the major challenge resides in their small size (for example, a mouse brain is less than 1 cm across). An effort is thus necessary to develop detectors capable of performing functional images of very small structures (below 1 mm resolution). Positron Emission Tomography (PET) scan has been considered as an alternative option to achieve high spatial resolution down to 1 mm. It is a technique that makes use of radiotracers that

emit positrons and its best spatial resolution is not only limited by the intrinsic spatial resolution of the detectors, as it is in PI or SPECT. The physical limitation of PET imaging is the fact that the emitted positron has kinetic energy, varying from a few hundred keV to several MeV depending on which radioisotope, and will thus travel a few millimeters to centimeters before annihilating with an atomic electron. Thus the site of the annihilation is not the site of emission resulting in a limitation to the defining of the origin of the decay. One of the major strengths PET has over SPECT is the ability to measure, directly, the attenuation effect of the object being viewed. And even though PET produces higher resolution images, SPECT still offers three main advantages: the isotopes used in SPECT have a longer decay time (a single radiopharmaceutical production facility can provide materials to a broader area), SPECT centres are more numerous, and the exam costs less.

The present state-of-the-art in nuclear medicine imaging is the Anger Camera [Anger, 1958], a large NaI:Tl single crystal read by an array of photomultiplier tubes. The position of the incoming photon is determined by averaging the light collected by each tube. The major disadvantages of this detector are its large dimensions, heavy weight and its low spatial resolution. In compensation, its large field of view allows viewing an entire region simultaneously. This system was invented more than 40 years ago, and while it has been used successfully ever since as a general purpose gamma camera, new technologies of radiation detection now allow the development of more compact and higher resolution detector systems.

Nuclear imaging is undergoing rapid changes and is increasingly moving from analog to digital technologies, giving place to instrumentation based on semiconductor detectors. In semiconductor detectors the energy loss of traversing charged particles in semiconductor crystal is used to create free charge carriers. The detectors are constructed in a diode structure necessary to remove thermal free charge carriers that would cause a high dark current. These diodes are reversed bias and the resulting electrical field makes the charge carriers drift through the crystal to the electrodes. The induced current is sensed by charge sensitive amplifiers. Depending on the segmentation and the placement and distribution of the necessary electronics the detectors are called pad detectors, microstrip detectors or pixel detectors. An important property of a semiconductor detector is the integration of sensor elements and readout electronics of small sizes. These detectors have an excellent energy resolution which

improves the suppression of Compton scattering that would otherwise contribute noise to the image. Among other benefits digital systems promise better image quality and reduced radiation dose compared to conventional ones. However, due to their small sizes and small field of view they can not be considered as general purpose detectors. For large area imaging, the single detector must be scanned over the area of interest and over periods of time that may vary from milliseconds to hundreds of seconds. This process in which a mosaic image can be formed is governed by the efficiency of the camera and the maximum radioactive dose that can be safely given to the patient. In most cases, scanning may slow down the exam process, taking into account that the image is affected by patient movement, it is not possible to do any dynamic studies where the change in function of an organ is measured with time. But with the recent progress in digital technology using computers, it is becoming possible to correct the position linearity and uniformity of the detection. In fact, due to the high costs associated to the manufacturing technologies of the detector, signal processing comes with mathematical functions to correct and compensate the efficiency loss.

2.3.1 The ISPA-tube

The semiconductor camera presented in this work, is an alternative device for the phosphor-screen image intensifier, which is used to create an image by detecting single photons. In other words, it amplifies visible and near-infrared light from an image by magnifying the intensity produced. It works by having a vacuum tube with a photocathode at one end that converts incoming photons to electrons. From there the electrons are accelerated until they hit a phosphor screen at the other end, converting it back to photons, which can be viewed by a camera or by eye. In medical imaging, the incoming radiation photons must be first converted to visible photons. For these purpose medical image intensifiers present a scintillator input window. This device is widely used in standard radiodiagnostic procedures such as in fluoroscopy where instant image capture is demanded. To achieve the required light amplification, enabling the viewer to easily see the structure of the object being imaged, the patient exposure to an external x-ray source is relatively high. In nuclear medicine this would translate to more radiation dose for the patient. Alternatives to reduce the radiation dose will benefit from recent advances that include the digitization of the images captured and flat-panel detector.

Toward this concept and still based on standard image intensifier technology emerges the ISPA-tube.

The ISPA-tube technology belongs to the Hybrid Photon Detector class (HPD) and differs from conventional image intensifier by presenting a PIN diode integrated in the vacuum tube instead of the phosphor screen. The first prototype was delivered to CERN in January 1998 by a collaboration carried out with the company Delft Electronic Products (DEP) regarding the tube encapsulation, called nowadays Photonis-DEP[1]. The development of such prototype was first devoted to the CERN LHCb (Large Hadron Collider beauty) experiment to observe Cherenkov ring images (RICH). While not optimized for this application it has permitted testing many of the required features.

Depending on the electrostatic field configurations, the ISPA tube is designed in two type models: proximity- and cross-focused tube. The proximity-focused tube presents a flat surface window with parallel field lines giving an entrance window/anode surface ratio of 1:1. The cross-focused tube presents a spherical surface window with field lines crossing before the anode providing an inverted and demagnified image. The entrance window/anode surface ratio is then above 1. This configuration presents a higher FoV but a loss in extrinsic spatial resolution. Figure 2-2 displays photographs of the two ISPA-tube designs.

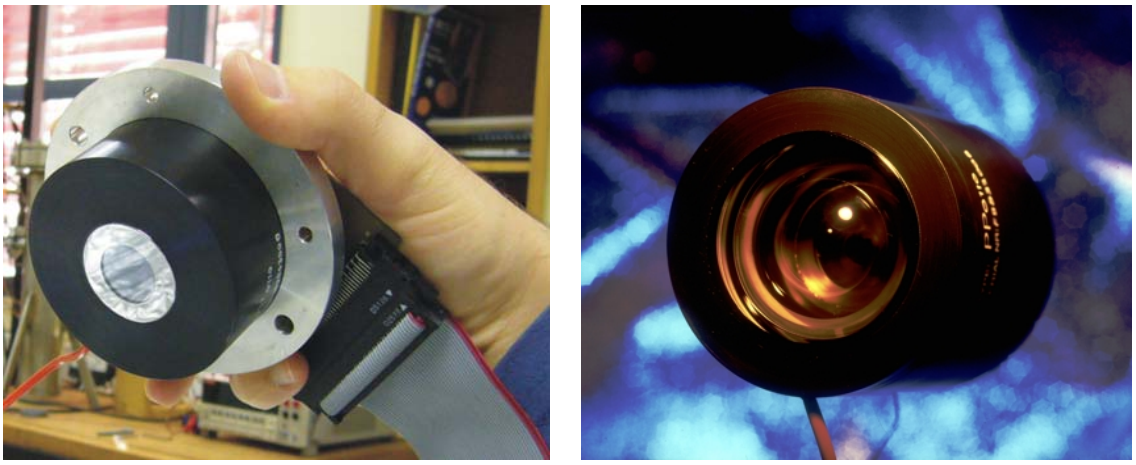

Figure 2-2: (left) Photograph of the ISPA proximity-focused tube that creates 1:1 images; (right) Photograph of the ISPA cross-focused tube that creates 4:1 images. In both designs, the tube is connected to a small printed circuit board with a flat cable connection to the readout electronics. For a correct/safe utilization procedure, the tube is mounted inside a protective envelope to avoid light entrance and electrical discharge.

[1] Photonis-DEP B.V; http://www.photonis-dep.com, 2006

The initial development of the ISPA cross-focused tube for gamma ray imaging is reported in [M. Alemi et al., 2000, C. D'Ambrosio, 2000]. Seeking for high resolution only the ISPA proximity tube is considered in this thesis, however the medical application proposal of this detector applies for both designs since the basic operation principle is the same and is described as follows:

When a photon coming from the organ under study crosses the collimator parallel to its preferential axis and strikes the crystal scintillator, a spotlight is created. A photocathode deposited on the inner side of the scintillator collects the light and generates photoelectrons, which are electrostatically accelerated up to 25 keV onto silicon pixels at the ISPA-anode, giving a spot whose centroid is used to determine with unprecedented precision the incoming photon entrance position, and whose number is proportional to the incident photon's energy (Figure 2.3).

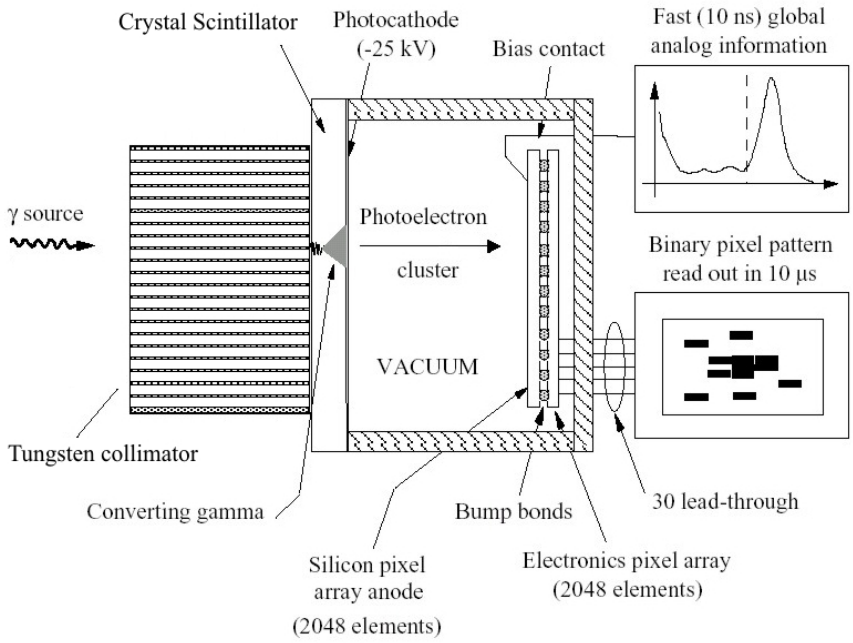

Figure 2-3: Operating principle of the ISPA proximity tube. The photons generated in the scintillating detector are converted at the photocathode into photoelectrons and accelerated onto the silicon anode. The global analogue signal taken from the detector plane provides information on the total charge created in the detector. This signal is used to operate the tube in the self-triggering mode. The binary read-out of the pixel electronics provides position information and allows 2-D imaging.

The pixel detector contains 2048 rectangular pixels with $50 \times 500\ \mu m^2$ sides, offering a field-of-view (FoV) directly related to the size of the chip ($8 \times 6.4\ mm^2$). Each pixel is bump-bonded to its individual and equally sized front-end electronic pixel. Its total read-out time amounts to less than 10 μs, far surpassing the several milliseconds of a CCD. The small pixel areas and the direct bonding between detector and electronics

reduce considerably the input capacitance viewed by the preamplifier, resulting in low noise levels that are essential for good contrast in optoelectronic images. The contact layer of the pixel chip serves as an electrode for the chip bias voltage. Each time one or more photoelectrons hit the anode chip, they generate a fast (~10 ns) electronic pulse. These analogue signals allow self-triggering the ISPA tube and enable the suppression of unwanted background events by setting appropriate energy windows.

2.3.2 Worldwide cameras

To provide accurate and clear images of very specific medical and research activities targeted by radiopharmaceuticals, many research groups worldwide are designing more sensitive detectors and dedicated scanning equipment. This motivation is aimed toward the need for a flexible detector than can be more easily positioned anywhere closer to the patient body improving spatial resolution. Some of the best known prototypes under development in laboratories and some already available commercially are presented below. They are at present single-photon counting systems comparable to the ISPA-tube and its position measurement application.

The Medipix2 European Collaboration[2] at CERN has developed a prototype single photon counting chip to improve x-ray, gamma and beta imaging, the medipix2 chip. It converts directly the x-rays into detectable electric signals. The chip is a CMOS ASIC (Application-Specific Integrated Circuit) and has an active area of 14×14 mm^2, composed of an array of 256×256 pixels with pitch of 55 μm. Experimental tests have shown promising results in the field of digital autoradiography [P. Russo et al., 2004]. This imaging technology is essentially ready for industry technological transfer and for use in biological and medical laboratories for beta digital autoradiography. Recent applications are reported in [P. Russo et al., 2003, C. Ponchut et al., 2003, S. R. Amendolia et al., 2004]. At present the Medipix collaboration is designing and building a compact gamma camera with a 1 mm thick CdTe pixel detector, for Tc-99m 140-keV imaging of sentinel lymph nodes during radio-guided surgery, shown in Figure 2-4. This system has potential for high resolution imaging down to the pixel size (55 μm) [M. Chmeissani et al., 2004]. A final conclusion about its relative performance in a clinical environment must wait for more comprehensive studies.

[2] Medipix2 Collaboration; http://www.cern.ch/MEDIPIX

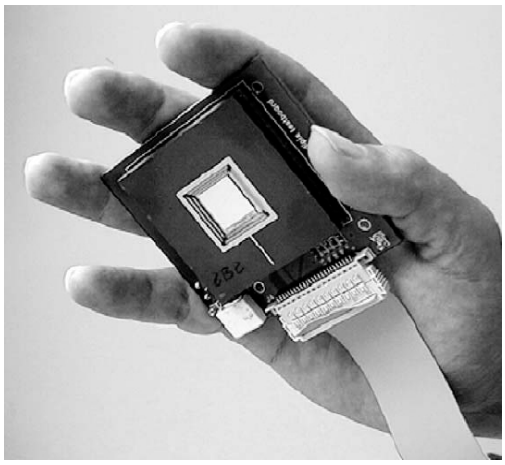

Figure 2-4: Medipix2 hand-held probe head (with the collimator removed) connected to a small footprint printed circuit board, with flat cable connection to the readout electronics. The chip is bonded to a CdTe pixel detector. Extracted from [P. Russo et al., 2003].

Another investigation group at *Insitut de Physique Nucléaire d'Orsay*[3] has developed a per-operative compact imager (POCI), shown in Figure 2-5. The current prototype with a 24 mm diameter usable field of view was first designed to validate the concept of per-operative imaging during cancer surgery [Menard et al., 1998]. It consists of a head module composed of a high resolution tungsten collimator and a YAP:Ce crystal plate, optically coupled to a silicon position sensitive diode (PSD). A new prototype which scales the field of view up to a 60 mm diameter sensitive area is currently under development to investigate the potentiality of miniature gamma camera with high spatial resolution to map the biodistribution of specific radiopharmaceuticals on small animals. An intrinsic spatial resolution of ~1 mm FWHM at 120 keV was achieved [S. Pitre et al., 2003].

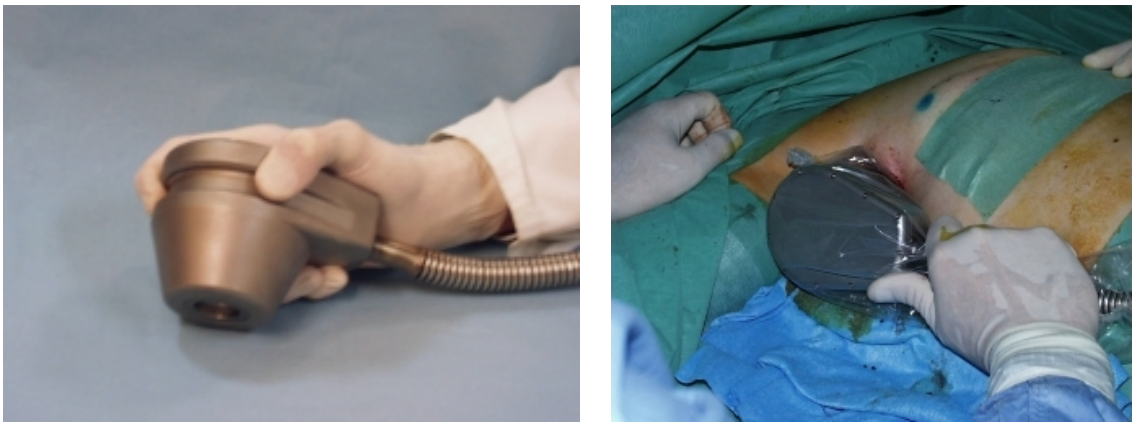

Figure 2-5: (left) Photograph of the per-operative compact imager (POCI); (right) Application test of the camera in a radio-guided operative cancer surgery.

[3] IPN d'Orsay, Groupe Modélisation Physique Interfaces Biologie; http://ipnweb.in2p3.fr/, 2006

Anzai Medical[4] contracted eV PRODUCTS[5] to design, develop and manufacture a handheld, light-weight, CZT-based gamma camera, the eZ-SCOPE AN [A. Abe et al., 2003], shown in Figure 2-6. This gamma camera is designed to produce both planar and tomographic images. 256 channels of CdZnTe (2 × 2 mm^2 pitch) are arranged on a detector tile. The eZ-SCOPE AN is significantly different from gamma cameras based on NaI/PMT technology and can reach a resolution of 2.2 mm ideal for gamma imaging of small animals.

Figure 2-6: (left) Photograph of the eZ-SCOPE AN portable gamma camera; (right) Imaging application of gene expression in a representative mouse.

It presents a weight of 820g (excluding the collimator) and has dimensions of 73(W) x 77(H) × 212(L) mm^3. The effective field of view is 32 × 32 mm^2. Figure 2-7 shows a comparison of a phantom image taken with this camera and an Anger camera.

(a) (b) (c)

Figure 2-7: Image comparison between (b) the eZ Scope (CdZnTe) camera and (c) a standard Anger camera (NaI). Data are produced by using (a) a 1.7 mm hollow phantom with a radioactivity concentration of 0.74 MBq/cc of Tc-99m. Collection times are 5 s for (b) and 10 min for (c).

[4] Anzai Medical Co.,Ltd; http://www.anzai-med.co.jp/
[5] eV Products; http://www.evproducts.com/

Another company that provides a higher field of view camera is TeraRecon[6]. It highlights with a handheld mini gamma camera developed for localizing sentinel lymph nodes, the MGC500, shown in Figure 2.8a. Primary applications include intra-operative and pre-surgical lymphoscintigraphy. The MGC500 is based on a CdTe semiconductor that directly converts gamma ray energy into electrical signals achieving millimeter spatial resolution images with 1024 pixels (32 × 32 matrix size) and a pitch of 1.4 mm. A high degree of precision is achieved utilizing tungsten collimation. Its effective field of view is 44.6 × 44.6 mm^2 and its energy range is 60-300 keV with an energy resolution of 7% at 60 keV. It presents a weight of 1.4 kg and has dimensions of 86(W) x 86(H) × 206(L) mm^3.

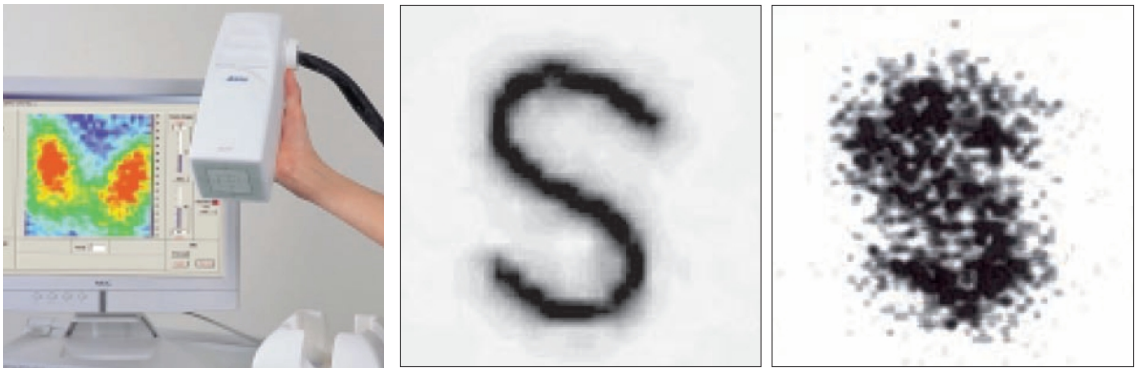

(a) (b)

Figure 2-8: (a) Photograph of the MGC500 mini gamma camera; (b) Image comparison of a 1 mm hollow S-shape phantom between the MGC500 (left) and a conventional gamma camera (right). Data are produced with a radioactivity concentration of 30 MBq of Tc-99m. Collection time is 2 s in each case.

Finally, less mobile but more versatile is the 2020tc imager introduced by Digirad Corporation[7] [H. Narita et al., 2001], shown in Figure 2-9a. It was the world's first solid state nuclear medicine gamma camera (1999). Its large field of view (216 × 216 mm^2) composed of an 8 × 8 array of 2.5 × 2.5 × 0.5 cm^3 detector modules, allows viewing an entire region simultaneously. Each detector module is composed of CsI(Tl) as the scintillation material and a Si photodiode. With an energy range of 60-300 keV, the best extrinsic spatial resolution achieved with a low energy high resolution collimator is 7.7 mm. Figure 2-9b shows a comparison of breast images taken with this camera and an Anger camera.

[6] TeraRecon, Inc; http://www.terarecon.com
[7] Digirad Corporation; http://www.digirad.com, 2006

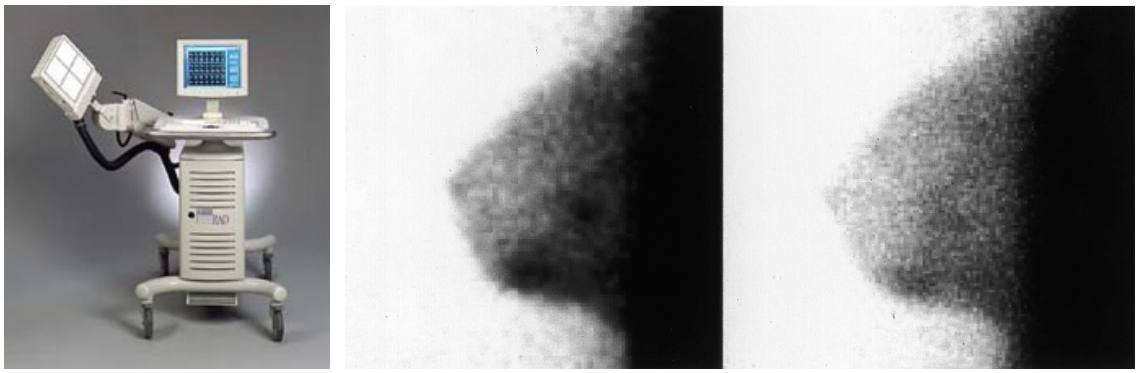

(a) (b)

Figure 2-9: (a) Photograph of the Digirad 2020tc Imager; (b) Comparison of images taken with the Digirad 2020tcTM (left) and a conventional gamma camera (right) with comparable collimators and imaging times.

Although other research groups have not described the commercial prospects for their semiconductor camera, they still come with promising high-performance solid state gamma radiation detectors, which are the object of several projects on behalf of manufacturers such as SIEMENS, Saint-GOBAIN, General Electric, IMARAD, etc. The range of tasks for which those gamma-ray imaging systems are currently being considered are particularly varied. In general, the factors which influence the choice of imaging technique include the field-of view required, the size and structure of the source, the source activity both in absolute terms and relative to the background activity, and the time available to make an image. Thus, one task may be preferred for technical reasons such as spatial resolution constraints. In Table 2-2 some known characteristics of the different gamma cameras presented above are listed in comparison with the ISPA-tube.

Gamma Camera	**Collimator**		**Scintillator material**	**Semiconductor**			**Performances**	
	Type	Hole diameter [μm]		Material	Active area [mm^2]	Pitch [μm^2]	Energy Resolution	Extrinsic Resolution [mm]
ISPA-tube	Tungsten parallel rippled foils	600 × 300	YAP:Ce	Si	8.0 × 6.4	50 × 500	22.6% @ 60 keV	0.7
Medipix 1	Tungsten pinhole	350	-	Si	11 × 11	170 × 170	not available	0.8
POCI	Tungsten parallel hexagonal hole	1000	YAP:Ce	Si	25 × 25	Positive Sensitive Diode	38% @ 120 keV	3.2
eZ-SCOPE	Lead parallel round hole	1000	CZT	CdZnTe	32 × 32	2000 × 2000	8.6% @ 141 keV	2.2
MGC500	Tungsten parallel round hole	not available	CZT	CdTe	44.6 × 44.6	1400 × 1400	7% @ 60 keV	1.4
2020tc	Lead parallel hexagonal hole	not available	CsI:Tl	Si	216 × 216	2500 × 2500	12.8% @ 141 keV	7.7

Table 2-2: Summary of the characteristics of different semiconductor gamma cameras.

2.4 Applications for the ISPA-tube

Preliminary results with this system show that internal organ images with resolution about 10 times better than a standard Anger gamma camera can be obtained. Also, despite its small field of view that will limit its use for some applications, the ISPA-tube could be applied potentially anywhere a full sized gamma camera might be used. Moreover, this camera can be located directly in contact with the region of interest, increasing the solid angle detection and reducing diffusion and attenuation effects of interposed tissues. The following sections briefly describe some types of general radiotracer imaging applications to which the ISPA-tube might be applied successfully.

2.4.1 Radiotracers studies in small animals

Animals play an increasingly important role as models for the study of diseases in vivo and drug development. Mice in particularly, enhanced by the recent completion of both the mouse and human genome maps, and since they share about 95 percent of their genes with humans. Small FoV gamma cameras make clearer, more detailed images and are also useful in monitoring the disease progression or the treatment efficacy. The selection of an isotope is done by imaging and examining many aspects in its behaviour processes. Two examples of such processes are imaging flow based both on the isotope half-life and on the understanding of the time course of the agent's pharmacokinetics, and imaging gene activity in which carefully designed radiolabeled molecular probes can target reporter genes in specific cells. Small animal SPECT imaging offers also the possibility to perform simultaneous detection of multiple processes by using multiple isotopes with different energy.

2.4.2 Intraoperative radioguided surgery

An application of radiotracers in surgery is location of metastases during tumor and lymph node resection. In fact, the surgeon can use a gamma counting probe to assist in intra-operative localization of the metastases and aid conservative excision. An example of the use of this technique is now standard practice in the management of many breast cancer and melanoma patients, namely, in Sentinel lymph node (SLN) biopsy. Surgeons used to perform full axillary or regional dissections on patients, although the benefits were not clear for many patients. Sentinel lymph node biopsies spare many patients the

morbidity and discomfort associated with a full axillary or regional dissection. By adding an intraoperative gamma counting probe it improves some protocols for a SLN biopsy. However, the imaging capability of cameras such as the ISPA-tube provides a visual indicator that a counting probe is not capable. A recent study [C. Greene, 2006], conducted to obtain preliminary experience and information on a small field of view gamma camera used for intraoperative imaging in sentinel lymph node surgeries, revealed that surgeons take advantage of intraoperative gamma imaging over intraoperative gamma counting. It revealed also that camera sensitivity is much more important than camera resolution for the task of intraoperative localization of SLNs in a melanoma or breast cancer patient. Some SLNs have very little uptake, yet intraoperative imaging protocols must be such that low uptake nodes can be detected and localized.

2.4.3 Thyroid imaging

Imaging with technetium 99m pertechnetate and iodine 123 is a common diagnostic method for thyroid disorders. When the deposition of radionuclide is significantly greater in the thyroid gland than it is in the salivary glands, the thyroid tissue is considered hyperactive. For the majority of thyroid imaging procedures, full-size gamma cameras with pin-hole collimators are used by acquiring lateral and ventral images of the neck. Getting the full-size camera close to the thyroid is difficult. Full-size cameras suffer from positioning problems degrading the spatial resolution as the distance patient-detector increases. With its small size and excellent resolution, the ISPA-tube could be used to assist a full-size gamma camera providing diagnostic quality images. The large camera would be used initially to scan the overall thyroid, and then the ISPA-tube would acquire spot views of specific regions.

2.4.4 Scintimammography

Nuclear medicine breast imaging, also called scintimammography, plays a role in both the early detection of breast cancer and the differentiation of benign from malignant disease. In scintimammography with technetium 99m, a malignant tumour might be expected to take up 10 times more radiation per cc than the surrounding breast tissue. Classical detectability studies have demonstrated that a signal-to-noise value >5 is required for reliable detection of cancers. It is then expected that a good signal to

noise ratio combined with high spatial resolution are the key parameters to detect early-stage tumours. The signal-to-noise ratio can be improved by compressing the breast during the image acquisition as in mammography. Because the breast tissue is spread over the camera face, the signal-to-noise ratio for lesions is increased and lesions are more easily detected. However a general-purpose gamma camera has limited intrinsic resolution for tumours smaller than 1 cm and suffers from the disadvantage that the arm and the shoulder keep the camera from being positioned optimally near the breast. Besides, the design of standard gamma camera results in limited depiction of lesions in the medial portion of the breast and thus most cancers diagnosed with scintimammography are larger than 1 cm. A high resolution small gamma camera positioned as close as possible to small-body regions appears as a feasible solution to be used as an adjunct providing quality images.

References

[A. Abe et al., 2003] A. Abe et al., **Performance evaluation of a hand-held, semiconductor (CdZnTe)-based gamma camera**, Eur. J. Nucl. Med. Mol. Imaging, 30(6), 805-11, 2003.

[Anger, 1958] H. O. Anger, **Scintillation camera**, Rev. Sci. Instrum., vol. 29, p. 27, 1958.

[C. D'Ambrosio, 2000] C. D'Ambrosio et al., **Recent developments on ISPA-cameras for gamma ray imaging: gamma imaging with an electrostatic crossed focussed ISPA-tube**, Nucl. Instr. Meth. in Phys. Res. A 442, 279-284, 2000.

[C. Greene, 2006] Carmen M. Greene, **Experience Using a Small Field of View Gamma Camera for Intraoperative Sentinel Lymph Node Procedures**, Master Thesis, Georgia Institute of Technology, 2006.

[C. Ponchut et al., 2003] C. Ponchut et al., **Evaluation of medipix-1 in X-ray scattering and X-ray diffraction applications**, Nucl. Instr. Meth. in Phys. Res. A 510, 29-34, 2003.

[H. Narita et al., 2001] H. Narita et al., **Evaluation of efficiency of a multi-crystal scintillation camera Digirad 2020tc Imager using a solid-state detectors**, Kaku Igaku. 38(4), 355-62, 2001.

[JLab, 2004] Jefferson Lab News Release, **http://www.jlab.org/**, 2004.

[L. Menard et al.] L. Menard et al., **POCI: A compact high resolution gamma camera for intra-operative surgical use**, IEEE Transactions on Nuclear Science 45, 1293-1297, 1998.

[M. Alemi et al., 2000] M. Alemi et al., **First operation of a hybrid photon detector prototype with electrostatic cross-focussing and integrated silicon pixel readout**, CERN preprint No. EP/99-110 and Nucl. Instr. Meth. in Phys. Res. A 449, 48-59, 2000.

[M. Chmeissani et al., 2004] M. Chmeissani et al., **First experimental tests with a CdTe photon counting pixel detector hybridized with a Medipix2 readout chip**, IEEE Trans. Nucl. Sci., vol. 51, no. 5, 2379-2385, 2004.

[S. R. Amendolia et al., 2004] S. R. Amendolia et al., **A prototype for a mammographic head and related developments**, Nucl. Instr. Meth. in Phys. Res. A 518, 382-385, 2004.

[P. Russo et al., 2003] P. Russo et al., **Design of a compact gamma camera with semiconductor hybrid pixel detectors: imaging tests with a pinhole collimator**, Nucl. Instr. Meth. in Phys. Res. A 509, 321-327, 2003.

[P. Russo et al., 2004] P. Russo et al., **Tritium digital autoradiography with a Medipix2 hybrid silicon pixel detector**, Nucl. Instr. Meth. in Phys. Res. A 516, 554-563, 2004.

[S. Pitre et al., 2003] S. Pitre et al, **A hand-held imaging probe for radio-guided surgery: physical performance and preliminary clinical experience**, European journal of nuclear medicine and molecular imaging 30, 339-343, 2003.

Chapter 3

Properties of the ISPA-tube

The ISPA-tube is a device that converts photons to electrical signals. It consists of four general stages: the photon collimation, the light conversion into photoelectrons, the photoelectrons transport and the position detection. Each part is executed by several components combinations that lead to specific processes. To analyse these processes and optimise the detector, a lot of important quantities such as collimator-transmission efficiency, crystal and photocathode conversion efficiency, decay time, optical reflectivity, electric field strength distribution, detector response, electrical noise, etc, must be known. Thereafter, properties of each component can be calculated from individual quantities, and properties of the whole detector can be determined using a convolution. In this application, the goal is to reconstruct accurately the position and energy of the incident photon. In fact, the image seen is not a direct intensity mapping of the incoming photons, but instead the distribution of charges produced by single photon. Hence, a detailed understanding of this imaging device requires a careful description of the detection process, by comparing the observed results to models based on physical principles occurring within the ISPA-tube through the four stages described above. This chapter describes the characteristics properties of the main components presented in Figure 2.3.

3.1 Collimator

In nuclear medicine imaging, the first object that an emitted gamma photon encounters after exiting the body is the collimator. It presents hole pattern made from high density material to effectively absorb gamma rays, usually lead or tungsten. Its function is to block gamma rays that are not travelling directly towards the camera face. This purpose is to ensure the projection of the radioactive distribution coming from a volume located in the focal point. In this way the detector is insensitive to the radiation coming from other volumes and each small part of the crystal views only a small area of

the organ to be imaged. In the first stage of a gamma camera, the collimator design must take into account the type, the density, the thickness, the dimensions, the hole pattern and the septa. It will define the spatial resolution and the detection sensitivity pretended, where sensitivity relates to how many photons that reach the collimator will pass through it. On the other hand, the design of a collimator in such application will be imposed by an important limitation on what we can consider the last stage of the gamma camera detection: the high resolution semiconductor detector.

To benefit from the intrinsic spatial resolution of the semiconductor detector, the collimator must be well dimensioned to be compatible with the pixel size. Collimators for SPECT are of several designs: parallel-hole, pinhole, converging or diverging. The holes may present different geometries: hexagonal, square, triangle or circle. And may be disposed in different configurations: parallel or honeycomb grid. The parallel-hole collimator is the most common. The smaller and the longer are the holes through the collimator, the higher is the resolution. To maximize collimator efficiency, the septa walls should be as thin as possible.

3.1.1 Mechanical properties

The ISPA-tube collimator is parallel-hole type and is made of thin tungsten rippled foils mounted inside a brass housing (Figure 3-1) to be located perpendicular to the entrance window of the ISPA-tube. The usable collimation dimensions are 26 mm long and 10×9 mm^2 area. The choice of this non-conventional type of collimator was due to the simple fact that it is easy to mount without requiring any high cost deep x-ray lithography and electroforming method [O. Makarova et al., 2004], while at the same time assuring a high performance collimator for preliminary tests. It is considered a low-energy collimator for imaging radionuclides such as Tc-99m (140 keV) because higher gamma energies could penetrate the septa walls leading to deterioration of spatial resolution. The choice of tungsten as absorbing element is due to the fact that for this energy window, it presents a higher absorption coefficient (36.23 cm^{-1} @ 140 keV) compared to its main opponent, lead (27.25 cm^{-1} @ 140 keV). Tungsten is also a hard metal that can be considered for the fabrication of submillimeter foils, needed to achieve high resolutions. One curiosity on the photographs shown in Figure 3-1 that may catch the reader's attention is the wire connected to the collimator. This connector ensures

that the collimator is at the same applied high voltage than the crystal scintillator, avoiding discharges in the equipotential spaces between them.

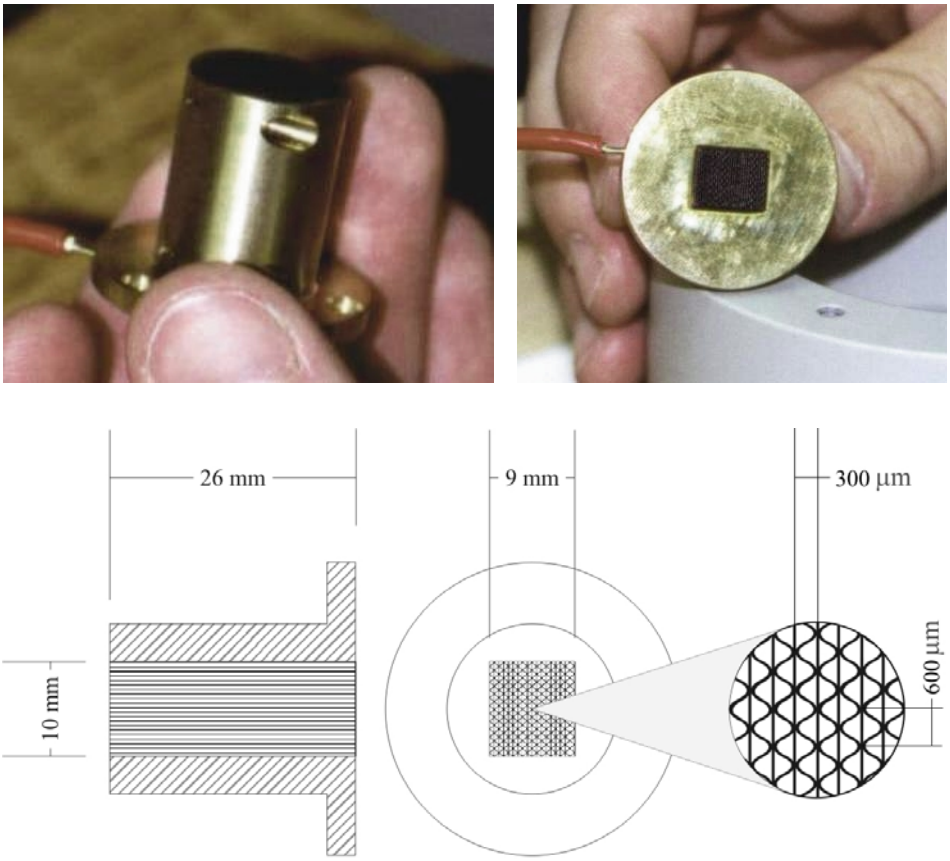

Figure 3-1: Photograph and technical design of the ISPA parallel-hole tungsten collimator. The septa are 60 µm thick.

3.1.2 Geometric properties

The geometrical properties of this non-conventional type of collimator were evaluated by means of a numerical simulation once the analytical calculations for rippled foils configuration turn out to be very difficult.

In a master's degree thesis [C. Ortigão, 2003], a LIP[1] team group has developed a Monte Carlo code from a geometric model of the ISPA-collimator. The numerical code, based on GEANT 3 package tools [S. Gianni et al., 2000], has been first confronted to an analytic approach of a simple multi-parallel-hole collimator. The results revealed a strong correlation between both studies and proved that the Monte Carlo simulation code can be reliable. The geometric properties of the ISPA-collimator achieved by

[1] Laboratório de Instrumentação e Física Experimental de Partículas; http://www.lip.pt, 2006.

means of Monte Carlo simulations are resumed in Table 3-1. This study revealed that an increase in the collimator thickness from 2 cm to 5 cm does not improve significantly the spatial resolution, therefore there is no need to build a collimator with large thickness.

Collimator length [cm]	Sensitivity [normalized for 1 cm]	FWHM [mm]	Energy Resolution [%]
1.0	1	1.050 ± 0.026	16.5 ± 1.4
2.0	0.16	0.676 ± 0.040	16.5 ± 3.4
2.6	0.10	0.585 ± 0.047	16.5 ± 4.4
5.0	0.09	0.495 ± 0.063	16.6 ± 7.1

Table 3-1: Sensitivity, spatial resolution and energy resolution of the ISPA parallel-hole tungsten collimator (rippled foils). Monte Carlo simulation results were obtained using a 122 keV point source photons placed at 1 cm from the collimator. Four collimator thicknesses were used.

In a comparative simulation study between this type of collimator (rippled foils) and a traditional one (parallel and honeycomb grid), we verified that this collimator presents better spatial resolution but worse sensitivity (Figure 3-2). Very thin-holed collimators allow high precision at the level of the incoming photon's position, but reduce dramatically the counting rates. It is clear that this type of collimator is useful to achieve submillimeter spatial resolutions in applications that allow high exposure time such as, for example, molecular imaging of small laboratory animals.

A simple experimental method to asses the sensitivity of the ISPA collimator was made with the collimator placed between a radioactive point-source and a semiconductor detector. The XR-100T-CZT (cadmium zinc telluride) high performance X-Ray detector from Amptek[2] was used. The measurement was done with a cadmium-109 radioactive source, which emits X-rays of 22 keV. By integrating the number of pulses over this 22 keV energy peak region displayed on a multichannel analyser, we can measure the intensity of the incident beam with and without collimator (Figure 3-3), and thus determine the transmission efficiency by taking the ratio between both intensities. With the radioactive point-source placed at a distance of 3 cm from the detector (0.5 cm from the collimator) and a detector active region of 5 mm diameter, an equivalent circular field-of-view of 3.6 degrees was achieved. In this condition the collimator transmits about 1.4 % of the incident flux, which corresponds to a measured sensitivity of 1.4×10^{-2}.

[2] Amptek Inc.; http://www.amptek.com

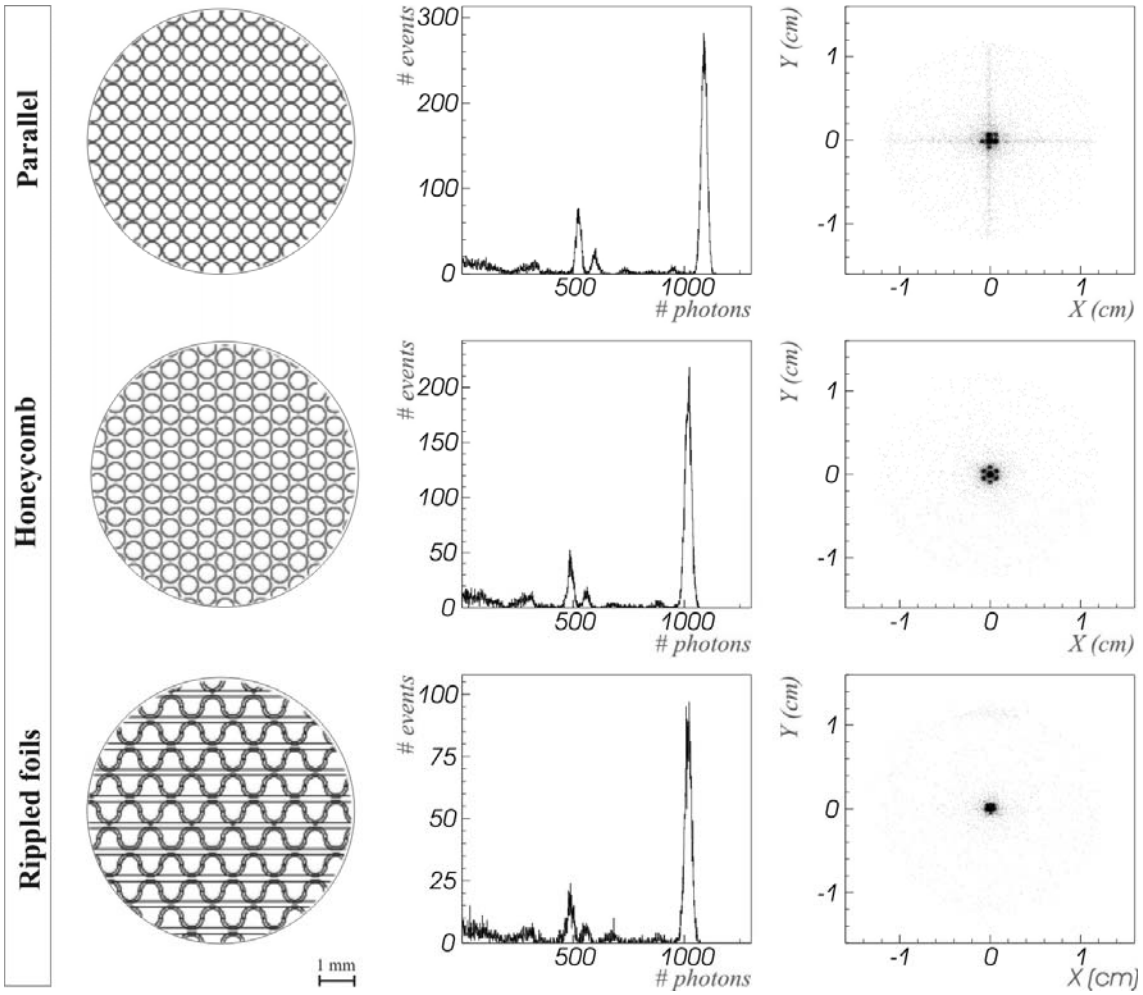

Figure 3-2: Optical photon spectra (middle column) and image reconstruction (right column) of a 122 keV point-source using three different tungsten collimators (left column). The collimator thickness and the source-collimator distance were fixed at 1 cm. The hole diameter is 0.6 mm. The image reconstruction with the parallel hole collimator presents a cross shape due the non-absorption of the radiation through the septa.

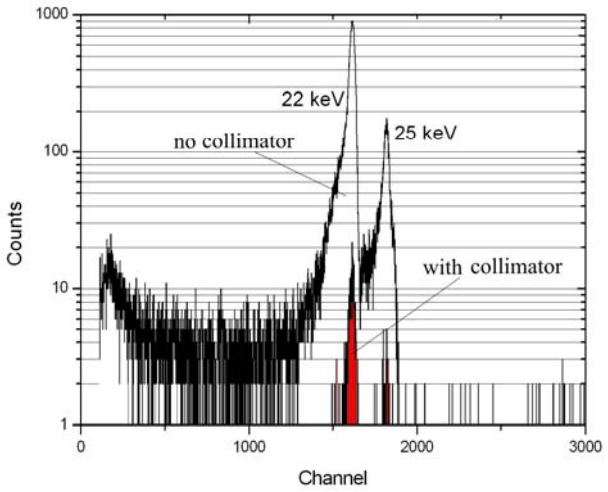

Figure 3-3: X-ray energy spectra of a cadmium-109 point-source captured using XR-100T-CZT detector with and without the ISPA parallel-hole tungsten collimator (rippled foils). Integrals of both peaks have been calculated over the 22 keV energy peak and a ratio of 1:72 has been measured.

3.2 Crystal scintillator

When ionizing radiation interacts with a crystal scintillator, it produces a fluorescent flash with a short decay time ($<10^{-8}$ s) at a characteristic wavelength, known as scintillation. In the case of gamma ray photons, three possible processes can occur at atomic level releasing one or two high-energy electrons: the photoelectric effect, the Compton scattering and the pair production. The probability of occurrence for each of these processes depends on the type of scintillator and the energy of the gamma rays, the latter being predominant for photons of energy above about 10 MeV and therefore not relevant for this application. Figure 3-4 shows the relative importance of the first two interactions when gamma ray energy is absorbed by a YAP:Ce (Yttrium-Aluminium Perovskite doped with cerium) scintillator.

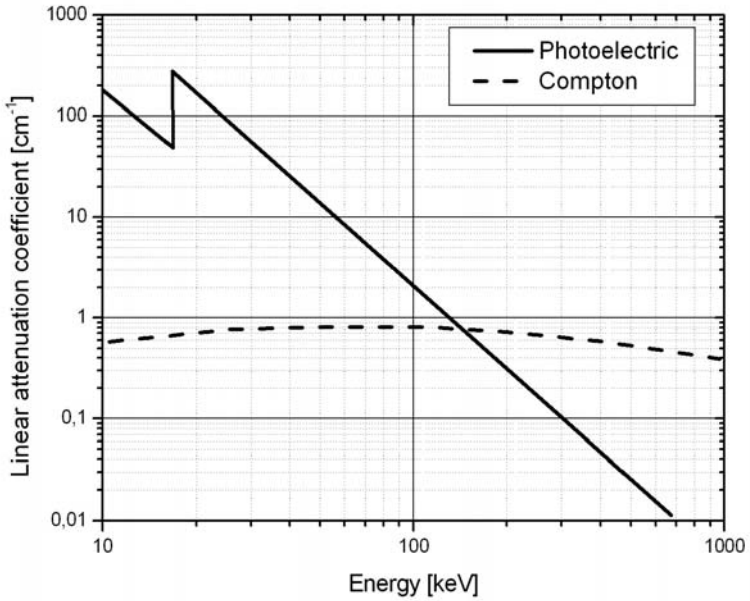

Figure 3-4: Linear attenuation coefficients (cm^{-1}) for standard YAP:Ce scintillator. Extracted from [R. Pani et al., 1995].

Depending on the intended applications, scintillators can be made of a variety of materials and are subsequently divided into inorganic and organic materials. Inorganic scintillators offer advantages of excellent energy conversion efficiency, high absorption efficiency and a good probability for the photoelectric effect compared to organic scintillators. Accordingly, a large number of inorganic materials differ greatly in their physical properties and are suited for energy analysis in nuclear medicine and high energy physics applications. The most common scintillators used in gamma-ray

detectors which are made of inorganic materials are usually an alkali halide salt, such as sodium iodide (NaI) or cesium iodide (CsI). Table 3-2 lists the main characteristics of the most widely used scintillating crystals and their common applications in medical imaging.

Scintillator	Name	Light yield (ph/keV)	Light output (%) of NaI(Tl) bialkali pmt	Emission time (ns)	Wavelength of maximum emission λ_{max} (nm)	Refractive index at λ_{max}	Hardness (Mho)	Density (g/cm^3)	Hydroscopic	Medical application
BaF_2	Barium Fluoride	10	16	630	310	1.50	3	4.88	slightly	PET
BGO ($Bi_4Ge_30_{12}$)	Bismuth Germanate	8-10	20	300	480	2.15	5	7.13	no	PET/CT/X-ray
CaF_2:Eu	Europium-activated Cadmium Fluoride	19	50	940	435	1.47	4	3.18	no	-
$CdWO_4$	Cadmium Tungstate	12-15	30-50	14000	475	2.3	4-4.5	7.9	no	CT
CsF	Cesium Fluoride	2	5-7	300-500	390	1.48	2	4.64	yes	PET
CsI:Na	Sodium-activated Cesium Iodide	41	85	630	420	1.84	2	4.51	yes	SPECT/CT/ PET/X-ray
CsI	Cesium Iodide	2	4-6	16	315	1.95	2	4.51	slightly	SPECT/CT/ PET/X-ray
CsI:Tl	Thallium-activated Cesium Iodide	54	45	1000	550	1.79	2	4.51	slightly	SPECT/CT/ PET/X-ray
LSO:Ce ($LuSiO_5$:Ce)	Cerium activated Lutetium Oxyorthosilicate	23	75	40	420	1.82	-	7.4	no	PET
LYSO:Ce ($Lu_{1.8}Y_{0.2}SiO_5$:Ce)	Cerium-activated Lutetium Yttrium Orthosilicate	32	75	41	420	1.81	-	7.1	no	PET
NaI:Tl	Thallium-activated Sodium Iodide	38	100	250	415	1.85	2	3.67	yes	SPECT/ PET
YAG:Ce ($Y_3Al_5O_{12}$:Ce)	Yttrium Aluminium Garnet activated by Cerium	8	28-34	70-100	560	1.82	8.5	4.57	no	X-ray
YAP:Ce ($YAlO_3$:Ce)	Yttrium Aluminium Perovskite activated by Cerium	14-18	35-40	27-38	350-380	1.94	8.5	5.37	no	SPECT/X-ray
ZnS:Ag	Silver activated Zinc Sulfide	50	130	110	450	2.36	-	4.09	no	CT/X-ray

Table 3-2: Important properties of some single crystal scintillators. Adapted from [Hamamatsu Photonics KK PMT's Handbook, p.88, 1999] and [Bicron Crystals Catalog, @2005 Saint-Gobain Industrial Ceramics & Plastics, Inc].

In inorganic scintillators, the scintillation mechanism is characteristic of the crystal electronic band structure. The scintillation occurs as a result of excitation of bound electrons by means of the energy imparted by ionised high-energy electrons inside the scintillator. In so doing, these electrons knocked out from their molecular bond orbitals,

become free to travel through the crystal, leaving the valence energy band and entering the higher energy conduction band. Impurities, called dopants, or activators, create special sites in the crystal lattice with a modified energy band structure. In these regions, energy states are created in the forbidden band, which now constitutes the "band-gap". When free electrons reach an impurity, they pass through the forbidden energy band back to the valence band and the energy released is given off as blue and ultraviolet light, if such a deexcitation mode is allowed. If the transition is radiationless the impurity center becomes a *trap* and the energy is lost to other processes. In other words, when a gamma ray deposits energy in a scintillator, a part of the energy is re-emitted as a large number of scintillation photons. To increase the probability of a scintillation photon being generated during the de-excitation process, small amounts of an impurity are added. Thallium and sodium are often used for this purpose. So one often sees scintillators described as NaI:Tl, which means it is a sodium iodide crystal with a thallium activator, or as YAP:Ce, which is Yttrium-Aluminium Perovskite crystal with a cerium dopant.

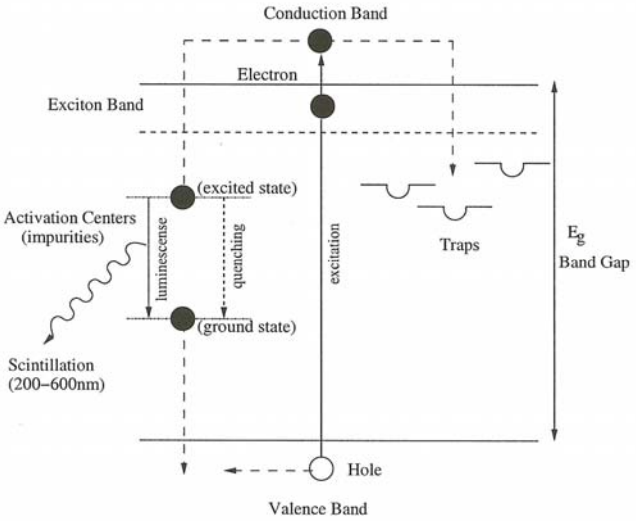

Figure 3-5: Electronic band structure of inorganic crystals. Extracted from [C. Ortigão, 2003].

The photons propagate isotropically and the number of photons emitted is a function of the scintillator material and the gamma-ray energy. From Figure 3-4, it is clear that the photoelectric effect dominates for low energy gamma rays. For both interactions, the amount of scintillation produced by the photoelectric effect is proportional to gamma-ray energy because all the energy of the gamma-ray is given to the orbital electrons.

3.2.1 Detection properties

The scintillator material is an important issue in the design of a gamma camera and is considered the first step in the detector optimization. Commonly, one or two aspects of an application will dominate the choice of material. Properties like market availability, machinability, price, etc, also play an important role when choosing a scintillator. Usually, a high conversion efficiency of a scintillator is the most crucial quantity, but it can be totally degraded if the scintillator is slow, possesses high self absorption, has extremely high index of refraction, or emits light in the spectral region of the low photocathode sensitivity. Applications requiring very high count rates must use crystals with short decay constants. In applications where the scintillator cannot be sealed from moisture, hygroscopic crystals would not be considered. To maximise the absorption probability, a high density and atomic number is required. The refractive index of a scintillator is critical when using light guides and mismatched refractive indices will cause loss of light at the scintillator interface. As can be seen, a lot of aspects must be taken into account when choosing a scintillator for a given application

Considering the origin of the ISPA-tube and the specific detection requirements of our application for small organ diagnosis in nuclear medicine, it is necessary that the scintillator presents the following properties:

- An important light yield output and a low coefficient of auto-absorption allowing the use of a thick scintillator without considerable losses of light. These two parameters allow improving the spatial resolution. They also increase the energy resolution and therefore the efficiency of discrimination of diffused gamma-rays originating from tissue by Compton effect, which degrades the spatial resolution and the signal-to-noise ratio.
- A high effective atomic number to benefit good interaction probability at medium gamma ray energy, which results in a very good photoelectric peak to Compton. Remember that Compton scattering in crystal is not distinguishable from scattering in tissue.
- A high density to absorb appropriate medium energy gamma rays with a minimal thickness of crystal, in order not to damage the spatial resolution.
- A wavelength of maximum emission appropriated to the spectral sensitivity of the photocathode.

- A maximum emission time of the order of the hybrid photodetector peaking time resolution (25 ns).
- Wide temperature performance stability over the room temperature range.

In this project, YAP:Ce has been chosen to be implemented in this detector for its low cost and its optimal properties that satisfy the specifications enumerated above, even if, compared to other scintillators, it has a low atomic number, a high absorption length and a low light yield. YAP means a $YAlO_3$ compound, which is of rhombic perovskite structure produced with cerium as a scintillating dopant (0.1% by weight). Its main disadvantage is the high refractive index, a property that complicates the collection of scintillation light, at least when the crystal is not coupled directly to the entrance window of the tube, which is not the case in the ISPA-tube. The main optical characteristics of YAP:Ce crystals can be found in [R. Pani et al., 1995; F. Vittori et al., 2000; F. de Notaristefani et al., 1998; J. A. Mares et al., 2003; W. Klamra et al., 1998] and are summarised as follows.

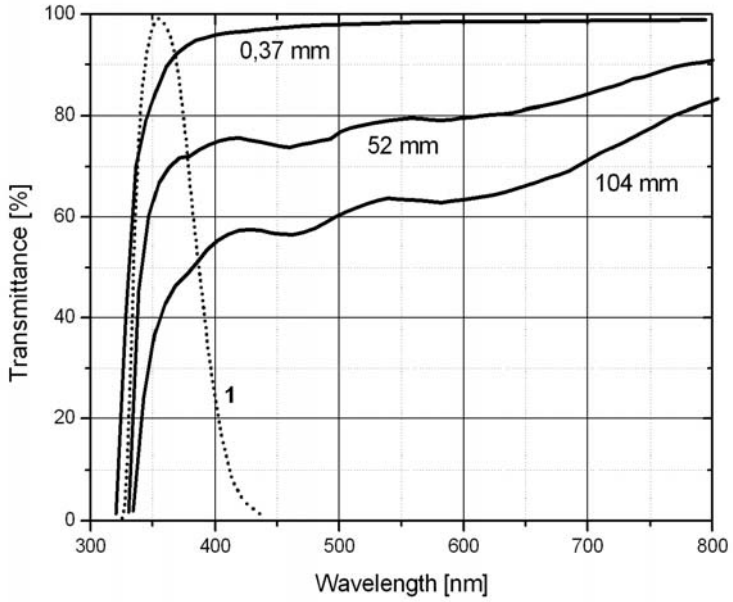

Figure 3-6: Optical transmittance of YAP:Ce (0.37 mm, 52 mm and 104 mm) single crystal scintillators, adapted from [F. de Notaristefani et al., 1998]. The emission spectrum (1), as reported in [C. D'Ambrosio et al. 2000] for a 2 mm-thick YAP:Ce crystal, is shown in relative scale of intensity.

YAP:Ce presents a maximum light yield of 40% compared to NaI:Tl and a minimum scintillation decay time of 27 ns. Its emission spectrum, peaking at 370 nm where the refractive index is equal to 1.94, matches well the spectral response of the S20

photocathode (see section 3.3). Figure 3-6 displays the emission spectrum and the transmittance of YAP:Ce crystal at normal incidence. The transmittance of light through one sample is constant at around 370 nm where YAP:Ce crystals have the luminescence peak. Moreover, it has high hardness and is not hygroscopic making it particularly suited for medium energy gamma ray detection in clinical applications [C. D'Ambrosio et al., 2000; V. G. Baryshevsk et al., 1991; R. Pani et al., 1997; T. Malatesta et al., 1998; M. Moszynski et al., 1999; F. Vittori et al., 1999; F. De Notaristefani et al., 2002; N. Belcari et al., 2004; F. Garibaldi et al., 2004]. LYSO:Ce scintillator would have been a better candidate. It is very hard, not hygroscopic and probably shows the best compromise between light yield (about 75% compared to NaI:Tl) and attenuation length, but it has a high cost and is naturally radioactive, therefore inappropriate for low count rate applications. However, it presents great potential for high counting rate depth-of-interaction position measurements such as in the promising PEM application [J. Varela et al., 2004].

3.2.2 YAP:Ce crystal scintillator operating principles

Following is a description of the scintillation process that occurs in our application with the ISPA-tube.

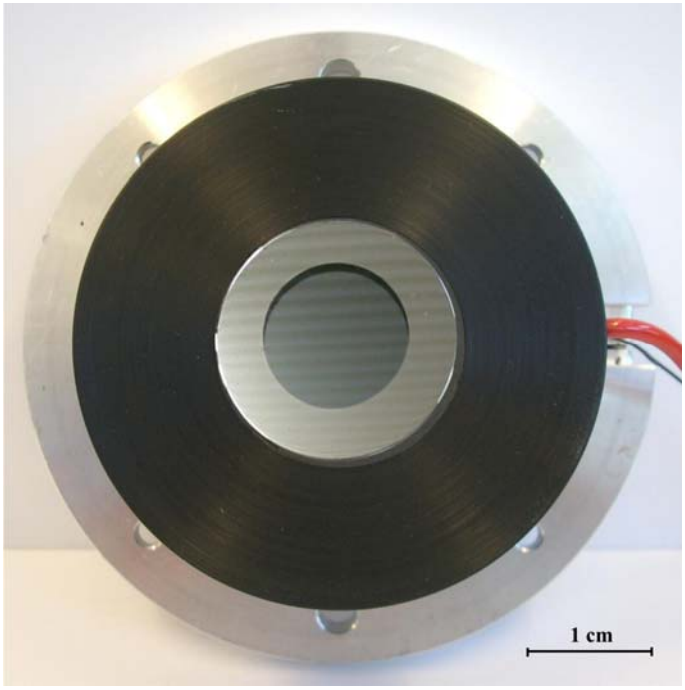

Figure 3-7: Top view of the ISPA detector. The YAP:Ce crystal coated with aluminium in an 'O' ring shape (19 mm-inner diameter) is visible. This aluminium coating extends to the lateral side. About 70% of the incident window (front + lateral sides) is aluminium coated.

The planar scintillation crystal of the ISPA-tube is 31 mm diameter and 2 mm thick. In the back face of the crystal a 19 mm diameter useful area S20 photocathode is deposited. The edges and the front face of the scintillator have been treated and coated with aluminium. This aluminium coating presents an 'O' ring shape to act as a light guide and behave as a reflector (Figure 3-7).

Passing through a hole in the collimator, a photon interacts in the crystal immediately behind that hole. The electrons resulting from the interaction of the gamma ray with the crystal are stopped very close to the point of interaction and consequently the scintillations are produced very close to this point. However, the depth of interaction of the incoming photon depends on its energy and thus, the crystal absorption efficiency will be a function of its thickness. Figure 3-8 shows the absorption efficiency of YAP crystals in function of the photon energy for different crystal thicknesses.

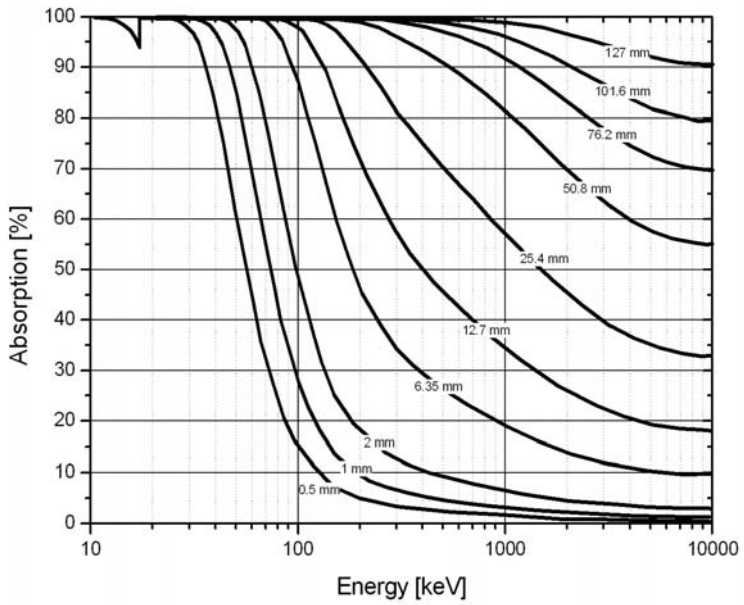

Figure 3-8: Absorption Efficiency of YAP crystals. Extracted from [Bicron YAP:Ce Brochure, @2002 Saint-Gobain Industrials Ceramics & Plastics, Inc].

With a 2 mm thick crystal only 89% of the 60 keV incident photon beam intensity is absorbed. This gives the probability of interaction of the gamma ray photon within the crystal. For example, 1000 incident photons of 60 keV will result on average in 890 absorbed photons. The YAP:Ce crystal implemented in the ISPA-tube, dating from year 1995, presents an intrinsic light output interval around 10 photons/keV. On average, for every 100 eV of energy absorbed from the gamma ray, one light photon is given off.

Thus, for a 60 keV gamma ray energy photon[3], some 600 light photons are produced in a scintillation event.

Meanwhile, a higher crystal thickness would allow better photon absorption efficiency, meaning a high number of light photons and thus a better energy resolution, but the larger the crystal thickness, the wider the lateral dispersion of scintillation light, which degrades spatial resolution. The light transport inside the crystal can be described as an exponential attenuation process, which takes into account both multiple reflections and self-absorption. To maximize light collection, the YAP:Ce crystal is coated with aluminium of 95% reflectivity. With no coating, a light output loss of 23% was observed. With aluminium coating, the loss was reduced to only 11% [C. Ortigão, 2003]. Roughly, a light output lower than 9 light photons per keV absorbed is expected.

As mentioned above, a higher planar crystal thickness means a better energy resolution and a weaker spatial resolution due to lateral dispersion. For very high resolutions, a segmented crystal made of optically isolated pillars could therefore be used, at the cost of a smaller number of photoelectrons, but leading to worse energy resolution [D. Puertolas et al., 1997; D. Puertolas et al., 1998; R. Pani et al., 1994]. Energy resolution is one of the most important characteristics in radiation measurement, and in this application we aim at the best compromise for both.

3.2.3 Monte Carlo simulations

The geometrical properties of the crystal have to be carefully chosen since they influence both the spatial and energy resolutions. Following the numerical simulation of the ISPA-tube, a Monte Carlo code has been developed to evaluate the performance of the crystal YAP:Ce and determine the best compromise between energy resolution, spatial resolution and sensitivity, paying particular attention to three parameters: surface coating, surface treatment and crystal sample thicknesses. Simulating the same geometric configuration of the crystal on the ISPA-tube, we had the opportunity to validate the Monte Carlo code, by comparing simulated results with experimentally acquired data.

For crystal coating the following cases were explored: total absorption or black material, specular reflector (as aluminium with 85% and 95% reflectivity) and diffuse

[3] In the analytical and numerical approaches of the ISPA-tube performance, 60 keV photons energy from the ^{241}Am source used experimentally are considered for results comparison.

reflector or white material (80% and 98% reflectivity). These were compared with the absence of any coating (air). The best performance was achieved with the aluminium coating configuration. For the surface treatment it was simulated from 100% polished to complete roughness (0.05% polished). The best case was achieved with the most polished crystal, although lower polishing had also good results and is less expensive. For a planar YAP:Ce crystal of 3.1 cm diameter with aluminum coating, perfectly polished, and a deposited S20 photocathode, several planar crystal thicknesses were simulated to study spatial resolution, energy resolution and sensitivity. Dependence of energy resolution on the photon beam energy is shown in Figure 3-9. The simulated data shows good agreement with the experimental data obtained with two different radioactive sources, ^{109}Cd (22 keV) and ^{241}Am (59.5 keV) respectively.

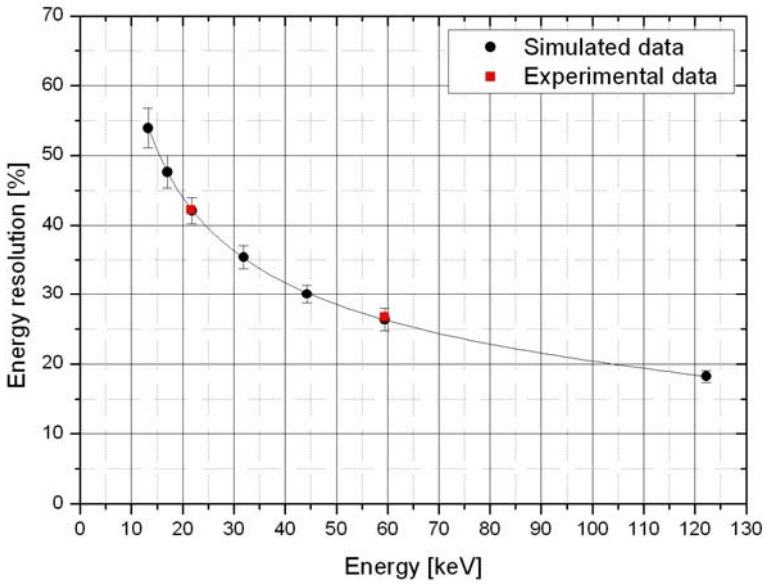

Figure 3-9: Energy resolution as a function of photon energy [C. Ortigão, 2003]. Red dots correspond to experimental results taken with ^{109}Cd and ^{241}Am radioactive sources.

Figure 3-10 and Figure 3-11 show the results for the spatial resolution and sensitivity analysis as a function of the YAP:Ce crystal thickness. This study revealed, for a 2.0 mm thickness crystal and 122 keV incident photons, a spatial resolution (FWHM) of 320 μm with 17% energy resolution and 23% sensitivity.

Moreover, simulations have shown a non-uniformity intensity distribution of scintillating light over the crystal, which has effects on the spatial resolution. In practice, it is known that the response of a scintillation detector falls rapidly near its scintillator edge.

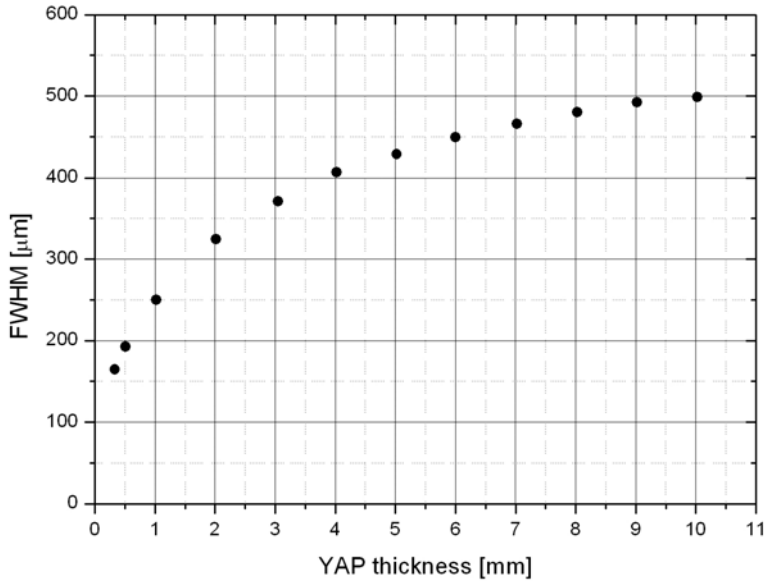

Figure 3-10: Spatial resolution as a function of the YAP crystal thickness for 122 keV energy photons [C. Ortigão, 2003].

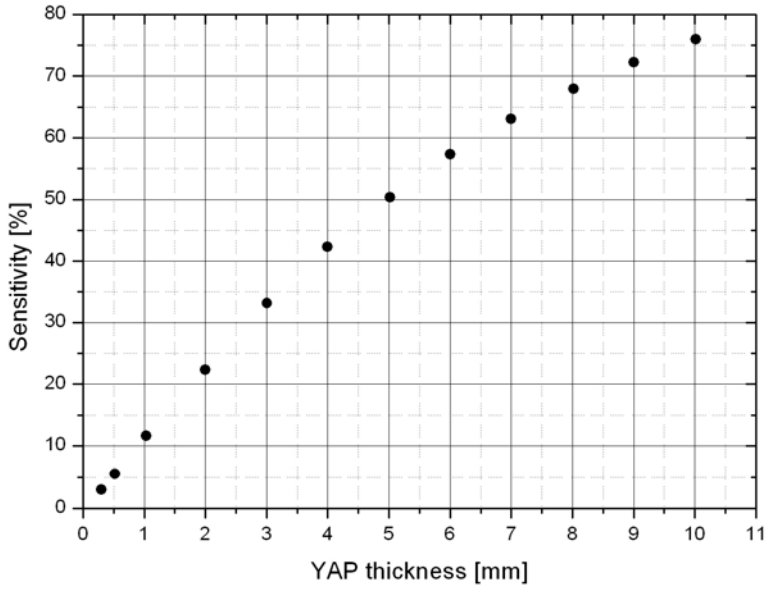

Figure 3-11: Sensitivity as a function of the YAP crystal thickness for 122 keV energy photons [C. Ortigão, 2003].

The scintillator size is usually larger than the field of view to keep the extra region of poor response outside the detector anode. To study this effect, data was simulated with gamma-ray photons spot scanned over the scintillator surface. It turned out for this specific application that, when approaching the crystal edge, the spatial resolution degrades quickly from 440 μm FWHM, at 1.0 cm from the center, to 1170 μm FWHM, at 1.6 cm from the center (Figure 3-12). This study has suggested that the active region

of detection should be smaller than 1.0 cm diameter, which is in agreement with the size of the silicon anode (8.0×6.4 mm^2).

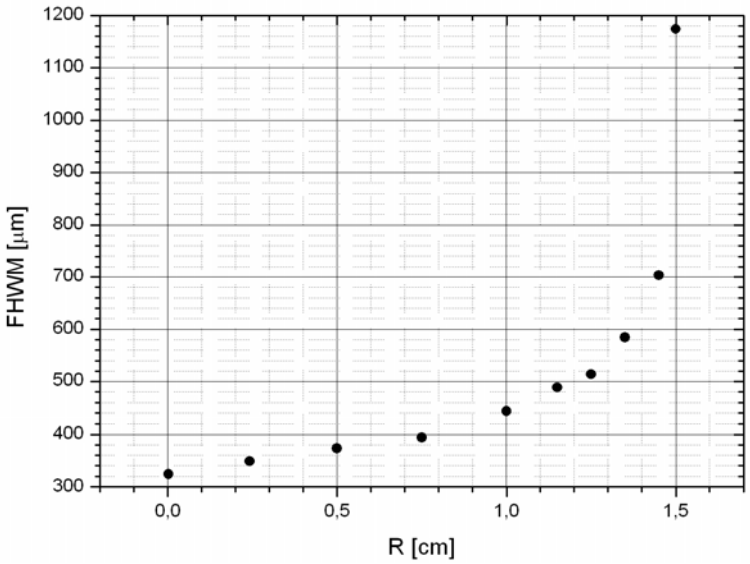

Figure 3-12: Spatial resolution as a function of the radial distance of the source position relative to the center of the crystal [C. Ortigão, 2003].

Recent simulations done with the last GEANT 4 release [S. Agostinelli et al., 2003] has validated the light output that passes through the interface scintillator-photocathode for 60 keV incident photons. Figure 3-13 shows the light output distribution for one and 8771 absorbed photons. For the latter, the incident beam was 10000 photons resulting in a detection efficiency of about 88%. This value is in agreement with that indicated in Figure 3-8.

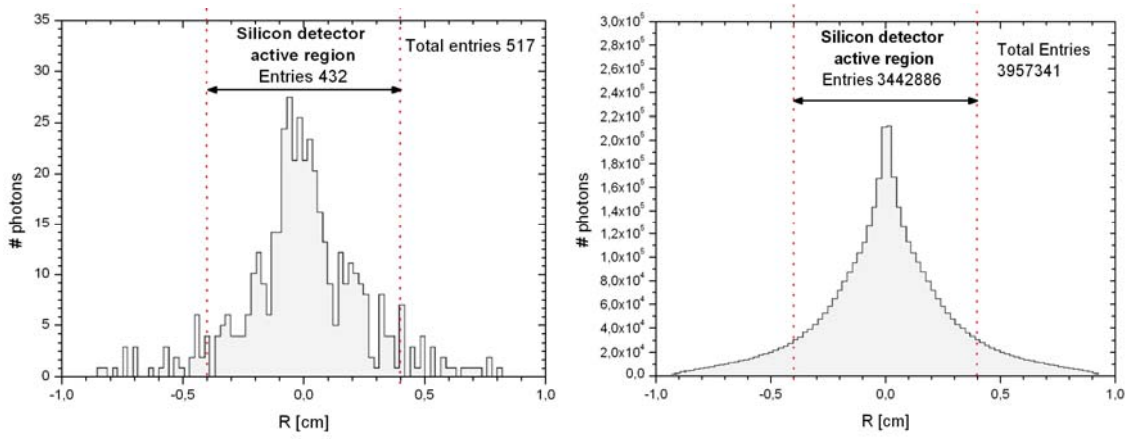

Figure 3-13: Intensity profile of the light photons that penetrate into the photocathode for (left) one and (right) 8771 absorbed gamma photons of 60 keV with centered normal incidence. The fraction of light per unit of energy that goes through the interface scintillator-photocathode and meets the active region of the silicon detector is close to 7 ph/keV. Courtesy of Sónia Rodrigues [Sónia Rodrigues, 2005].

In Figure 3-13, the dotted lines delimit the active region of the silicon detector. It is important to ensure that light-electron conversion outside this area will not contribute to effective detection and thus only the efficient light conversion within the dotted lines is relevant. As result, 3442886 light photons per 8771 absorbed photons of 60 keV were output in the field of view of the silicon detector, resulting in an efficient light conversion of almost 7 ph/keV. This parameter was previously estimated below 9 ph/keV of incident energy without self-absorption corrections.

3.3 Photocathode

The photocathode is a photoemissive semiconductor made of materials from group V, usually antimony (Sb), and one or more metals from alkali group, namely sodium (Na), potassium (K), and caesium (Cs). It converts proportionally the incident light photons into low-energy electrons using the photoelectric effect. In semiconductor band model (see Figure 3-14), when photons strike a photocathode, electrons in the valence band absorb photon energy and become excited, diffusing toward the photocathode surface. If the diffused electrons have enough energy to overcome the vacuum level barrier, they are emitted into the vacuum as photoelectrons.

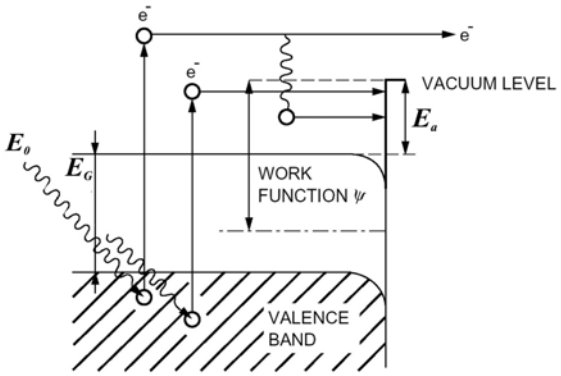

Figure 3-14: Alkali photocathode band model. E_G corresponds to the forbidden-band gap energy and E_a is the electron affinity. Extracted from [Photonis PMT's application book, 2002]

The ejected electrons have then a kinetic energy (E_k) equal to the energy of the incident photons (E_0) minus the work function (ψ) which is an energy difference between the Fermi level and the vacuum level, or simply the energy required to free the electrons from a particular material:

$$E_k = E_0 - \psi \tag{3-1}$$

During manufacture, the photocathode is deposited by vacuum evaporation as a thin layer on the inside of an optical entrance window, and must be thin enough so that the photoelectron escapes without interacting with other photocathode molecules. In working conditions, photocathode applications have to be performed under vacuum because the alkali compounds decompose rapidly in air. They can be constructed as either opaque or semitransparent layers. In opaque cathodes, the electrons are emitted from the illuminated side. In semitransparent cathodes the electrons are emitted from the side opposite to the incident light. The most widely used, and also the one applied in the ISPA-tube, are semitransparent where the cathode surface can be large (from ten to a few hundred millimetres in diameter) and the entrance window on which it is deposited can be flat or curved.

3.3.1 Optical properties

The choice of photocathode material is determined by the spectral range where the device sensitivity is crucial. Sensitivity in some sense refers to the ability of the phototube to transform the photon energy into electrons at the anode. But the overall sensitivity of the phototube naturally depends on the sensitivity of each of its sections, namely at the photocathode stage.

Because it is easier to measure the photocathode current produced in response to the incident light power than to count electrons, the photocathode sensitivity (S_k) is expressed in terms of the current (I_k) produced per unit incident flux Φ (measured either in units of radiometric watt W or photometric luminosity lm) on the window surface:

$$S_k[\mathrm{A/W}] = \frac{I_k[\mathrm{A}]}{\Phi[\mathrm{W}]} \tag{3-2}$$

The cathode sensitivity is not uniform over the whole cathode surface and it is also dependent on the energy of the incoming photon. At a specified wavelength λ, the photocathode sensitivity is given by

$$S_{k,\lambda}[\mathrm{A/W}] = \lim_{d\lambda \to 0} \frac{dI_k[\mathrm{A}]}{d\Phi[\mathrm{W}]} \tag{3-3}$$

Thickness variations within the photocathode also give rise to corresponding changes in the sensitivity of the photocathode and can be a source of resolution loss degradation.

One consideration in selecting a photocathode is to seek a high quantum efficiency *QE* (another way to specify the sensitivity) which is simply the ratio between the number of photoelectrons emitted n_e and the number of incident photons n_γ.

$$QE = \frac{n_e}{n_\gamma} \tag{3-4}$$

Expressed in a probability process we obtain

$$QE = P_\lambda P_S \frac{(1-R)}{\alpha}\left(\frac{1}{1+1/\alpha L}\right) \tag{3-5}$$

where P_λ is the probability that light absorption may excite electrons to a level greater than the vacuum level, P_S is the probability that electrons reaching the photocathode surface may be released into the vacuum, R is the reflection coefficient, α the full absorption coefficient of photons and L is the mean escape length of excited electrons.

The quantum efficiency of any photocathode will be a strong function of wavelength or quantum energy of the incident light, and could never be 100% efficiency due to the fact that there is a minimum escape energy and there are losses in the migration process. The best quantum efficiency of the system is a result of a perfect combination between the optical entrance window and the deposited photocathode, in order to achieve the maximal spectral response of the photocathode at the maximum emission wavelength of the entrance window.

In the ISPA-tube, the optical entrance window (YAP:Ce) has a wavelength of maximum emission at 370 nm and corresponds closely to the maximum quantum efficiency of the deposited multialkali ($SbNa_2KCs$) photocathode, known as S20 type (see Figure 3-15). In this plot we see that the photocathode quantum efficiency was also measured on a quartz window. Both windows are of identical geometrical dimensions and their photocathodes are coated onto them with the same procedure. Their quantum efficiencies differ only due to the different light transmission properties of their windows that limit the spectral sensitivity in the short wavelength region, with cut-off wavelengths ranging from 300 nm for YAP:Ce crystal down to 160 nm for quartz crystal. Cut-off is essentially due to the absorption by the crystal window.

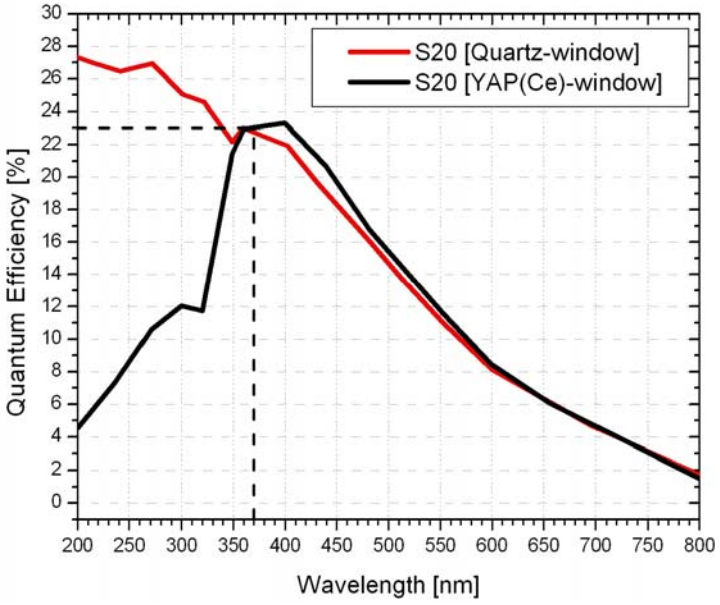

Figure 3-15: Quantum efficiency of the S20-photocathode evaporated on a quartz window and on the YAP:Ce window (measured by DEP[4] company).

Designation	Composition	Type of window	Spectral Range (nm)	Wavelength at maximum quantum efficiency (nm)	Quantum efficiency (%)
Solar blind	CsI	4	115 to 200	130	13
Solar blind	CsTe	2	160 to 320	200	15
S11	$SbCs_3$	1	300 to 650	410	17
Bialkali	SbKCs	1	300 to 650	390	28
		2	160 to 650	390	28
		3	185 to 650	390	28
High temperature bialkali	SbKCs	1	300 to 650	360	19
Multialkali S20	$SbNa_2KCs$	1	300 to 850	360	20
		2	160 to 850	280	23
		3	185 to 850	290	23
Multialkali S20 (ERMA*)	$SbNa_2KCs$	1	300 to 900	570	6
S1	AgOCs	1	300 to 1200	780	0.4
* Extended-red multialkali also called S25					

Table 3-3: Typical characteristics of standard photocathodes. Adapted from [Hamamatsu Photonics KK PMT's handbook, 1999]. *Type of window* ***1.*** *Borosilicate 2. Synthetic silica 3. UV 4.* MgF_2

The S20-photocathode is well-suited to optimise the YAP:Ce crystals scintillation process and presents a spectral response which extends more to the red part of the visible light spectrum. Typical spectral response characteristics of major standard

[4] B.V. Delft Electronische Producten (DEP), P.O. Box 60, 9300AB Roden, The Netherlands

photocathodes are illustrated in Table 3-3. The photocathode quantum efficiency was measured at the factory and found to be 23% at 370 nm.

The quantum efficiency is related to the cathode sensitivity by

$$QE = \frac{n_e}{n_\gamma} = S_{k,\lambda} \frac{hc}{\lambda e} \tag{3-6}$$

where h is Planck's constant, c is the velocity of light in vacuum, and e is the electron charge. With $hc/e = 1.24x10^{-6}$ Wm/A , we thus get,

$$QE[\%] = 124[\mathrm{W \cdot nm/mA}] \frac{S_{k,\lambda}[\mathrm{mA/W}]}{\lambda[\mathrm{nm}]} \tag{3-7}$$

This relation is shown in Figure 3-16, as a function of the incident wavelength for S20-photocathode evaporated on a quartz window and on the YAP:Ce window.

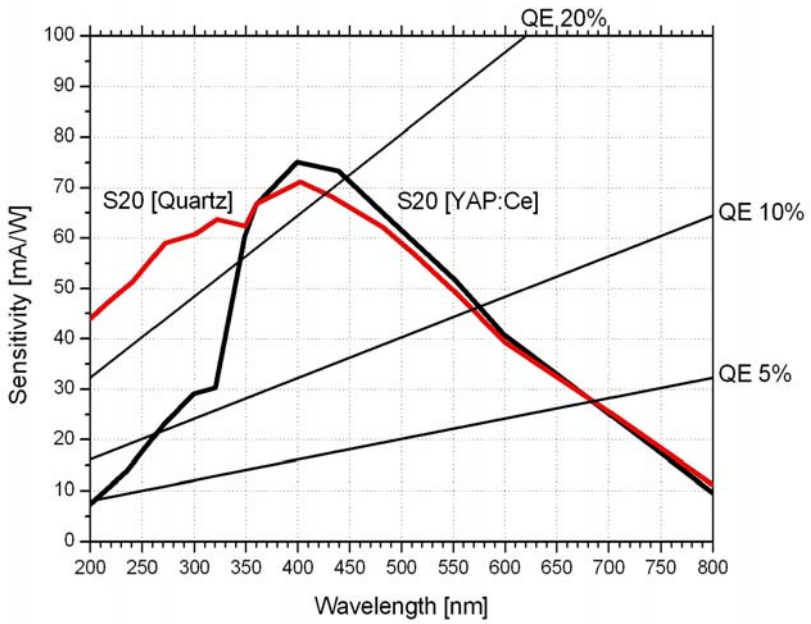

Figure 3-16: Radiant sensitivity of the S20-photocathode evaporated on a quartz window and on the YAP:Ce window.

In fact, the S20-photocathode presents excellent characteristics and has been processed to give optimum sensitivity in which the photoelectric threshold almost coincides with this absorption edge [B. P. Varma and C. Ghosh, 1973; R. Holtomt, G. P.

Hopkins and P. M. Gundry, 1979], making it particularly suited for this application. The reflection, transmission and absorption of a typical S20 photocathode are shown in Figure 3-17 as percentages. More details on S20 optical properties are reported in [S. Hallensleben, S.W. Harmer, P.D. Townsend, 2000].

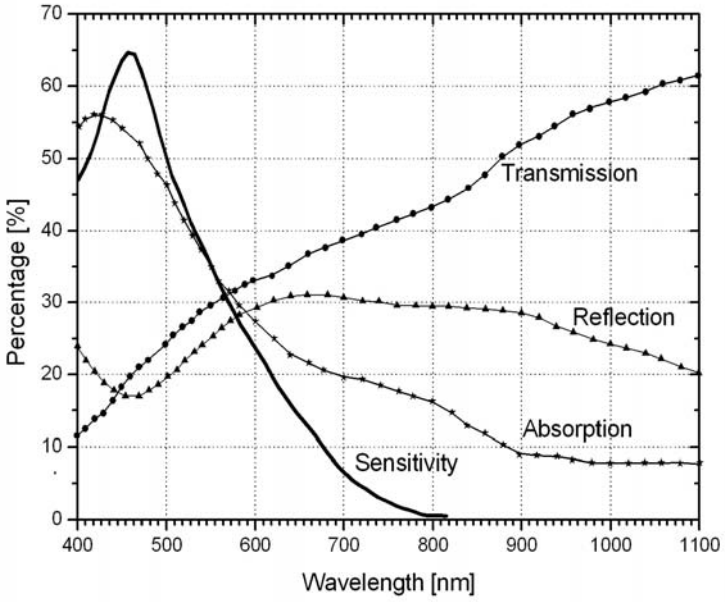

Figure 3-17: Absorption, transmission, reflection and spectral sensitivity of the S20 with wavelength. Extracted from [B. P. Varma and C. Ghosh, 1973].

3.3.2 Dark current

Another consideration in selecting a photocathode that may limit the required accuracy of the measurements if not taken into account, is the dark current. Even when a phototube is operated in absolute darkness a small current is running through the cathode. This current stems from different sources, and under normal operating conditions, a photocathode has two significant sources of dark noise pulses: a high voltage (HV) dependent component of the noise and an additional temperature dependent thermionic emission.

The number of photoelectrons released by the photocathode is proportional to the intensity of the incident light and thus, the total charge produced will be too small to provide a detectable electrical signal. The photocathode material is then placed at high voltage to provide a gain. The HV creates electrostatic discharges on the input window due to dielectric breakdown of the optical medium, and generates scintillation light giving dark pulses to the photocathode. There is also the possibility of field emission if the voltage between the cathode and the anode is extremely high, this can help electrons

to escape from the surface and a pulse is created. If they have enough charge to appear as a valid event, the center-of-gravity of the signals will be registered as a photon, indistinguishable from the real ones.

Thermionic emission depends on the metals composition of the cathode [W. Fisher, 1999] and occurs when an occasional electron gains an energy above the work function. This electron can then be emitted from the photocathode, accelerated by the HV field and experiences the same gain as a normal photoelectron. Then a signal will be created that is large enough to be observed.

Of the two causes of dark current, field emission is the one that predominates for high supply voltages above 3 kV. At room temperature, an S20 photocathode has a typical dark noise specification of 6.000 $e^-/cm^2 \cdot s$ which decreases rapidly with temperature (see Figure 3-18).

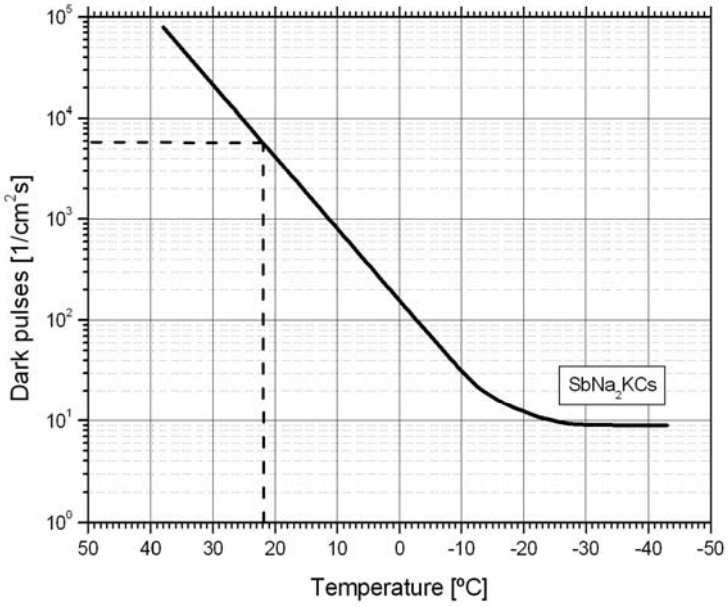

Figure 3-18: Number of dark current pulses per second per centimeter squared as function of temperature for S20-photocathode. Extracted from [Photonis PMT's application book, 2002].

Cooling the tube can therefore drastically reduce the dark current counting rate. However, problems may arise with the water vapour condensation on exposed cold surfaces that can increase photocathode electrical resistance, which can distort the electrostatic field between the photocathode and anode and may lead to a loss in photoelectron collection efficiency. In general, the effects of the dark currents are small and can either be accounted for with an *empty* measurement (in darkness) or sorted out by applying an amplitude discriminator threshold.

3.3.3 S20 photocathode operating principles

A description of the photoemission process that occurs in our application with the ISPA-tube follows.

Scintillation light from the YAP:Ce crystal of peak wavelength $\lambda = 370\,\text{nm}$ strikes the S20-photocathode. Only a fraction of it releases energy to the electrons in the material and will contribute to the photoemission process, the rest is either reflected or passes through it. S20 optical properties have been studied in detail and are well known [P. D. Townsend, 2000; S. W. Harmer and P. D. Townsend, 2003]. Figure 3-19 shows the variation of the absorption coefficient α as a function of the wavelength λ of the incident photons for the S20-photocathode. From this plot we can estimate an absorption coefficient α greater than $10^6\,\text{cm}^{-1}$ for a wavelength $\lambda = 370\,\text{nm}$.

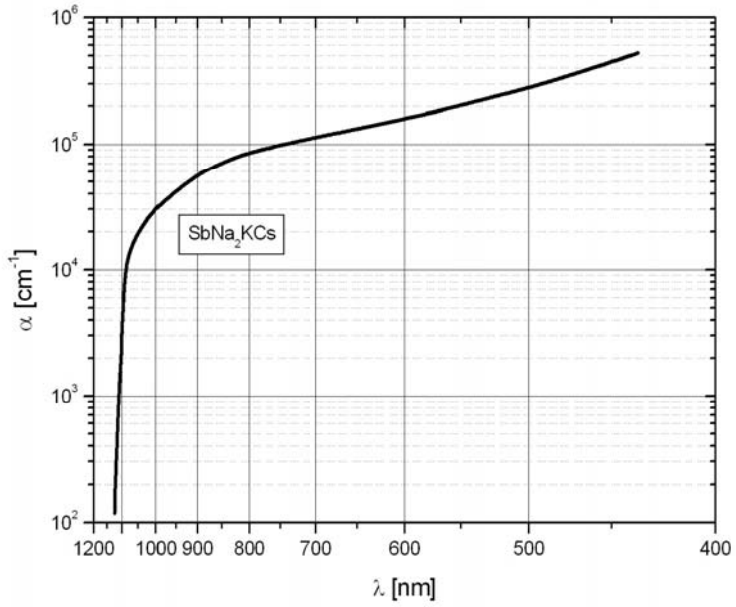

Figure 3-19: Absorption coefficient α as a function of the wavelength λ of the incident photons for the S20 photocathode. Extracted from [Photonis PMT's application book, 2002].

Using this absorption coefficient, the intensity of the photons at a depth t, $I(t)$, for an incident intensity I_0 is given by

$$I(t) = I_0 \exp(-\alpha t) \tag{3-8}$$

where the transmission efficiency can be written

$$T[\%] = \exp(-\alpha t) \tag{3-9}$$

The exponential attenuation coefficients apply for x-rays as well as photons in the visible portion of the electromagnetic spectrum. Figure 3-20 represents this function where we see that a few tens of nanometres of photocathode are enough to absorb the greater part of the incident radiation.

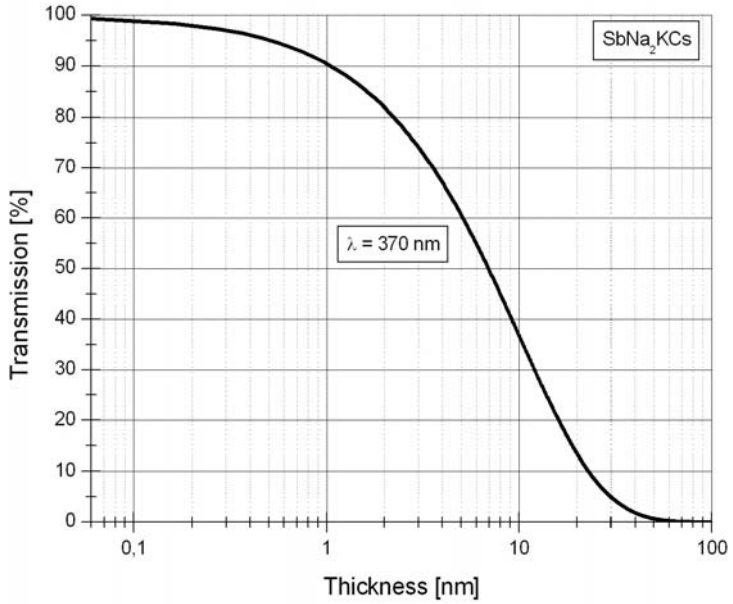

Figure 3-20: Transmission efficiency as a function of the thickness of the photocathode S20 for an incident light wavelength of λ = 370 nm.

The electrons will receive $E_0 = hc/\lambda = 1240 \text{ eV}\cdot\text{nm}/370 \text{ nm} = 3.35 \text{ eV}$ when they absorb a photon. With an energy E_0 above the thermionic work function Ψ, the photoemission will occur. The value of the S-20 photocathode work function was not available from the factory, as the creation of a photocathode does not allow for manufacturers to create a precisely uniform layer of metal and also, the exact composition of the photocathode can vary across the photocathode itself. However, photocathodes with caesium compounds usually present a work function of about 1.4 eV. If we now calculate the initial kinetic energy of the migrating electron, Equation (3.1) results in

$$E_k = E_0 - \psi = 3.35 - 1.4 \cong 1.95 \text{ eV} \tag{3-10}$$

As stated above, the photocathode must be thick enough to increase the photoemission efficiency, but it must also be thin enough, so that the photoelectron can escape with a minimum interaction within the crystal lattice (creation of phonons). The average energy loss per electron-phonon collision is about 0.05 eV, and the minimum mean free path between two collisions is 2.5 nm. If we calculate the escape depth of the photoelectron from these conditions, we obtain that the maximum thickness of the photocathode shouldn't surpass few tenths of nanometers (20 to 40 nm for transmission mode S20). This result is a trade-off between high absorption and high electron escape probability.

Under these conditions, part of the electrons in the photocathode that absorb the energy from the light photons will diffuse through the material in the same direction as the incident photon, loosing some of their energy, and reach the surface with sufficient excess energy to escape from it. The mean radial emission energy of the S20 photocathode is 0.3 eV [E. H. Eberhardt, 1968].

In section 3.2.2 (YAP:Ce crystal scintillator operating principles), we demonstrated that approximately 7 light photons will reach the photocathode per keV of energy absorbed. With a S20 photocathode quantum efficiency of 23% we obtained an electron conversion efficiency of 1.6 photoelectron/keV.

3.4 Electrostatic tube

The ISPA-tube is a vacuum-sealed ($10^{-9} \div 10^{-10}$ mbar) cylinder that combines the photocathode, for light conversion into photoelectrons as seen previously, with a silicon anode which provides charge signals via photoelectron absorption. The photocathode is first deposited on the crystal scintillator window. This window is then used to seal hermetically a ceramic container which already contains the silicon detector mounted onto a ceramic carrier (Figure 3-21). A high voltage electric field applied between them accelerates the generated photoelectrons in the proximity-focusing mode to 25 keV on to the reverse-biased anode. Proximity focusing mode means that the gap between photocathode and silicon detector is small and the electrostatic field configuration is parallel, normal to the anode plane. There is no demagnification and thus the photosensitive area of the detector is limited by the size of the silicon sensor so that the 1:1 image on the sensor corresponds to the photon pattern on the photocathode.

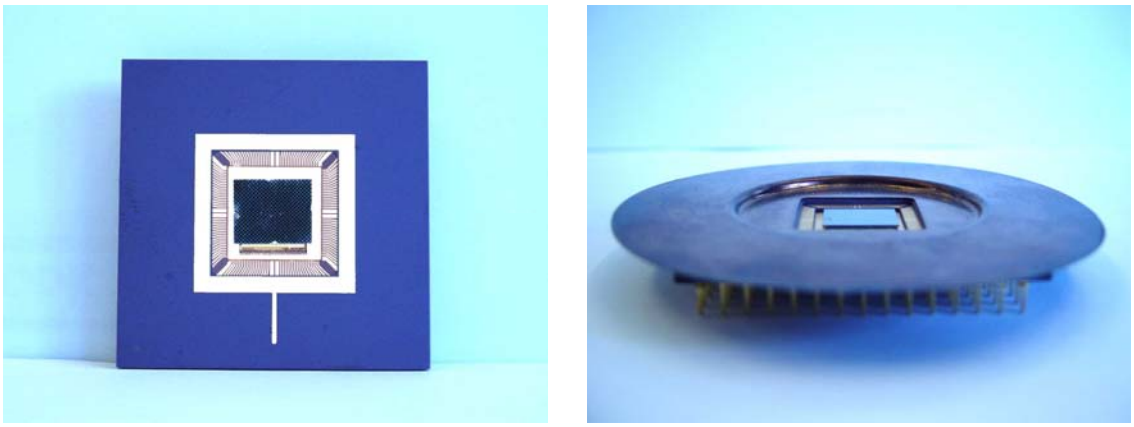

Figure 3-21: (left) Photograph of the silicon detector mounted and wire-bonded onto the ceramic carrier manufactured by Kyocera[5] in Japan. It is of the Pin Grid Array (PGA) type. An O-ring plate/cover (right) is then glued onto the ceramic carrier for integration on the electrostatic tube and for grounding purposes.

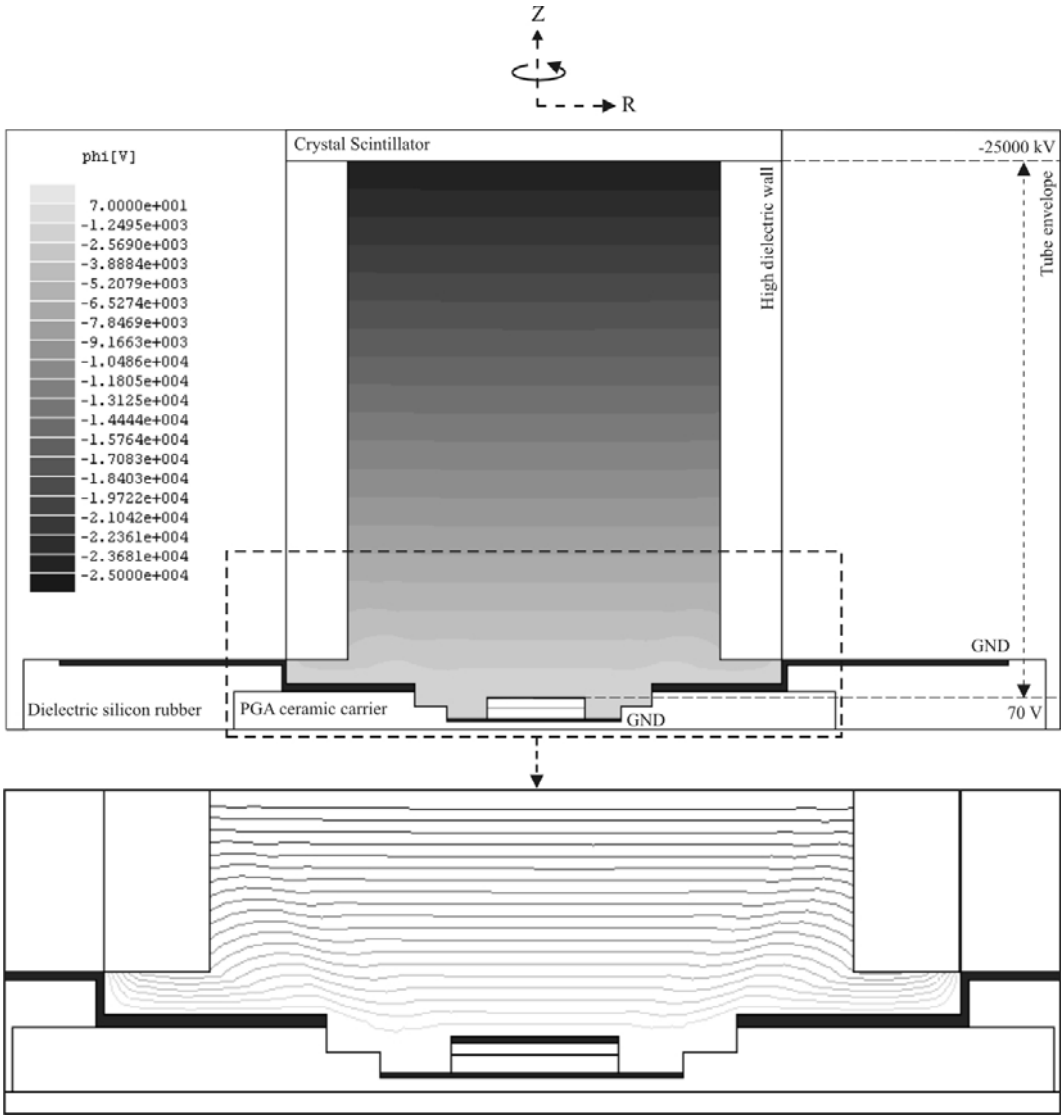

Figure 3-22: Distribuition of equipotential lines along a simple design reproducing of the ISPA proximity focussing tube. Maxwell S-V version 3.1.04.

[5] Kyocera Corporation; http://global.kyocera.com/prdct/semicon/ic_pkg/pga.html

To visualize the equipotential line distribution inside the proximity focusing tube configuration, the electrostatic field calculation has been performed in cylindrical coordinates with Maxwell-SV 2D electric field simulation program by Ansoft[6] (see Figure 3-22). The equipotential lines range from -25 kV (at the cathode level) to 70 V (at the anode). This simulation shows an uniform electric field with a small distortion of the equipotential lines near the inner boundaries at the bottom of the tube. It is caused by edge effects and does not affect the active region. This result has been considered satisfactory to demonstrate the feasibility of a proximity focusing tube satisfying the requirements of 1:1 imaging.

To preclude leakage current through the scintillating entrance window, the collimator placed on top of the scintillator is biased to the same potential as the photocathode. For high operating voltage, a rise in the ambient humidity may also increase the leakage current by several orders of magnitude. For this reason and still more important, human handling, high voltage shielding is an important component of the gamma camera design. A high dielectric polymer (polypropylene) envelope is the choice to insulate the external camera housing (Figure 3-23). The present electrostatic tube was developed in close collaboration with the company Delft Electronic Products (DEP).

Figure 3-23: Photograph of the proximity focusing tube and the polypropylene casing. This HV shield casing has a centered hole to adapt the collimator. Three springs are visible around it and they are useful to lean the collimator on the scintillator. The groove cavity is for the tube and collimator high voltage cables.

[6] Ansoft Corporation; http://www.ansoft.com/

3.4.1 Trajectories in the electric field

Electrons emitted by the S20 photocathode are generated within the proper kinetic energy ranges 0 ÷ 1.95 eV (see section 3.3 Photocathode) and are assumed to follow Lambert's cosine law

$$I = I_0 \cos\varphi \tag{3-11}$$

where I_0 is the radiant intensity along the line φ (see Figure 3-24). They are emitted with a Maxwellian velocity distribution with most probable velocity

$$v_p = \left(\frac{2\tilde{E}_{kin}}{m_e} \right)^{\frac{1}{2}} \tag{3-12}$$

where m_e is the electron rest mass and $\tilde{E}_{kin}$ is the mean radial emission kinetic energy.

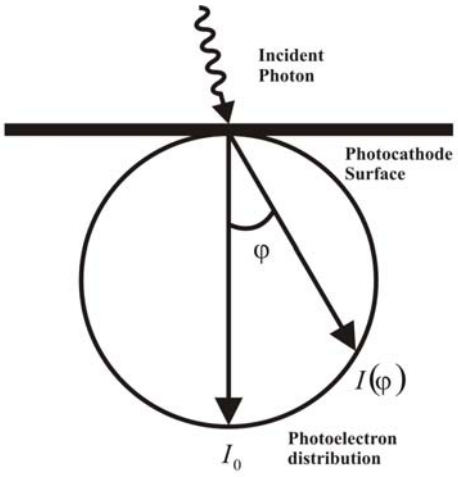

Figure 3-24: Lambertian distribution of photoelectron intensity

Emerging from the photocathode surface, electrons are accelerated by the electric field straight down to the anode. Those entering the parallel electric field region with an angle φ with respect to the surface normal will follow a parabolic trajectory. From Equation (3.14), derived from the range equations, we can calculate how far (radially from its origin) the electron travels before hitting the anode, located at a distance d .

$$x_{d,\varphi} = 2d \left(\frac{\tilde{E}_{kin}}{eU} \right)^{\frac{1}{2}} \sin\varphi \tag{3-13}$$

where eU (eV) is the electrostatic potential between cathode and anode.

Using d =32,5 mm, eU = 25 keV and $\tilde{E}_{kin}$ = 0.3 eV, Figure 3-25 shows the photoelectron spatial deviation at silicon anode measured relative to the emission angle normal to the photocathode.

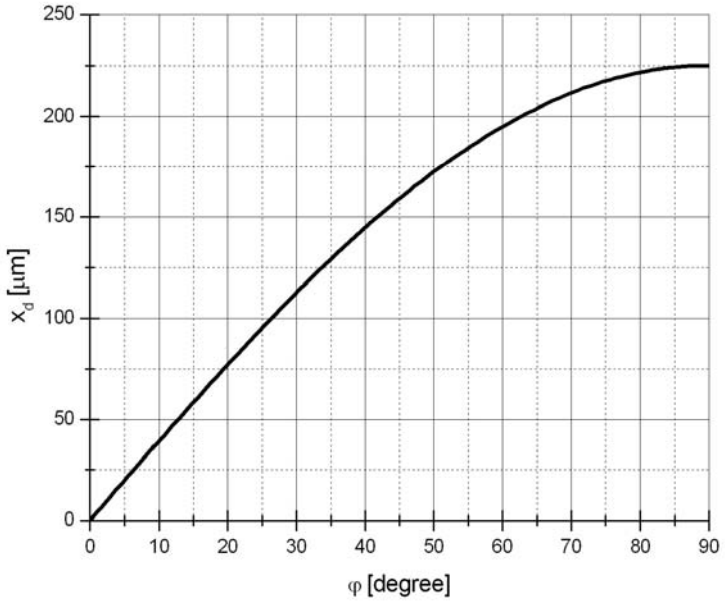

Figure 3-25: Photoelectron spatial deviation at silicon anode as function of photocathode surface emission angles. For a maximum emission angle of $\varphi = 90°$, the spatial deviation is 225 µm.

3.5 Silicon anode

Silicon pixel detectors are used to measure accurately the position as well as the energy of particles incident upon them. They are usually fabricated on high resistivity n-type silicon wafer with a donor concentration (source of electrons) of the order of $N_D \approx 10^{11}$ cm^{-3}. Through ion-implantation, p^+ regions are formed, creating diodes corresponding to individual pixels. The p-region is highly doped with an acceptor concentration (positive holes) of $N_A >> N_D$. Operated at reverse bias (a forward bias would result in permanent current flow), the depletion region can be expressed by

$$d = \sqrt{\left(\frac{2\varepsilon V}{eN_D}\right)} \tag{3-14}$$

where ε is the silicon dielectric constant (Table 3-4), e the electron charge (1.60x10^{-19}C) and V the bias voltage. If the bias voltage is large enough, the depletion layer extends throughout the whole silicon bulk thickness.

General properties of silicon	
Atomic number	14
Atomic weight	28.09
Density	2.33 $g.cm^{-1}$
Melting point	1410 ºC
Electrical properties	
Energy gap between conduction and valence band at 20ºC	1.13 eV
Dielectric static constant $\varepsilon_r\varepsilon_0$ = 11.9 x 8.854 x 10^{-2} $pF.cm^{-1}$	1 $pF.cm^{-1}$
Diode capacitance at 1 nm depletion depth	10 $pF.cm^{-2}$
Resistivity range	1-10 kΩ.cm
Average lifetime of electron-hole pairs until recombination	1 ms
Charge collection time for electrons	4.5 $ns.(kV/mm)^{-1}$
Charge collection time for holes	10 $ns.(kV/mm)^{-1}$
Mobility of electrons	1450 cm^2 V s^{-1}
Mobility of holes	450 cm^2 V s^{-1}
Optical properties	
Light transmission > 95% spectral range	1.3 - 6.7 μm
Maximum spectral response of Si photodiodes	0.8 – 1.0 μm
Quantum efficiency between 0.5 and 1.0 μm	70 – 80%
Radiation properties	
Energy required to create an electron-hole pair	3.6 eV
Yield of electron-hole pairs	278 keV^{-1}
Radiation length	9.36 cm
Gamma conversion length	12.03 cm
Nuclear interaction length	45.5 cm
Stopping power (d*E*/dx)	0.71 $MeV.cm^{-1}$
Energy loss of minimum-ionizing electrons after 300 μm	21.5 keV
Range of 20 keV electrons	4.0 – 5.0 μm
Fraction of backscattered electrons at 20 keV incidence energy	0.17
Charge deposition of minimum-ionizing electrons within 300 μm	4 x 10^{-15} C

Table 3-4: Properties of silicon diodes. Extracted from [C. D'Ambrosio and H. Leutz, 2003].

When ionizing radiation interacts within the depletion region, free electrons and free holes are created at the average rate of one per 3.64 eV (room temperature) incident energy, independently of the type and the energy of the ionizing radiation. Electrons are quickly swept (compared to the holes) towards the n-type electrode, while holes are

swept slowly towards the p-type electrode. This rate is on average, not exact, by due to the fact that energy entering the semiconductor detector is partitioned between breaking covalent bonds and lattice vibrations or phonon production. The variance in the number of electron-hole pairs created is given by the Fano factor for silicon (F~0.12) times the number of pairs created.

At low energy radiation, photoelectrons are fully stopped within tens of microns across the semiconductor and, for convenient radiation detection, the detector should be operated in full depletion mode. The number of the charge carriers created, i.e. the gain of the device is approximately proportional to the total energy of the incident radiation. To a first approximation, the gain is given by

$$G = \frac{eU}{3.64} \tag{3-15}$$

At eU = 20 keV gap voltage, the gain amounts to 5495 e^-. For a silicon wafer of 300 μm, the response time of this type of detector is fast. Charge collection can be performed in less than 10 ns, allowing high counting rates. Table 3-4 gives the general characteristics of the silicon structure.

3.5.1 The Omega3/LHC1 sensor chip

The pixel silicon detector anode of the ISPA-tube is the Omega3/LHC1 sensor chip developed in 1995/96 in the framework of the RD-19 Collaboration at CERN for LHC experiments. The sensor chip, built by Canberra Semiconductor N.V.[7], measures 8.3 × 10 mm^2 and comprises a matrix of 16 × 128 pixels of dimensions 50 × 500 μm^2.

One of the 128 rows has been implemented for the leakage current detection in the sensing circuit cells providing a compensation current for each of the 16 columns. The active area is then 8 × 6.35 mm^2. Figure 3-26 shows a photograph of the Omega3/LHC1 pixel sensor chip where the pixel column structure with the surrounding guard-ring is visible. The bottom figure shows a zoom-in of the pixel cells implants. In Figure 3-27, a schematic view across the sensor chip is shown and in Table 3-5 some details regarding the sensor chip processing is presented.

[7] Canberra Semiconductor N.V., Lammerdries 25, B-2250 Olen, Belgium

The pixel matrix is hedged by "dummy" diodes connected by thin lines to a surrounding 230 μm wide guard-ring, all connected to ground. This design ensures identical electric field conditions throughout the chip and protects the active pixel matrix from leakage currents, especially those caused by imperfections in the borders of the chip after being diced. Figure 3-28 illustrates the current-voltage characteristics at room temperature. The detector capacity is 90 fF [Iztok Ljubljana, 2000], and the leakage current for an applied detector bias of 70 V is around 5 pA/pixel.

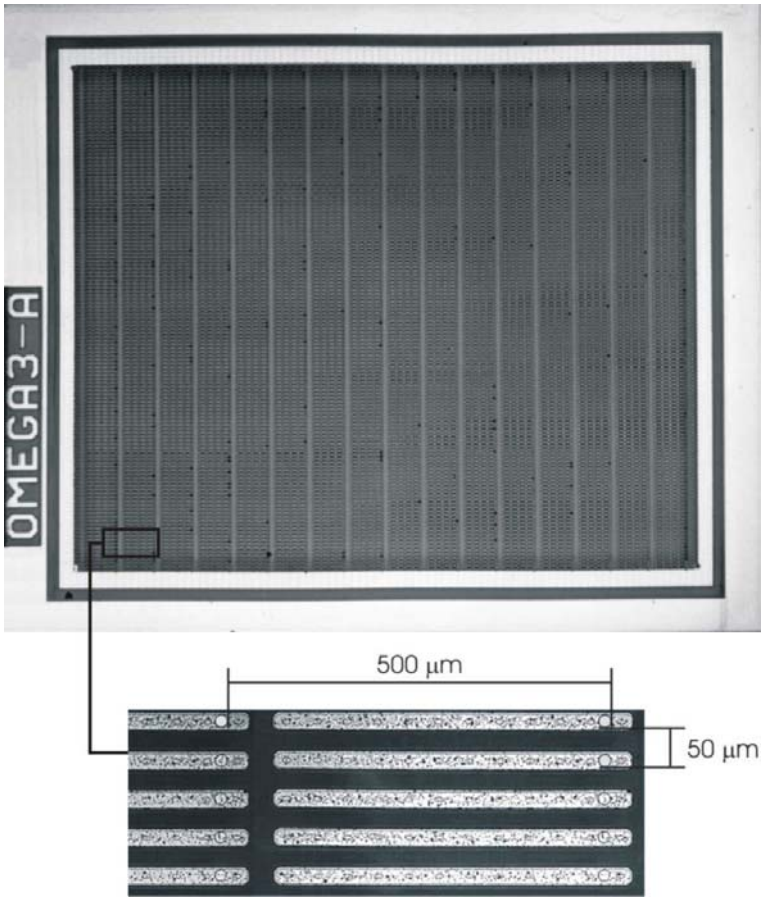

Figure 3-26: (top) Photograph of the OMEGA3/LHC1 sensor; (bottom) Photograph of the pixel cells.

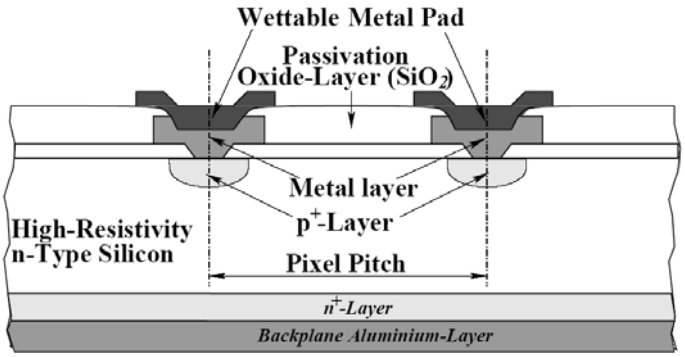

Figure 3-27: Cross sectional view of the sensor chip (sizes not to scale).

Wafer resistivity	17500 [Ω cm]
Wafer $N_D - N_A$ (n-type)	2.5 x 10^{11} cm^3
Wafer thickness	300 μm
Wafer diameter	13 cm
p^+-implant thickness	500 nm
Rear side n^+-implant thickness	500 nm
Aluminium-layer thickness	800 nm
Passivation-layer thickness	1-2 μm

Table 3-5: Characteristics of the sensor chip processing for the OMEGA3/LHC1 detector [Iztok Ljubljana, 2000].

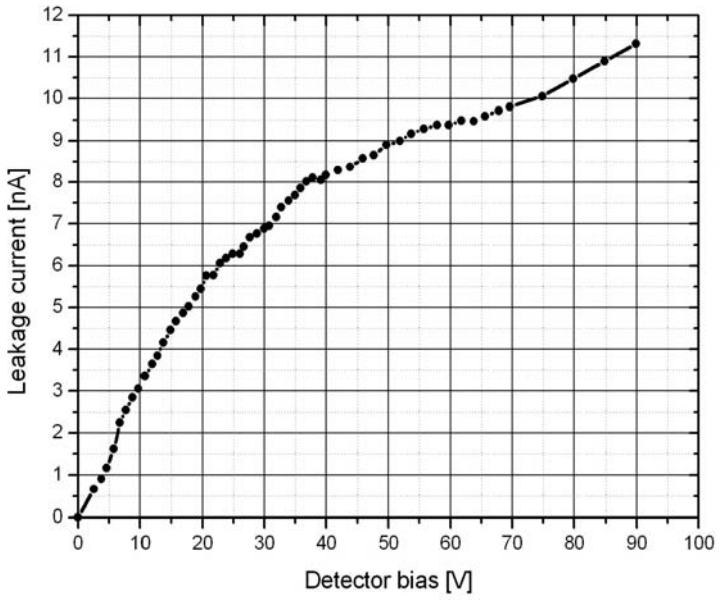

Figure 3-28: Current-voltage characteristics of the reverse biased sensor chip. Extracted from [Iztok Ljubljana, 2000].

3.5.2 Photoelectron response

To predict theoretically the signals observed in the silicon detector, the photoelectron detection efficiency has been evaluated by means of a scattering Monte Carlo program specifically designed for low energy beam interactions in solids (CASINO[8]). The study carries out energy loss through elastic/inelastic interactions and backscattering through elastic interactions, formation and diffusion of the electron cloud, and charge sharing. Based on this simulation model, a detailed description of the analysis follows.

[8]CASINO; http://www.gel.usherbrooke.ca/casino/index.html, 2006

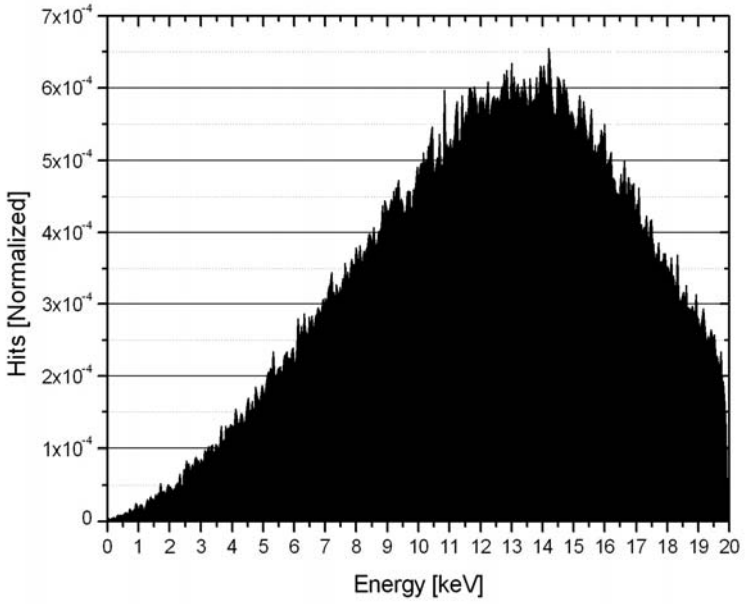

Figure 3-29: Backscattering distribution of 20 keV incident electrons from the silicon detector back-plane. The total backscattered energy is 2.1 keV. Simulated with CASINO version 2.42.

When photoelectrons with energies of 20 keV impinge on the silicon sensor back-plane, there is a probability that the photoelectron will be backscattered into the vacuum, escaping from detection after a parabolic motion in the electric field. Simulation results give a backscattering probability of 16.8% which is in good agreement with experimental data given in [E. H. Darlington, 1975]. The backscattered electrons have an energy distribution from a few eV up to the accelerating voltage (20 keV) (Figure 3-29). Integrating this distribution gives a result of a total backscattered energy leaving the detector of $E_B = 2.1$ keV.

Only 89.5% of the non backscattered electrons will then release their full energy E_0 on the anode, but part of this energy will not contribute for charge signal generation since there is an energy loss E_D within the ohmic layer of the silicon detector backplane. The ohmic side is formed by a thin 500 nm-thick n+ implant and in fact, the photoelectrons lose part of their energies in passing through this dead surface before reaching the depletion region of the diode. According to the simulation, at 20 keV incident energy this absorption results in ~1.8 keV. Hence, the average useful energy E_U for charge signal generation is given by

$$E_U = E_0 - E_B - E_D = 20 - 2.1 - 1.8 = 16.1\,\text{keV} \qquad (3\text{-}16)$$

Figure 3-30 shows the transmitted energy beyond the ohmic layer.

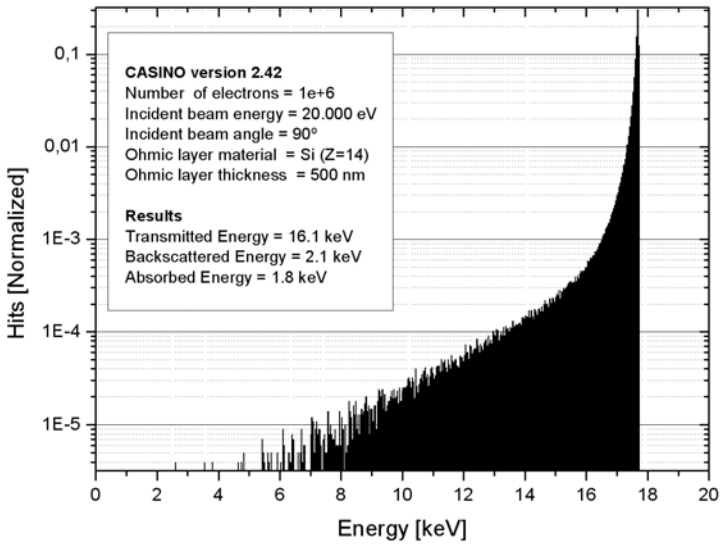

Figure 3-30: Intensity distribution of the transmitted energy through the 500 nm-thick ohmic layer of the silicon detector back-plane (CASINO version 2.42). The results are normalized for 1 electron of 20 keV.

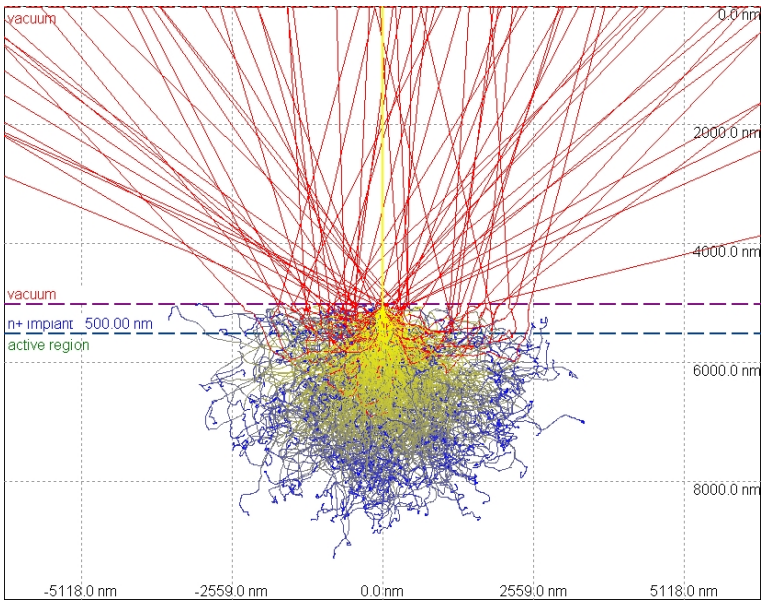

Figure 3-31: Interaction volume in silicon at 20 keV, simulated with CASINO version 2.42. Red lines correspond to backscattered electrons. The absorption energy varies from 20 keV (yellow) to 3.62 eV (blue). An initial electron cloud of $r_i \sim 2.5$ μm lateral spread radius is formed.

Assuming a full depletion voltage operation mode, the process of electron-hole pair multiplication occurs in the depleted layer near the back surface of the device and along the path of the photoelectron. A Monte Carlo simulation schematic of the interaction process can be seen in Figure 3-31. The actual shape of the interaction volume is approximately round with an initial radius of $r_i \sim 2.5$ μm. A density depth distribution

(Figure 3-32) shows that photoelectron penetration ranges a maximum of ~4 μm in the active region with the beam incident perpendicular to the sample.

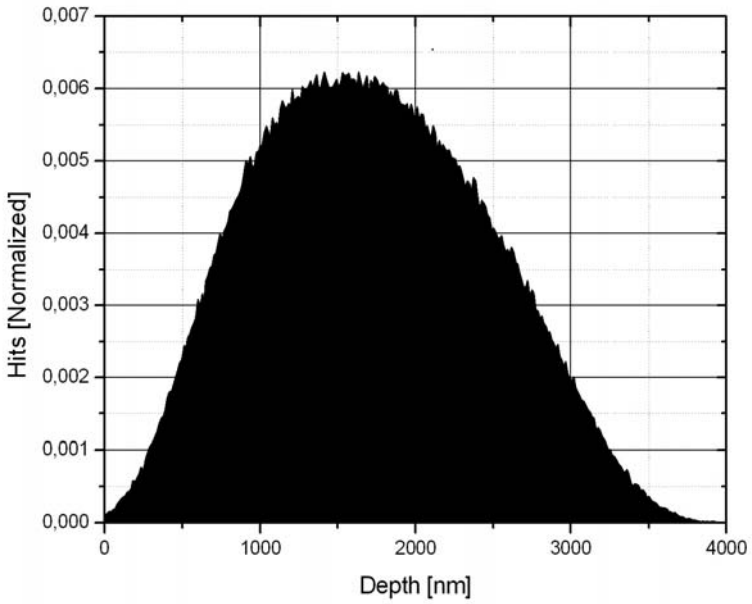

Figure 3-32: Photoelectrons density depth profile along the incident track direction, simulated with CASINO version 2.42.

From there the carriers diffuse until they are collected in the potential wells. Electrons are quickly collected at the back-plane where they will contribute with analog information (energy distribution), while holes give position information as they are collected by individual pixels. During holes diffusion process there is some lateral spreading, and the final cloud size determines how the charge of the cloud is split between adjacent pixels. The lateral spread of this diffusion can be approximated by a Gaussian distribution with a standard deviation given, according to [John A. Nousek et al., 1999], by

$$\sigma_d = d\sqrt{\frac{2kT}{eV}} \tag{3-17}$$

where k is the Boltzmann constant ($1.38\text{x}10^{-23}$ $m^2.kg.s^{-2}.K^{-1}$), T is the temperature (300 K), and e is the electron charge ($1.6022\text{x}10^{-19}$ C). It is clear that increasing the electric field across the full sensitive volume improves the charge collection speed and minimises the charge spread. At an operating bias of $V = 70$ V and detector thickness d of 300 μm, we get $\sigma_d = 8.2$ μm. With a 99.73% uncertainty limit, the diffusion radius of

the major axis of this cloud volume would be $r_d = 3\sigma_d = 24.6$ μm. The final cloud radius r_f is then calculated according to the formula

$$r_f = \sqrt{r_i^2 + r_d^2} = \sqrt{2.5^2 + 24.6^2} = 24.7 \text{ μm} \tag{3-18}$$

A representative drawing of the charge sharing process is shown in Figure 3-33.

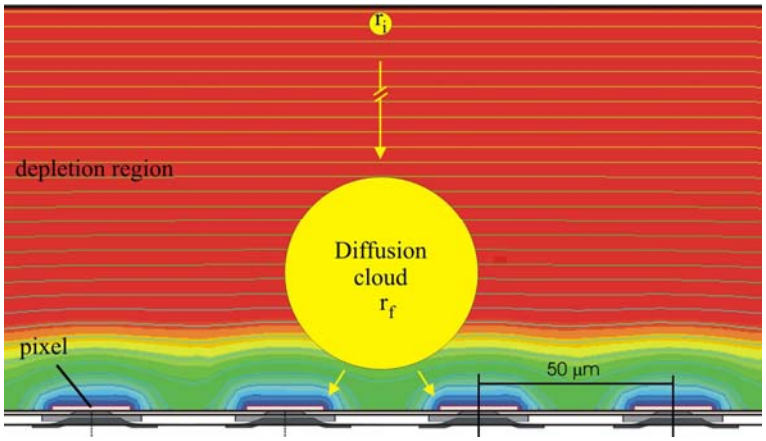

Figure 3-33: Maxwell electric field calculation for the reverse biased (70V) OMEGA3/LHC1 pixel detector with the appropriate geometry, electrode pattern and potentials. A schematic drawing of the final cloud radius due to the holes diffusion process is presented. Besides the detector thickness, sizes are to scale.

This simulation shows that charge sharing will occur in adjacent pixels or "double pixel cluster" because electrons from the cloud will be swept by the electric field toward more than one pixel. The simulation also confirms that charge splitting occurs between pixels with no signal loss in the space-charge layer. Assuming that the charge is deposited uniformly along the track we can estimate the amount of charge sharing using a model proposed in [A. Belau et. al., 1983] by simple geometrical considerations. The fraction of charge sharing between neighbouring pixels which occur in a region of ~30 μm on the pixel boundaries is equal to

$$\frac{(50-30)\times(500-30)}{50\times 500} = 37.6\% \tag{3-19}$$

Finally, the average number of electron-hole pairs created must be estimated in order to evaluate the absolute gain and set the threshold value. With 20 keV incident photoelectron, we saw that the maximum useful energy that will create electron-hole pairs is 16.1 keV (Equation 3.15) giving a most probable signal of 4423 e^-. Charge-

sharing effects between two adjacent cells may reduce this to half in a single channel (not taking into account charge lost) and the electronics must therefore be sensitive to this level of signal, selecting an operational threshold of or above 2212 e^-. This result is purely the product of simulation study and depends on the amount of charge generated, the location of the hit, and the detector bias and geometry.

3.5.3 Spatial resolution

Theoretically, and not taking into account charge sharing, the spatial resolution of a binary system with sensitive element pitch l is given by the continuous uniform probability distribution

$$\sigma_p = \sqrt{\frac{1}{l}\int_{-\frac{l}{2}}^{\frac{l}{2}} x^2 dx} = \frac{l}{\sqrt{12}} \tag{3-20}$$

where σ_p is in fact the root-mean-square (r.m.s.) value of the distance x between the physical hit and the center of the sensor element. The OMEGA3/LHC1 sensor chip presents a binary pitch of 50 μm in the column direction and 500 μm in the row direction (Figure 3-26 bottom). From Equation 3-20, we get σ_{column} = 14.4 μm and σ_{row} = 144.3 μm. The pixel pitch presents a limit to its efficient sampling. As will be shown in section 5.2 (Position Estimation), the system spatial resolution is obtained by convolution of the pixel pitch resolution with the centroid resolution of the cluster of cells that give a charge signal above a discriminator threshold.

3.6 Readout chip

The role of this chip is to process the signals generated by photoelectrons incident on the silicon anode. In order to reduce noise, the first preamplifier stage of the readout circuit has to be located as close as possible to the detector. The integration of the silicon pixel detector with the readout electronics is done via flip-chip bonding process[9], where small bumps of solder establish the electrical and mechanical connection. The major advantage is that detector and electronics, fabricated in different semiconductor

[9] Solder bump bonding process had been introduced around 1970 by IBM to overcome the limits of wire bonding. The Omega3/LHC1 solder bump has been developed by GEC Marconi Materials Technology Ltd, England.

substrates, can be developed and optimized separately. This type of integration is called hybrid integration (Figure 3-34 left).

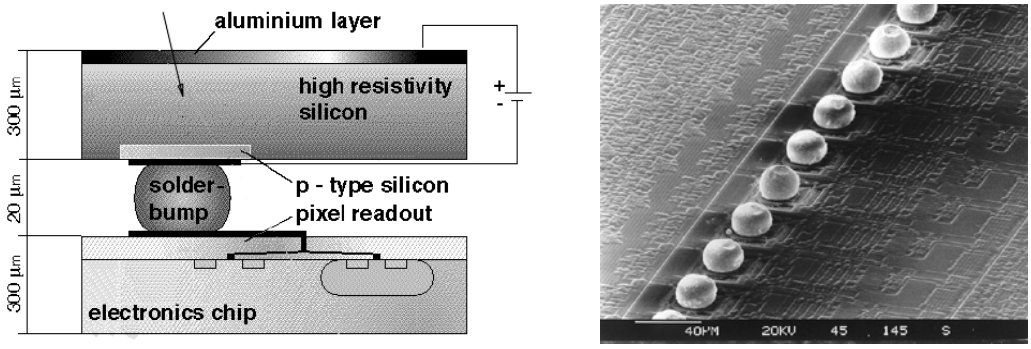

Figure 3-34: (Left) Hybrid pixel detector. (Right) **:** Photograph taken with a scanning electron microscope of a column of solder bumps (ϕ 28 µm) on the readout cell after reflow.

3.6.1 The Omega3/LHC1 readout chip

Also developed in 1995/96 in the framework of the RD-19 Collaboration at CERN for LHC experiments, the Omega3/LHC1 readout chip is a two dimensional matrix of 128 × 16 read-out cells of 50 × 500 µm^2. It means 16 columns and 128 rows to be read-out: 127 active rows, 1 test row and a dummy row for the leakage compensation which is not read. The read-out chip is bump-bonded onto the pixel sensor (Figure 3-34 right), and every sensor cell has its corresponding readout cell. The equivalent noise charge of the read-out chip has been estimated by electrical measurements to be 100 e$^-$ rms without the pixel sensor and 222 e$^-$ rms with the pixel sensor [E. Heijne et al., 1996].

The size of the readout cell is the same as the size of a sensor cell. One readout cell is shown in Figure 3-35. A readout chain contains an analog part and a digital part, as shown in the schematic of Figure 3-36.

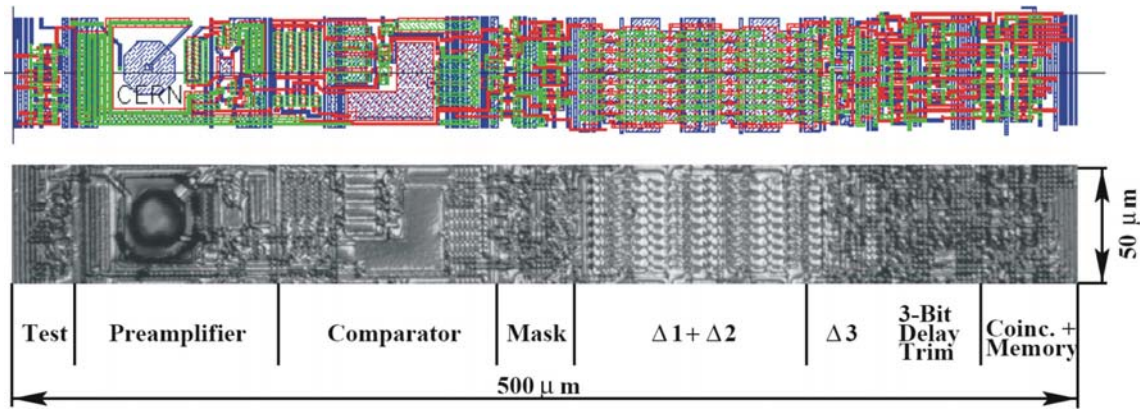

Figure 3-35: Layout and photograph of a single readout cell. The bump pad is the octagon on the left.

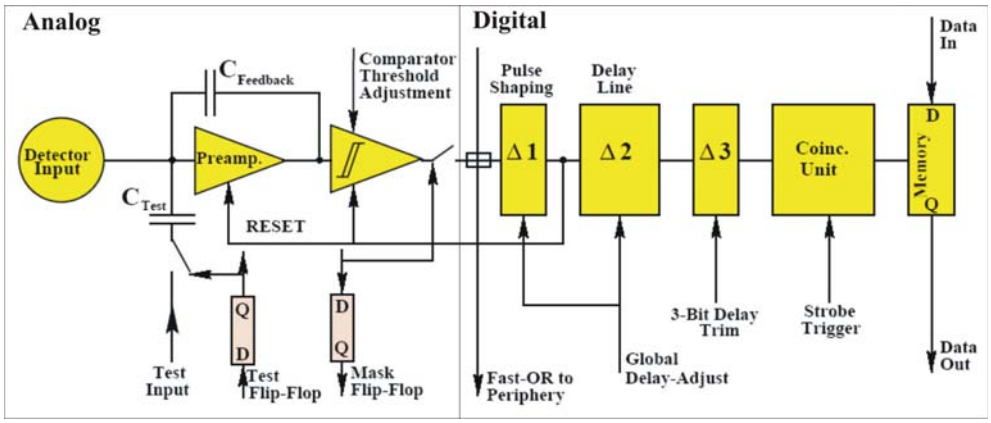

Figure 3-36: Block diagram of the Omega3/LHC1 readout electronics in a single cell.

The analog front-end consists of a charge sensitive preamplifier and an asynchronous comparator for amplification and discrimination. The content of a test flip-flop determines whether a test-input or an analog pulse is applied to the pixel. The amplified signal will then enter the comparator, where it will be compared with a threshold value. The signal rise-time is designed to be 80 ns and the lowest threshold setting is close to 2000 e^-. The comparator can be reset and masked in case of malfunction or excessive noise.

The digital part consists of a delay chain, a coincidence and memory units. Before the comparator output signals enter the delay chain, a fast-OR signal is generated. This signal can be used for diagnostic purposes during testing as any activity in the chip can be detected without a full readout, and it can be used for self-triggering. The delay chain, adjustable between 1.5 and 3.3 μs, allows several hit pulses travelling in the delay line at the same time. This reuqires that the dead-time between consecutive hits on the same pixel is below 250 ns. Following, a three bit delay adjustment allows a fine-tune to the delay of every pixel individually to obtain a more uniform delay across the chip. It can be externally adjusted between 60 ns and 300 ns. Finally, the coincidence logic will write a 1-bit into the data flip-flop memory if during the externally provided strobe (supplied by the experimental trigger) a rising edge at the end of the delay line is detected. The readout cell also presents a leakage current compensation circuit (not shown in the figure) to compensate the detector leakage current.

All these functions of a single pixel cell are carried out by around 400 transistors. The gain of the charge amplifier, the preset threshold for the comparator, the level of the leakage compensation, the global delay and the fine delay adjust, are common to all pixels in the chip, and can be set externally through bias current (I_{bias}, I_{th}, I_{comp}, I_{dl} and

I_{dla}). The required bias voltages and digital signals for the Omega3 chip operation are given in Table 3-6.

General Operational Voltages		
Symbol	*Function*	*Range value*
V_{det}	DC Detector bias voltage	0-100V
V_{DDA}	Analog DC voltage	+3.0V
V_{DD}	Digital DC voltage	+3.0V
GND	Analog ground reference	+1.5V
V_{SS}	Analog and digital common ground	0V
Chip control bias voltages		
Symbol	*Function*	*Range value*
V_{th}	Discriminator threshold bias voltage (DC)	0 – 5000 mV
V_{bias}	Bias voltage for the preamplifier and shaper (DC)	0 – 5000 mV
V_{comp}	Leakage current compensation circuit bias voltage (DC)	0 – 5000 mV
V_{dl}	Global delay line bias voltage (DC)	0 – 5000 mV
V_{dla}	Delay trimming bias voltage (DC)	0 – 5000 mV
V_{ref}	Reference voltage for all the former voltages	
Digital signals		
Symbol	*Function*	*Range value*
S0, S1	Selection of operating mode	TTL level
CS	Chip select	TTL level
LV1	Level 1 trigger for LHC operation	TTL level
R/W	Read/Write (1/0)	TTL level
STR	Strobe signal for data capture	TTL level (~1 μs delay, ~2 μs width)
CLK	Data readout clock for the shift-registers of each column	TTL level (3.5 MHz)
RST	Resets the preamplifier and the comparator of each pixel	TTL level
DT<00:15>	Output data columns	TTL level
Test signal		
Symbol	*Function*	*Range value*
TST	DC test signal applied to the test-input of addressed pixels	0-5 V (~10 μs width)

Table 3-6: Different bias voltages and digital signals required for the Omega3 chip operation.

All the readout chip information mentioned above has been resumed from [T. Jarigsma, 1997; I. Ropotar et al., 2000; W. Snoeys et al., 2001; E. Cantatore et al., 1998; E. Heijne et al., 1996] where more details can be found.

3.6.2 Architecture and operation

There are 5 registers in each column:

Name	Full name	Nº Bits	Connectivity	Function
TST	Test	128	IN→TST→MSK	1 enables Test input
MSK	Mask	128	TST→MSK→ OUT	1 disconnects the discriminator output from the reset of the pixel
DLA	Delay_adj	3×128	IN→DLA→OUT	000 no added delay, to 111 maximum added delay inside each pixel
DT	Data	128	0→ DT→OUT	1 if strobe and delay output levels are equals
FOD	FastOrDelay	16	FOS→ FOD→FOL IN→ FOD→FOL	Digital delay FastOr after being synchronized with the CLK (FOS)

The FOD register is at the bottom of the column. The others are incorporated in the pixel cells. The MSK and TST registers are daisy-chained together. The DLA register is filled by giving 128×3-bit words in series. A connection is provided from the top of the matrix to the bottom so that data can be read in and out. The DT register is connected at the top to V_{ss} so that it fills with 0 after readout. As well as the above registers there is one latch at the bottom of each column:

FOL	FastOrLatch	1	FOD→ FOL→OUT	Latch with coincidence of LV1 and bit 15 of FOD

For example, during data readout, all the 128 data flip-flops of the pixel cells in one column are configured as a shift-register. Then every falling edge of an applied readout clock signal of up to 40 MHz loads the contents of the *n*+1 th row into row *n* and down into the chip peripheral region at the bottom (Figure 3-37), where the data are buffered.

Regarding the operational aspects of the readout chip, the control logic was implemented with four operational modes selected by an external control signal (S0, S1). The modes of operation of the chip are as follows:

S1	S0	Operation	Mode
0	0	Ω operation	0
0	1	LHC operation	1
1	0	Initialise delay registers	2
1	1	Initialize Mask and Test registers	3

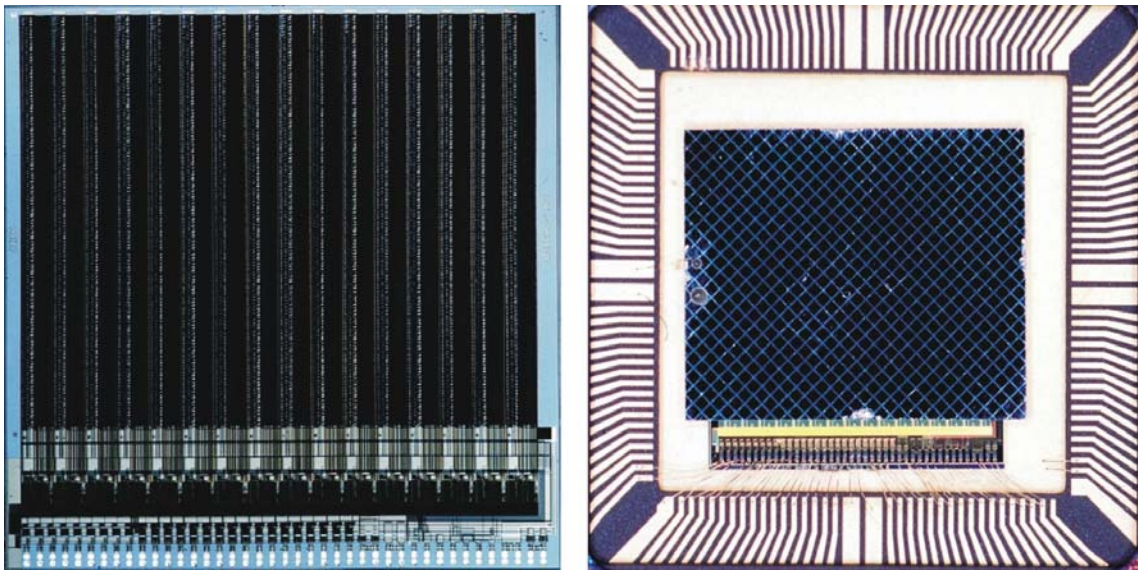

Figure 3-37: (Left) Photograph of an Omega3/LHC1 pixel detector readout chip of size 8.72 × 9.12 mm^2, covering an active area of 8 × 6.35 mm^2 that comprise a matrix of 12 × 16 pixel cells with dimension 50 × 500 μm^2; (Right) Photograph of the silicon detector bump bonded onto the readout chip (ref. CERN-EX-0206005). As referred to in Sub-Chapter 3.4, this assembly is mounted and wire-bonded onto a Pin Grid Array (PGA) ceramic carrier. At the bottom of the chip, where the chip periphery is located, two rows of wire-bonding pads are visible, which provide the connections to the external data and bias lines. Refer to schematics on Figure 3-34 for structural overview.

In mode 0 (Ω Operation), the strobe signal is connected to all pixels during data taking. CS is ignored. LV1 is ignored. After the strobe is given the chip must be selected with CS and either a RST given or readout initiated. To read the data contents of the hit pixel, 128 pulses on CLK with R/W high must be applied after the strobe signal. The RST line resets the data register and discriminators only. If R/W is low CLK is given to the columns which are specified by the 16 bit word at the D inputs. This enables us to verify that data can still be collected while other columns are being clocked. This mode corresponds to the "normal" mode and was applied to all measurements performed in this thesis.

In mode 1 (LHC Operation), the strobe is enabled by the fast-OR signal generated on chip. CLK is pulsed continuously and is gated to the FOD. The Fast Or output of one column is normally gated (CS does not care, R/W high) through a synchronization circuit to the FOD. If CS is low the contents of FOL are presented at the data bus outputs. If, however the R/W is low then data present on the D bus is clocked into the FOD register.

In mode 2 (Initialize Delay_adj register), CS must be low. CLK is connected to the DLA register. R/W should be low and 3×128 pulses of CLK are necessary to clock in a pattern provided on the data bus to fill the register. If R/W is high the content of the

registers is output to the data bus while the register is refilled circularly. The RST is connected only on the DLA register.

In mode 3 (Initialize Mask and Test registers), CS must be low. CLK is connected to the TST and MSK registers. R/W should be low and 2×128 pulses of CLK are necessary to clock in a pattern provided on the data bus to fill the registers. If R/W is high the content of the registers is output to the data bus while the register is refilled circularly. The RST is connected only to the MSK and TST registers.

Mode	S1	S0	CS	R/W	RS	CLK	Action	Description
M0 (OMEGA)	0	0	0	1	1	^	0→DT→OUT	Read-out data registers (both OMEGA and LHC)
	0	0	1	X	1	_	DISC&STR => DT	OMEGA run mode
	0	0	0	0	1	^	IN&CLK^DT, 0 →DT	Clock to DT column selected by IN lines, '0' is clocked in
	0	0	0	X	0	_	0 =>DT, 0 => DISC	Reset DT and discriminators
M1 (LHC)	0	1	1	X	1	^	FOS→FOD, Z→OUT, STR&FOL&DISC=>DT	Clock FOD, Hi Z output (LHC run mode)
	0	1	0	0	1	^	IN→FOD→	Test FastOrDelay shift register (write)
	0	1	0	1	1	_	FOL→OUT	Test FastOrDelay shift register (read FastOrLevel1)
	0	1	0	X	0	_	0=>FOD, 0=FOL	Reset FOD and FOL
M2 (INIT0)	1	0	0	1	1	^	IN→DLA→OUT	Read DLA (cyclic shift)
	1	0	0	0	1	^	IN→DLA	Write DLA
	1	0	0	X	0	_	0=>DLA	Reset DLA
M3 (INIT1)	1	1	0	1	1	^	IN→TST→MSK→OUT	Read TST and MSK chain (cyclic shift)
	1	1	0	0	1	^	IN→TST→MSK	Write TST and MSK chain
	1	1	0	x	0	_	0=>TST, 0=>MSK	Reset TST and MSK

Symbol	Meaning
0	Low logical state
1	High logical state
X	Does not care state
Z	High impedance state
→	Serial input to a structure
=>	Parallel input to a structure
^	Input to the clock of a structure
&	AND
IN	Data lines in input
OUT	Data lines in output

Table 3-7: The Omega3/LHC1 readout chip operation modes.

Through the execution of these logic operation sequences, the output of the data lines will give us the information of the state of each pixel in a 2D distributed matrix. For particle detection application of this multi-channel system using 1-bit binary information, the challenge is time precision. All the hits produced by the same physical event must coincide with the strobe signal by making the cell response as uniform as possible. This is done by tuning each channel internal delay line. A characteristic of the electrical performance of the chip and a calibration, in particular with respect to detector bias, pixel threshold and trigger pulse timing, has been carried out, the results of which are presented in Chapter 6.

3.7 Summary discussion

In this chapter, a full characterisation of the physical parts that constitute the ISPA-tube was presented. Also shown was a detailed study of the gamma ray photon detection processes that undergoes in the collimator, the scintillator, the photocathode, the electrostatic field and finally, in the silicon anode. The method of particle tracking has been performed with a combination of analytical calculations and numerical simulations. For the collimator design efficiency and the interaction between gamma rays and the crystal scintillator, Monte Carlo simulations based on GEANT 3 and GEANT 4 were used. The electric field inside the tube and the silicon anode were simulated with the Maxwell-SV 2D electric field program. In order to obtain a realistic distribution of the charge generated in the silicon anode, the CASINO Monte Carlo simulator was also used.

These are the main properties results:

- The parallel hole rippled-foil tungsten collimator of 26 mm long and 10×9 mm^2 area field of view presents a spatial resolution (FWHM) of 585 μm and 16.5% energy resolution for 122 keV photons energy. The sensitivity detection was measured to be 1.4×10^{-2} at 0.5 cm source distance from the collimator face, where the FOV is 0.5cm diameter at the collimator back face.
- The YAP crystal scintillator of 31 mm diameter, 2 mm thick and aluminium coating, has a peak emission wavelength at 370 nm and features a light yield of around 10000 ph/MeV. The light output at the crystal-photocathode interface integrated over the sensitive area of the silicon detector was estimated at 7

ph/keV. For 122 keV incident photons, the crystal presents a spatial resolution (FWHM) of 320 μm with 17% energy resolution.

- The S20 photocathode quantum efficiency is 23% at 370 nm. An electron conversion efficiency of 1.6 ph/keV is expected.
- The 20 kV electric field inside the tube that accelerates the photoelectrons onto the silicon anode presents a parallel and uniform distribution. Due to emission angle of the photoelectrons at the photocathode surface, some photoelectrons may suffer a maximum deviation of 225 μm at the silicone anode, but with low probability since it's emission angle follows a lambertian distribution.
- For 20 keV photoelectrons that interact on the silicon anode back-plane, 9% will be absorbed at the entrance ohmic layer, 10.5% will be lost by backscattering processes and 80.5% will be absorbed in the sensitive area for charge signal production. The result for a 70 V fully depleted detector gives a most probable signal of 4423 e^-. With an equivalent noise charge of 222 e^-, the signal to noise ratio (S/N) is calculated to be 20.
- The Omega3/LHCI pixel detector readout chip comprises a matrix of 128 × 16 readout cells of 50 μm × 500 μm. Its intrinsic spatial resolution is limited by its pixel pitch that follows a continuous uniform distribution. The quadrature of standard deviations from both column and row directions gives a spatial resolution (sigma) of 145 μm.

After an overview of the architecture of the ISPA-tube underlying its main components, the operation of Omega3/LHCI pixel detector readout chip was presented, followed by a description of the signals and task functions that the readout electronics system must perform to control the chip. An interesting feature of this chip is that electric tests measurements can be done by applying a DC signal to the test-input of addressed pixels. Thus a triggered event firing some pixels can be simulated. This is useful to check the detector response and the correct implementation of the logic in the readout system as well.

References

[B. P. Varma and C. Ghosh, 1973] B. P. Varma and C. Ghosh, **Some optical properties of a multialkali (S20) photocathode and the processing parameters**, J. Phys. D: Appl. Phys., Vol. 6, 1973.

[C. D'Ambrosio et al., 2000] C. D'Ambrosio et al., **Crystalline $YAlO_3$ as a novel window for photodetectors**, Nucl. Instr. Meth. In Phys. Res. A 454, 221-226, 2000.

[C. D'Ambrosio and H. Leutz, 2003] C. D'Ambrosio and H. Leutz, **Hybrid photon detectors**, Nucl. Instr. Meth. In Phys. Res. A 501, 463-498, 2003.

[C. Ortigão, 2003] C. Ortigão, **Simulação Monte Carlo de um Detector SPECT Protótipo de Alta Resolução**, Master Thesis, Instituto Superior Técnico de Lisboa, 2003.

[D. Puertolas et al., 1997] D. Puertolas et al., **An ISPA-Camera for gamma rays with improved energy resolution**, IEEE Trans. Nucl. Sci., vol. 44, 1747-1752, 1997.

[D. Puertolas et al., 1998] D. Puertolas et al., **An ISPA-camera for gamma-rays in nuclear medicine**, Nucl. Phys. B, vol. 61B, 644-649, 1998.

[E. Belau et al., 1983] E. Belau et al., **Charge collection in silicon strip detectors**, Nucl. Instr. Meth. In Phys. Res. A 214, 253-260, 1983

[E. Cantatore et al., 1998] E. Cantatore et al., **Uniformity of response of the LHC1 large area pixel detector system**, Nucl. Instr. Meth. In Phys. Res. A 409, 119-128, 1998.

[E. H. Darlington, 1975] E. H. Darlington, **Backscattering of 10-100 keV electrons from thick targets**, J. Phys. D: Appl. Phys., Vol.8, 1975.

[E. H. Eberhardt, 1968] E. H. Eberhardt, **Source detector spectral matching factors**, Applied Optics IP, vol. 7, Issue 10, p. 2037, 1968.

[E. Heijne et al., 1996] E. Heijne et al., **LHC1 A semiconductor pixel detector readout chip with internal tunable delay providing a binary pattern of selected events**, Nucl. Instr. Meth. In Phys. Res. A 383, 55-63, 1996.

[F. de Notaristefani et al., 1998] F. de Notaristefani et al., **Refractive index and absorption length of YAP:Ce scintillation**, Nucl. Instr. Meth. In Phys. Res. A 406, 479-485, 1998.

[F. De Notaristefani et al., 2002] F. De Notaristefani et al., **A new hybrid photomultiplier tube as detector for scintillating photons**, Nucl. Instr. Meth. In Phys. Res. A 480, 423–430, 2002.

[F. Garibaldi et al., 2004] F. Garibaldi et al., **Novel design of a parallax free Compton enhanced PET**, Nucl. Instr. Meth. In Phys. Res. A 525, 268–274, 2004.

[F. Vittori et al., 1999] F. Vittori et al., **Crystals and light collection in Nuclear Medicine**, Nucl. Phys. B, vol. 78, 616-621, 1999.

[F. Vittori et al., 2000] F. Vittori et al., **A study on light collection of small scintillating crystals**, Nucl. Instr. Meth. In Phys. Res. A 452, 245-251, 2000

[Iztok Ljubljana, 2000] Iztok Ljubljana, **An investigation of silicon pixel tracking detectors and their application in a prototype vertex telescope in the CERN NA50 heavy-ion experiment**, PhD Thesis, Bergische University of Wuppertal**,** WUB-DIS 99-20, 2000.

[I. Ropotar et al., 2000] I. Ropotar et al., **The LHC1 pixel detector studied in a 120 GeV/c pion test beam,** Nucl. Instr. Meth. In Phys. Res. A 439, 536-546, 2000.

[J. A. Mares et al., 2003] J. A. Mares et al., **Scintillation and spectroscopic properties of Ce^{3+}-doped YAP and Lux$(RE^{3+})_{1-x}$AP (RE^{3+} = Y^{3+} and Gd^{3+}) scintillators - [gamma]-ray spectroscopy up to 1 MeV**, Nucl. Instr. Meth. In Phys. Res. A 498, 312-327, 2003.

[John A. Nousek et al., 1999] John A. Nousek et al., **Charge diffusion in CCD X-ray detectors**, Nucl. Instr. Meth. In Phys. Res. A 428, 348-366, 1999.

[J. Varela et al., 2004] J. Varela et al., **Design and evaluation of the Clear-PEM detector for positron emission mammography**, accepted for publication in IEEE Transactions on Nuclear Science (No. TNS-00377-2004.R2), 2004.

[M. Moszynski et al., 1999] M. Moszynski et al., **A high-energy resolution observed from a YAP:Ce scintillator**, Nucl. Instr. Meth. In Phys. Res. A 421, 610-613, 1999.

[N. Belcari et al., 2004] N. Belcari et al., **Detector development for a novel Positron Emission Mammography scanner based on YAP:Ce crystals**, Nucl. Instr. Meth. In Phys. Res. A 525, 258-262, 2004.

[O. Makarova et al., 2004] Olga V. Makarova et al., **Fabrication of collimators for gamma-ray imaging**, Proceedings of SPIE Design and Microfabrication of Novel X-Ray Optics II , CO Volume 5539, 126-132, 2004.

[P. D. Townsend, 2000] P. D. Townsend, **Optical constants for the S20 photocathode, and their application to increase photomultiplier quantum efficiency**, Optics Communications 180, 89-102, 2000.

[R. Pani et al., 1995] R. Pani et al., **Scintillation properties of YAP:Ce**, Nucl. Instr. Meth. In Phys. Res. A 361, 209-215, 1995.

[R. Pani et al., 1997] R. Pani et al., **Scintillating array gamma camera for clinical use**, Nucl. Instr. Meth. In Phys. Res. A 392, 295-298, 1997.

[R. Pani et al., 1994] R. Pani et al., **Multi-crystal YAP:Ce detector system for position sensitive measurements**, Nucl. Instr. Meth. In Phys. Res. A 348, 551-558, 1994.

[R. Holtomt, G. P. Hopkins and P. M. Gundry, 1979] R. Holtomt, G. P. Hopkins and P. M. Gundry, **Surface studies of multialkali antimonide (S20/S25)**, J. Phys. D: Appl. Phys., Vol. 12, 1979.

[S. Agostinelli et al., 2003] S. Agostinelli et al. (GEANT 4 Collaboration), **GEANT 4 – a simulation toolkit**, Nucl. Instr. Meth. In Phys. Res. A 506, 250-303, 2003.

[S. Gianni et al., 2000] S. Gianni et al. (GEANT 3 Collaboration), **GEANT Detector Description and Simulation Tool. European Organization for Nuclear Research**, CERN Program Library Long Writeup W5013, 2000.

[S. Hallensleben, S.W. Harmer, P.D. Townsend, 2000] S. Hallensleben, S.W. Harmer, P.D. Townsend, **Optical constants for the S20 photocathode and their application**, Optics Communications 180, 89-102, 2000.

[S. Rodrigues, 2005] S. Rodrigues, **Multi-crystal YAP:Ce detector system for position sensitive measurements**, Internal note LIP-Algarve, 2005.

[S. W. Harmer and P. D. Townsend, 2003] S. W. Harmer and P. D. Townsend, **Absorption of optical power in an S-20 photocathode**, J. Phys. D: Appl. Phys., Vol. 36, 2003.

[T. Jarigsma, 1997] T. Jarigsma, **Characterisation of the Omega3/LHC1 silicon pixel detector**, Ph.D. Thesis, NIKHEF/97/021, University of Twente, 1997.

[T. Malatesta et al., 1998] T. Malatesta et al., **Energy response and resolution of YAP:Ce matrix for imaging applications in nuclear medicine**, Nucl. Phys. B, vol. 61B, 658-661, 1998.

[V. G. Baryshevsk et al., 1991] V. G. Baryshevsk et al., **$YAlO_3$:Ce-fast-acting scintillators for detection of ionizing radiation**, Nucl. Instr. Meth. In Phys. Res. B 58, 291-293, 1991.

[W. Klamra et al., 1998] W. Klamra et al., **Properties of the YAP:Ce scintillator**, Nucl. Instr. Meth. In Phys. Res. A 404, 157, 1998.

[W. Fisher, 1999] W. Fisher, **Characterization and Analysis of the Dark Pulse Output of Hybrid Photo-diode**, 1999 (unpublished).

[W. Snoeys et al., 2001] W. Snoeys et al., **Pixel readout electronics development for the ALICE pixel vertex and LHCb RICH detector**, Nucl. Instr. Meth. In Phys. Res. A 465, 176-189, 2001.

Chapter 4

Readout Electronics System

A dedicated electronics readout setup was previously designed at CERN by the RD19 Collaboration to meet the specific needs for testing the Omega3/LHC1 silicon pixel detector. The lack of mobility and the space dimension required for the implementation of this setup present one of the major drawbacks for the imaging application proposed in this thesis. To overcome some limitations imposed by this setup and focus all the efforts in order to provide a better portability of the equipment, as for example inside clinical environment, a new readout system was designed. This new system would have to preserve all the logical characteristics of the precedent one, and would need to be able to adapt the existing setup, at least initially, giving us the possibility to do comparative measurements. In this chapter, we present the old readout electronics with the operation procedures that the system conducts. Following, we introduce the new electronic cards with some details on the architectures.

4.1 The old readout system

Figure 4-1 shows a photograph of the laboratory where the existing readout setup is mounted. The need for a dedicated room for such a setup is clearly visible. This setup consists of 5 general parts: the detector (ISPA-tube), the control electronics, the supply voltages, the timing circuits and the data analysis. Mounted on a front-end card, the detector is connected to what is generally called the motherboard, designated also as the RD19/Omega3 digital readout card. This card transfers the supply voltages and the signals (see Table 3-6) to the pixel readout detector, and most of all, executes logic operation sequences (see sub-section 3.6.2) by a Xilinx Field Programmable Gate Array (FPGA). The motherboard is operated and read out by a VME based system which is controlled through a PCI interface by programs running C language. For graphical data analysis, the Physics Analysis Workstation (PAW) software tool is used [René Brun et al., 1989]. The connection between detector, motherboard and VME module is done via

two flat cables comprising twisted pair cables. The chip control bias voltages (V_{th}, V_{bias}, V_{comp}, V_{dl}, V_{dla}) are generated on the VME readout module by a set of five 8-bit DACs, controlled via the VME-processor. The contents of the different chip control registers (test, mask, delay trim) can be writen/read bidirectionally between the VME bus and the pixel readout detector for electrical testing. The readout of the pixel readout detector is controlled locally on the motherboard.

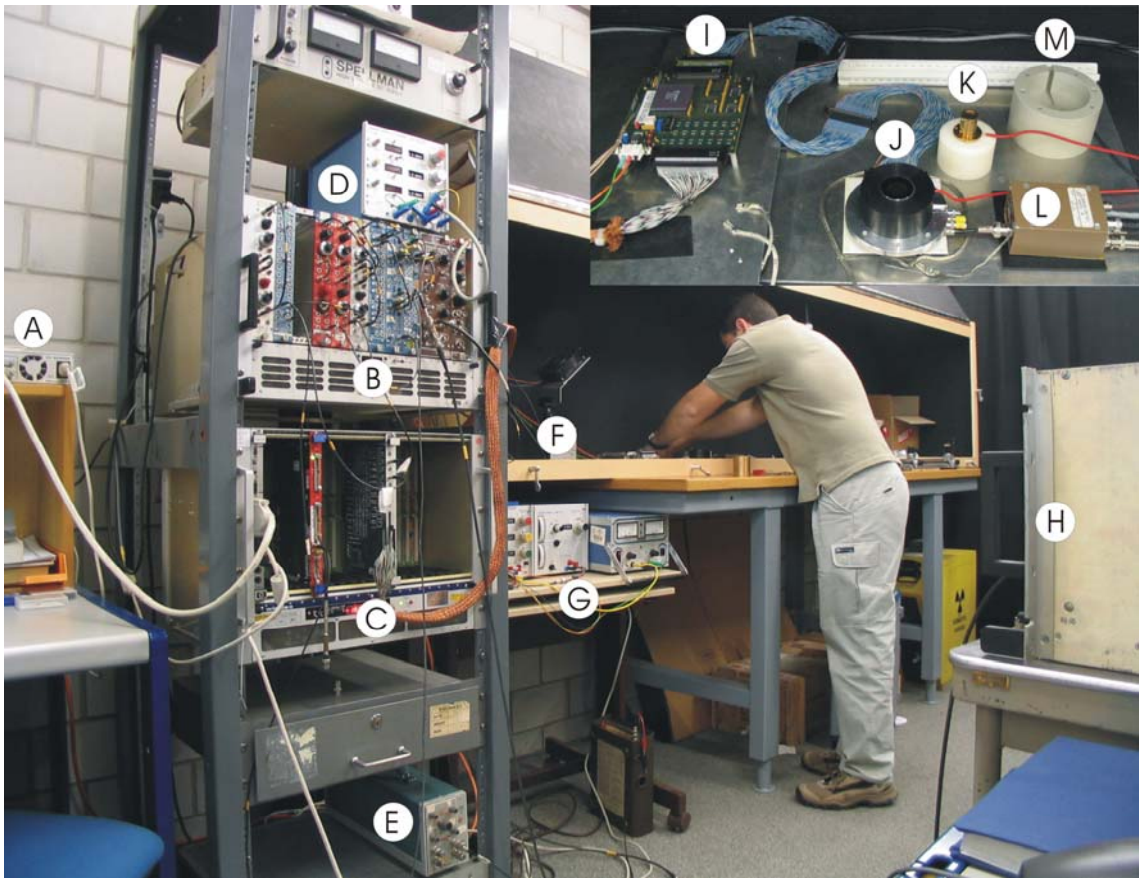

Figure 4-1: Photograph of the existing ISPA-tube imaging setup at CERN. (A) HP workstation; (B) analog NIM modules; (C) VME readout modules; (D) tube high voltage regulated DC power supplies; (E) pulse generator; (F) Cooling fan; (G) tube anode power supply and readout card power voltages; (H) multichannel analyser; (I) RD19/Omega3 readout card; (J) ISPA proximity focusing tube mounted on a test board; (K) tungsten collimator; (L) preamplifier; (M) tube housing.

The readout clock is also generated on the motherboard and is activated only during readout to minimise noise coupling to the pixel cells. The clock frequency is limited to 3.5 MHz by the speed of the programmable logic. When an external strobe is enabled for data capture, 128 clock cycles are applied, shifting the binary contents of the 128 pixels rows out as 128×16-bit words in ~40 μs. The data words are transmitted from the motherboard to the VME readout module, where a zero suppression is performed and a

progressive address for the useful data is produced. The words and addresses are then stored in a FIFO which is accessible via the VME bus for further processing. After each data capture, the VME readout module also generates a trigger signal which is used to time the external strobe.

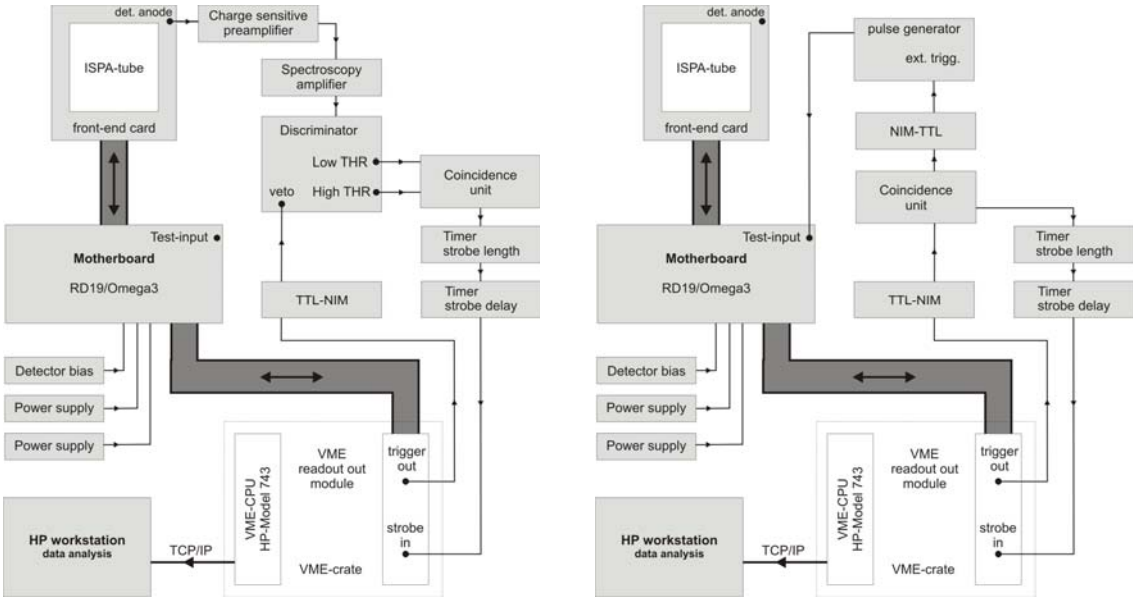

Figure 4-2: Schematics overview of the VME based setup for the Omega3/LHC1 pixel detector operation with radioactive sources (left) and with electrical test-input signals (right). *Not to scale.*

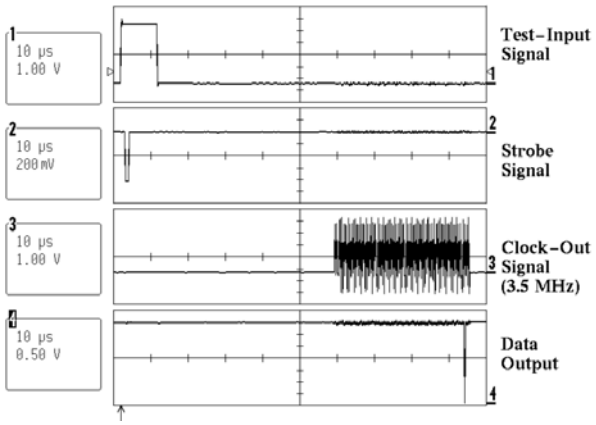

Figure 4-3: Complete Omega3/LHC1 readout sequence of one pixel in a column with the required timing for the signals test and strobe. The strobe signal is a NIM signal of approximately 2 µs, the test pulse has a length of 12 µs and a height of ~5V.

The external strobe signal is obtained via a discrete analog system based on NIM modules. To perform photon imaging measurements with radioactive sources and trigger the pixel readout on good data events, the external strobe is generated by the charge collection signal on the silicon anode. The analog signal is pre-amplified,

amplified and discriminated between high and low levels. The resulting strobe signal is then shaped both in width and delay. Figure 4-2 (left) shows the layout of the setup for the Omega3/LHC1 pixel detector operation with radioactive sources. To perform electrical test measurements, a test signal applied to the test-input of addressed pixels is controlled by a pulse generator which is triggered by the VME readout module. Figure 4-2 (right) shows the layout of the setup for the Omega3/LHC1 pixel detector operation with electrical test-input signals. Figure 4-3 shows an image of a complete Omega3/LHC1 readout sequence from a digital oscilloscope (test signal, strobe, clock and the data output of one pixel in a column).

4.2 The new prototype system

One of the requirements of the new prototype system was to preserve all the logical characteristics of the precedent one and to implement new digital logic functions that substitute the NIM modules for triggering purposes and the VME read out module for data acquisition control. In addition, a new power-line system would also have to be defined. Figure 4-4 shows the layout of the new readout setup.

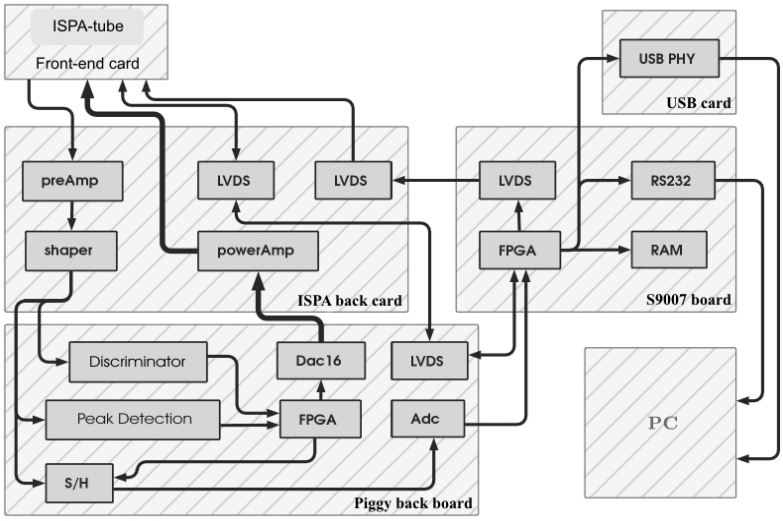

Figure 4-4: Schematic overview of the setup with a block-readout architecture. *Not to scale.*

The system is based on three non-commercial cards plus two dedicated boards, properly designed and programmed to perform a particular operation: the front-end card, the ISPA back card, the Piggy Back Board, the S9007 board and the USB card. The power supply subsystem in these boards delivers the appropriate supply voltages to the

Omega3/LHC1 pixel detector as well as to the internal components in the boards. An external high-voltage power supply (30kV) for the ISPA-tube, plus three external low-voltages power supplies (+5V, +12V and -12V) for the boards are needed, all other values are generated from these external supplies. Each part's function is described below with some details on the architecture.

4.2.1 Front-end card

This card figures a pin grid array (PGA) ZIP socket to plug the ISPA tube (Figure 4-5 left). All the necessary lines for the operation of the Omega3/LHC1 readout chip are accessible through a flat connector. The PGA pin assignment can be found in Appendix. A LEMO connector is used to connect to the detector anode. Initially, a test card with just an Omega3/LHC1 chip glued on it was used (Figure 4-5 right) for the development of the software control and preliminary measurements.

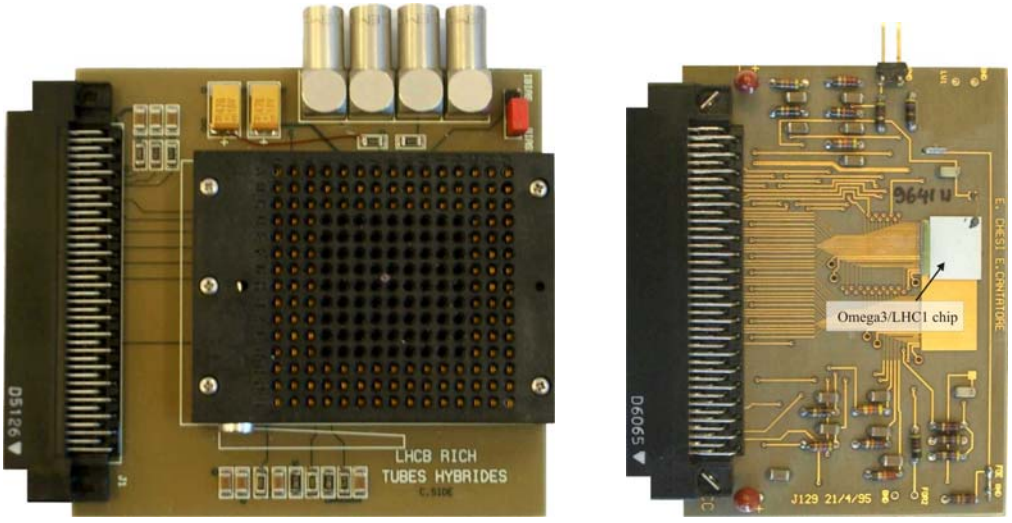

Figure 4-5: (left) ISPA front-end card; (right) Omega3/LHC1 chip test card.

4.2.2 ISPA back card

The ISPA Back card (Figure 4-6) can be considered as a second front-end card that provides at the same time a long communication line to address the chip logic with dedicated LVDS[1] (low-voltage differential signalling technology) drivers and a power amplifier circuit for the Omega3 chip voltage supplies that is able to source up 2 A of

[1] LVDS is a high-speed digital interface that is the solution for many applications that demand low power consumption and high noise immunity for high data rates.

current. It is furthermore equipped with a EURORAD[2] charge-sensitive preamplifier module (model PR304 with sensitivity of 100mV/MeV in silicon) designed for semiconductor detectors, and two INTERSIL [3] semiconductor modules for signal amplification and pulse shaping circuit. In the design stage of this PCB, the capacitances and resistances for the integration/derivation circuits were selected with the aim of obtaining a shaping time of 300 ns. This board operates at input voltages of +12V and -12V.

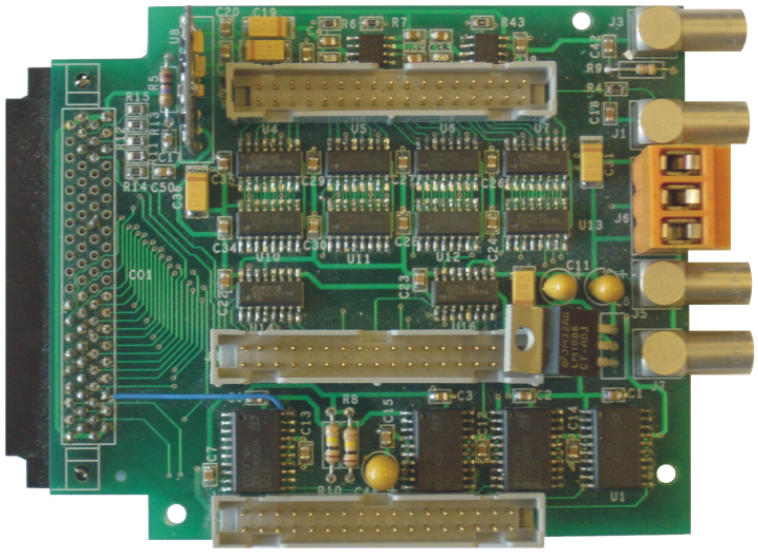

Figure 4-6: Photograph of the ISPA Back Board. The PCB has been commercially purchased and the surface mounted device (SMD) has been achieved at the INFN[4] laboratories of Rome 3, in Italy.

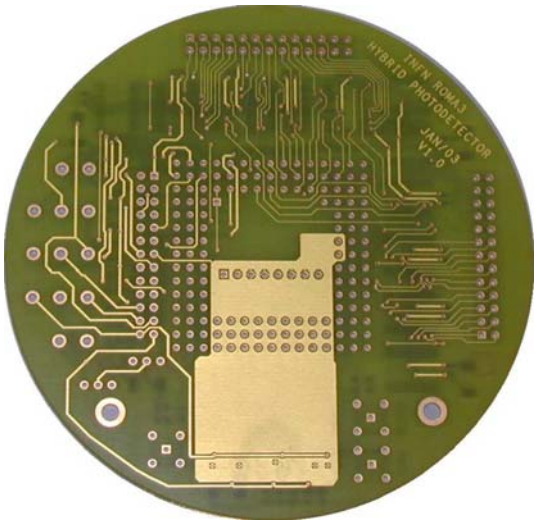

Figure 4-7: Photograph of the PCB for the new ISPA front-end card.

[2] EURORAD; http://www.eurorad.com
[3] INTERSIL; http://www.intersil.com
[4] INFN – Instituto de Física Nucleare Roma-III, I-00146 Rome, Italy; www.roma3.infn.it/

To reduce the introduction of noise sources and preserve a good signal-to-noise ratio, a new card under development at INFN was properly shaped not exceeding the detector dimensions, to plug the tube directly on it with a pin grid array (PGA) ZIP socket. This card will be introduced to substitute the existing front-end card plus the ISPA back board. At the moment only the PCB is available (Figure 4-7). The task functions of this card can be summarised as follows:

- To provide a power amplifier circuit to the chip control bias voltages (V_{th}, V_{bias}, V_{comp}, V_{dl}, V_{dla}) delivered by the DACs in the Piggy Back Board.
- To convert the TTL digital signals into LVDS standards and vice versa.
- To pre-amplify and shape the analog signal coming from the chip anode.

4.2.3 Piggy Back Board

The Piggy Back board (Figure 4-8) was designed in a degree thesis [Manuel Pici, 2001] at the University of the Studies Rome 3 in collaboration with the INFN and the Italian firm CAEN[5]. It manages the entire analog signal front-end for trigger purposes and energy measurements. It is equipped with a peak detection circuit and a low threshold discriminator circuit, whose coincidence is realized by a FPGA (Field Programmable Gate Array) ALTERA[6] EMP7128SQC100. The coincidence signal triggers a sample-and-hold module. The sample-and-hold module acquires the input at the signal port whenever it receives a trigger event at the trigger port. The module then holds the output at the acquired input value until the next triggering event occurs. The signal with a maximum amplitude of 5 volts proceeds to an analog-to-digital converter (ADC). The sample-and-hold module also provides a stable signal to the ADC in order to perform a conversion accurately.

In the design stage of the PCB, the 16-bit precision ADS8320 ADC was chosen since it is a high-speed micro power sampling ADC operating at a sampling rate of 100 kHz. The pulse height converted by the ADC is then sent to the S9007 board FPGA, where it is compared with two digital levels. If the digitized pulse height is found to be inside the region of interest then the S9007 board FPGA iniciates the readout of the 16 rows pixels contents. To access the pixels flip-flop memories for data acquisition, 32 differential lines in technology LVDS allowing high speed communication are available, others 16

[5] CAEN Technologies Inc., Viareggio; http://www.caen.it/
[6] ALTERA Corporation; http://www.altera.com/

bi-directional lines are used for control (strobe, read/write, reset, clock, etc). All the peripherals on the Piggy Back Board share the same data bus, which is directly brought out to the outside. Finally, the Piggy Back Board FPGA also controls 16×8-bit ADCs to supply the chip control bias voltages. This board operates at input voltages of +5V, -5V, +12V and -12V.

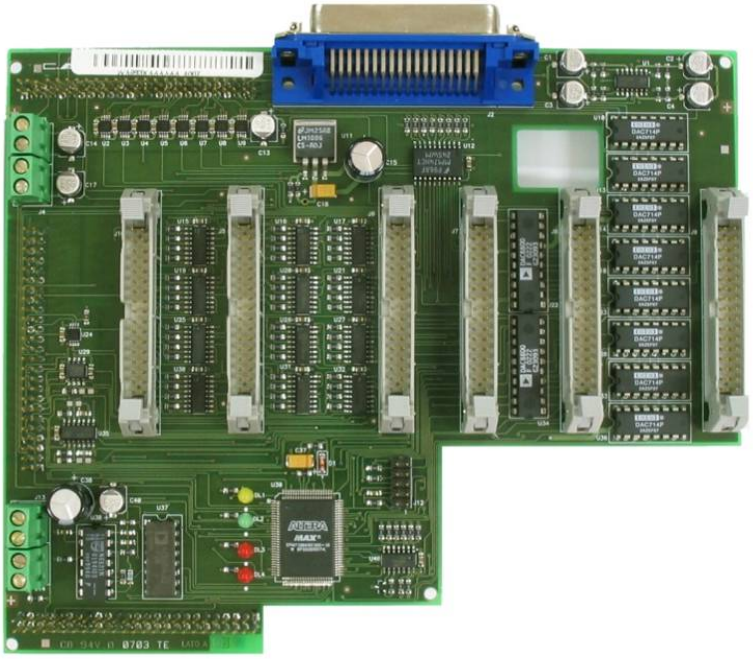

Figure 4-8: Photograph of the Piggy Back Board.

4.2.4 S9007 Board

The S9007 board (Figure 4-9) is the core of the developed system since it controls the entire readout chain and provides the data storage. It was also designed at INFN in collaboration with the firm CAEN and developed as an electronic front-end for the AMS[7] project (CERN experiment to search antimatter in space).

Exploiting its abilities of expansion and programmability, we use it to manage the digital signal that will lead the reconstruction of the gamma emission image detected with the ISPA-tube, which is the most important feature for the medical application of this device. The main element of the S9007 board is the EP20K400 FPGA of the ALTERA APEX family and it has the functionalities of buffer, memory and sequencer. The EP20K400 includes 6400 logic elements that can be used to perform the desired operations. Two clock signals, at 12.5 and 25 MHz respectively, make the state

[7] AMS -The Alpha Magnetic Spectrometer; http://ams.cern.ch/

transition functions. In this dedicated PCB a Digital Signal Processor (DSP), of the family ADSP218x with a peak computing rate of 50 Million Instruction Per Second (MIPS) is also present. This processor, able to perform very complex operations, is not used presently but will be employed in the future to calculate the center-of-gravity of each event that will lead to the reconstruction of the image. This task is actually done on a PC (see Chapter 5). The PCB employs a 576-bit high-speed static RAM that operates in a fully static asynchronous way. This device stores all the data processed by the read-out system. A RS232 serial interface allows sending data to a PC at a maximum baud rate of 115.2 kbps.

Figure 4-9: Photograph of the S9007 Board.

In addition, this card is provided with an auxiliary connector expansion that allows the access to 100 I/O lines of the FPGA. The Piggy Back Board is plugged onto the S9007 board through that connector. This board operates at an input voltage of +5V.

4.2.5 USB card

The USB card (Figure 4-10), although not used presently, has been designed [Enrico D'Abramo, 2004] to be adapted on top of the Piggy Back Board through its auxiliary connector expansion. This card comes as an alternative to the S9007 serial port

communication with the purpose to speed up by 9 times (921.6 kbps) the data rate with a PC. It is based on FTDI[8] single chip FT232BM USB UART IC.

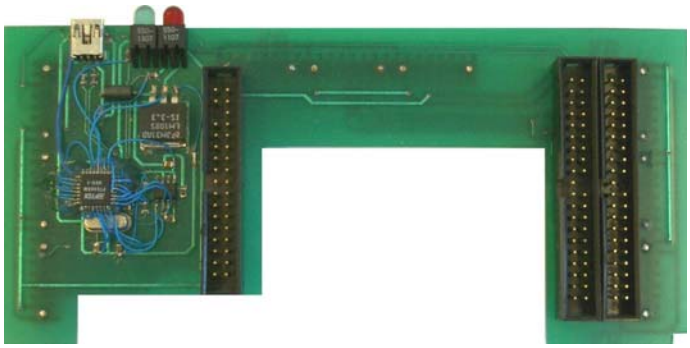

Figure 4-10: Photograph of the USB card.

4.3 Logic programming

In the new readout electronic system, FPGAs can be seen as state machines that link the programmer with all the digital devices present in this system. They are logic devices that provide specific functions, including device-to-device interfacing, signal processing, data communication, data display, timing and control operations, and almost every other function required for this application. The programming of the FPGAs was realised in VHDL (Very high speed integrated circuit Hardware Description Language) using Altera's Quartus II v.4.0 development system compilation software, directly programmed through an EPROM[9] (Electrically Erasable Programmable Read Only Memory) by means of JTAG[10] protocol. The architecture development of the VHDL code has required the expertise available at CERN and mostly at the INFN-Rome 3 [Enrico D'Abramo, 2004].

To test the functionality of the programmed logic components in the FPGAs, the design at multiple stages throughout the design process in Quartus II has been simulated. In fact, the great merit of this software is that it allows the simulation and the synthesis of real devices without physically being linked and thus, allowing to detect defects before the unit is programmed. After the FPGAs programming is complete, signal probing measurements were done with a logic analyzer. Logic analyzers are used to

[8] FTDI- Future Technologie Devices International Ltd.; http://www.ftdichip.com/
[9] Memory chip that retains its data when its power supply is switched off.
[10] JTAG, an acronym for Joint Test Action Group, is the usual name used for the IEEE 1149.1 standard entitled Standard Test Access Port and Boundary.

capture data into timing diagrams in systems that have many channels. Logic analyzers can uncover hardware defects that are not found in simulation. Once the probes are connected (see Figure 4-11), the analyzer is programmed with the names of each signal. Next, the capture mode is chosen, where the clock signal is defined, and data is taken on the falling edges of the clock. Figure 4-12 shows a timing diagram of the data captured during a readout of the pixels mask and test flip-flop memories.

Figure 4-11: Photograph of the Omega3/LHC1 chip test card (see figure 4.5) connected with the logic analyzer probes.

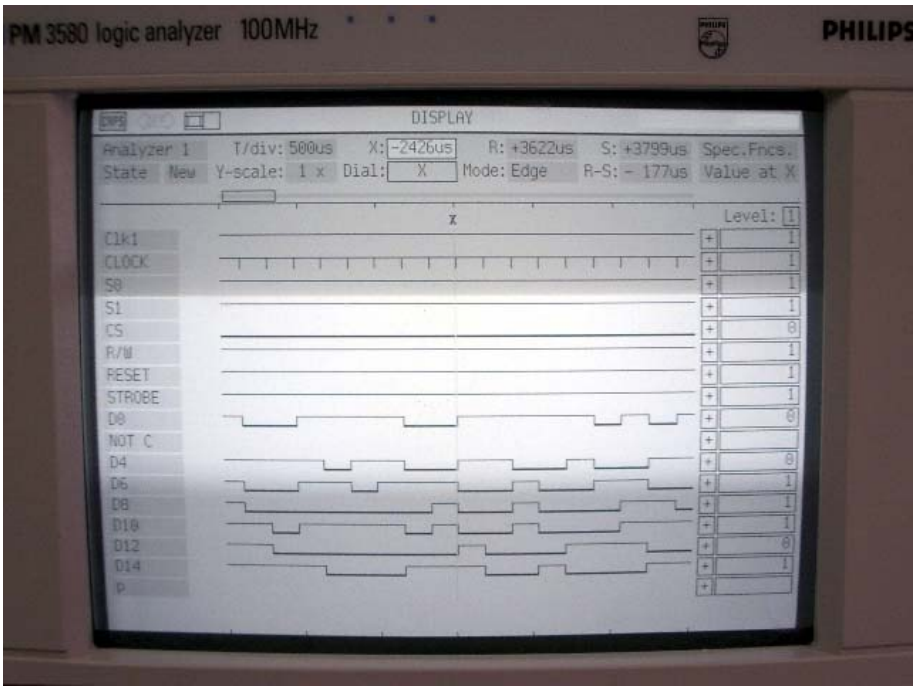

Figure 4-12: View of the logic analyser's display (Philips PM3580) during a chip readout of the mask and test flip-flop memories (operation mode 3). The left column shows the designation of the probes connected on the Omega3/LHC1 chip test card (refer to Tables 3.6 and 3.7) and the right column shows the corresponding level state at the X vertical line. Only even data lines (D0:D16) are probed.

4.4 Summary discussion

The new readout system use custom electronic boards designed toward optimization of a full working laboratory setup and ease of integration with the ISPA-tube. The system accomplishes several tasks by using two different FPGAs configurations. For data transfer between boards, all signals use the LVDS standards. Concerning their operations, VHDL simulations and signal probing with a logic analyzer have demonstrated the correct operation of the logic functions that control the detector. Electrical measurements with the test input of the readout electronics chip could also be performed. The analog circuit has also been tested with the anode signal of the ISPA-tube by acquiring a radioactive source spectrum with a multichannel analyzer (MCA) built around the FPGA of the Piggy back board. However, we did not succeed in making position measurements with the ISPA tube using radioactive sources. As a result, we pointed out two problems. The first is related to digital and analog grounds, especially evident in the ADC circuit where digital return (ground) currents find their way into the ISPA back board analog circuit. The solution engages a redesign of this board keeping the analog and digital grounds separated. A second problem, not yet totally understood but still related to noise, is the effect of crosstalk into the clock signal. The noise couples onto the clock signal and introduces errors on the data acquisition synchronization. This effect still remains when the analog circuit line for triggering purposes on both ISPA back card and Piggy back board is replaced by the analog line from NIM modules. This observation suggests that the noise source is associated with the analog signal.

Meanwhile, and despite of these present limitations of the new prototype system, the control and readout software has been developed and used successfully for measuring and characterising the Omega3/LHC1 silicon pixel detector. Details are presented hereafter.

4.5 References

[Enrico D'Abramo, 2004] Enrico D'Abramo, **Sistema di imaging medico sensibile ai raggi gamma,** Degree Thesis, Electronic Engineering Department, Università degli Studi di Roma Tre, Italy, 2004.

[Manuel Pici, 2001] Manuel Pici, **Sistema per l'estrazione del sincronismo per matrici di rivelatori γ**, Degree Thesis, Electronic Engineering Department, Università degli Studi di Roma Tre, Italy, 2001.

[René Brun et al., 1989] René Brun et al., **PAW: a general-purpose portable software tool for data analysis and presentation**, Computer Physics Communications, Volume 57, Issues 1-3, 432-437, 1989.

Chapter 5

Application Software

For a convenient use of the ISPA-tube, the system has not only to be very compact but also must be very simple in its direct control and use. These requirements have led to the development of a code designed in order to perform any operation by a mouse click in a complete interface framework. This code, that we developed in Microsoft Visual Basic version 6.0 and running under Windows XP, is described in this section. The method used for the image reconstruction is also presented.

5.1 The visual basic interface program

Figure 5-1 shows the diagram of the software architecture developed to access the S9007 electronic board and therefore control the acquisition process of the ISPA-tube.

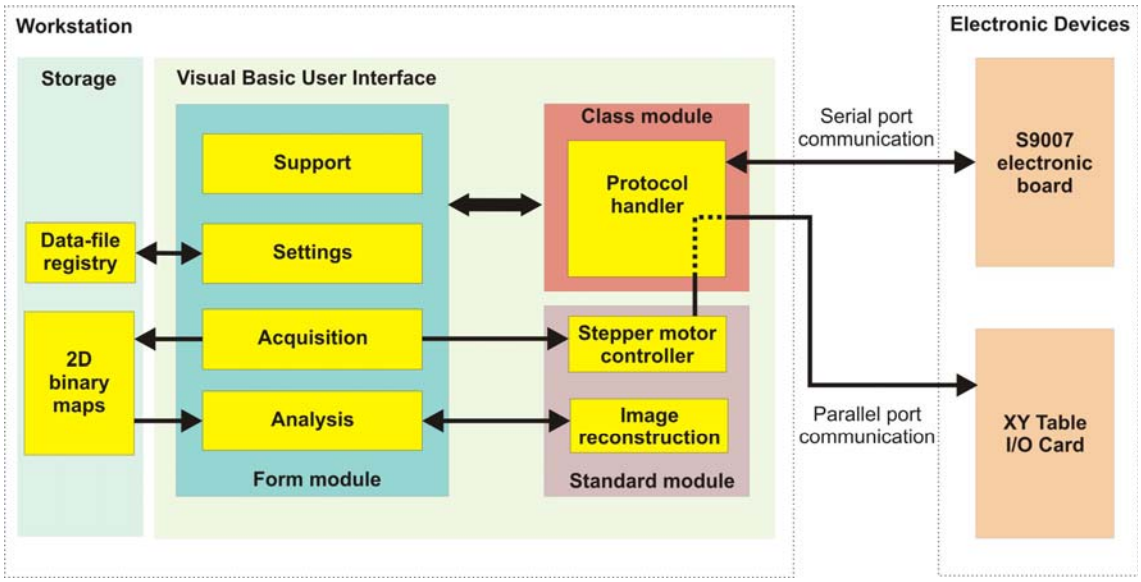

Figure 5-1 Diagram of the application software for the ISPA-tube prototype system.

The software consists of modules written in Visual Basic. Three types of modules are being used: form module, standard module and class module. The form module contains the graphic elements of the VB application along with the instructions and the

declarations. The standard module contains general-purpose instructions and procedures not pertaining to anything graphic on-screen. The class module contains the defining characteristics of an object, including its properties and methods.

5.1.1 The protocol handler

A protocol handler provides scripting language components for communicating with external devices through serial port communication. It is considered the core of the system architecture since it contains all the functions that address the FPGA S9007 electronic board for the operation of the ISPA-tube. The protocol handler is implemented in a class module transmitting and receiving data as specified by the serial port interface protocol. The visual basic public functions provided by this class module are fairly self explanatory:

- Init: Initialize Serial Communication with the board on a specified port;
- send_Reset: Send a reset signal to the board;
- send_Read: Request a reading with a specified length at a specified hexadecimal address and outputs the variable array DataToSend;
- send_Write: write a data array at a specified hexadecimal address;
- OnComm: decode the data from the serial line and outputs it into the variable array DataArrived;

The data format sent through the serial connection is represented in Figure 5-2. It is composed by an initial byte that points out the type of command, followed by an optional 3 bytes address, and by data of 768 bytes maximum size.

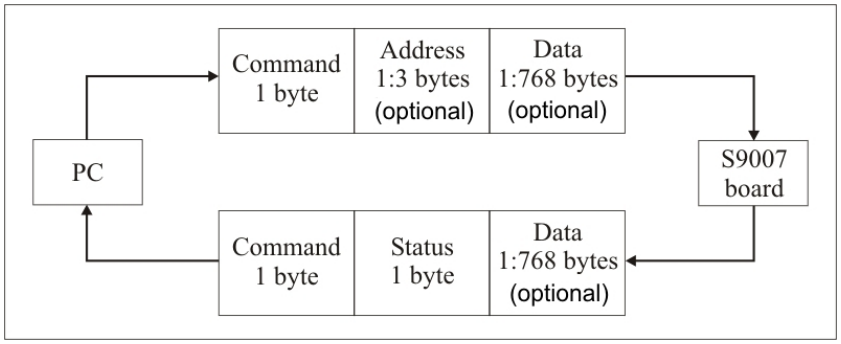

Figure 5-2: Serial data packet format.

The type of command assumes three values:

- Reset = 00h;
- Read = 01h;
- Write = 02h;

The address corresponds to a specified register implemented in the source code of the FPGA. These registers currently implemented are described in the Table 5-1. For example, a write to register address 0×40020 (delay map register) will send a package of 768 bytes (16×128×3 bits) whose entries are either 0 or 1.

Register	Address (hexadecimal)	Access	Bytes
Delay Map	0×40020	R/W	768
Test and Mask maps	0×401A1	R/W	512
Hit map	0×402A2	R	256
Status	0×40322	R/W	1
Strobe delay length	0×40323	W	1
Strobe delay width	0×40324	W	1
V_{LowTh}	0×40000	W	1
V_{comp}	0×40001	W	1
V_{th}	0×40002	W	1
V_{dla}	0×40003	W	1
V_{dl}	0×40004	W	1
V_{bias}	0×40007	W	1

Table 5-1: Basic register file addresses implemented in the VHDL code.

The data format received always contemplates two bytes, followed eventually by data of 768 bytes maximum size. The first byte is always the echo of the sent command to check the serial communication. The second byte indicates the status state of the command and can assume three values:

- Status = 00h: the command has been executed correctly;
- Status = 01h: a time out occurred after command request;
- Status = 02h: unknown command;

Regarding the form module, a main graphical interface contains four panels: settings, acquisition, analysis and support. Simply running an executable file, the user will have

first access to this main form. Next, the software executes automatically a search at the computer ports to detect where the S9007 electronic board is attached. From now on the user can have access to all panels and view the current state action displayed in the status bar located at the bottom of the program window. An overview of each panel follows.

5.1.2 The settings panel

In the *settings* panel (Figure 5-3), all the chip control bias voltages referred to previously can be set manually by entering the values on the corresponding fields or automatically in some cases. Automatically means that the system will start a tuning process of selected parameters to reach the maximum efficiency detection, i.e. the maximum number of firing pixels. The voltage scan range and the step size can be set and this calibration can be performed using the read out electronics with the detector input, or alone using the test input. The behaviour of the efficiency versus bias scan is displayed on a graph.

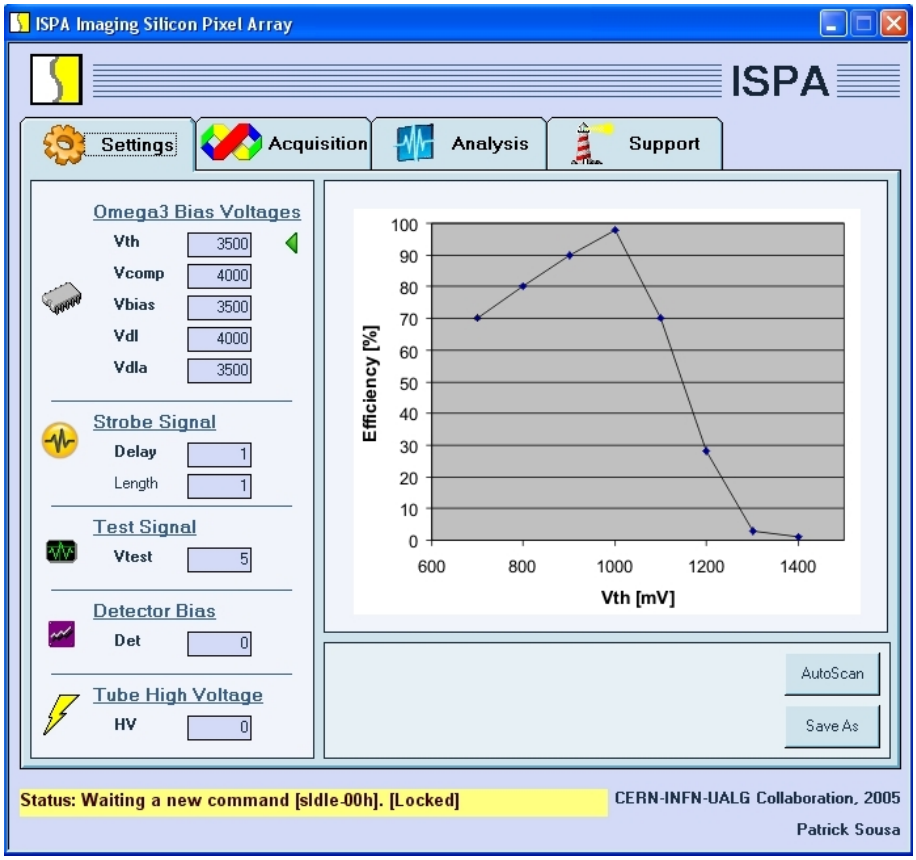

Figure 5-3 Screenshot of the settings option menu. The chart shows an automatic scan of the efficiency detection versus the threshold voltage. All the chip control bias voltages can be tuned stably and effectively in the same way.

Default values of the calibration parameters for standard detector imaging application are automatically loaded if not changed, i.e., any altered configuration parameter is written in a data-file registry so that it is automatically loaded on the next startup.

5.1.3 The data acquisition panel

The *data acquisition* panel (Figure 5-4) provides the following tasks: Energy histogram, 2D hit map, make/load a mask and loop on rate.

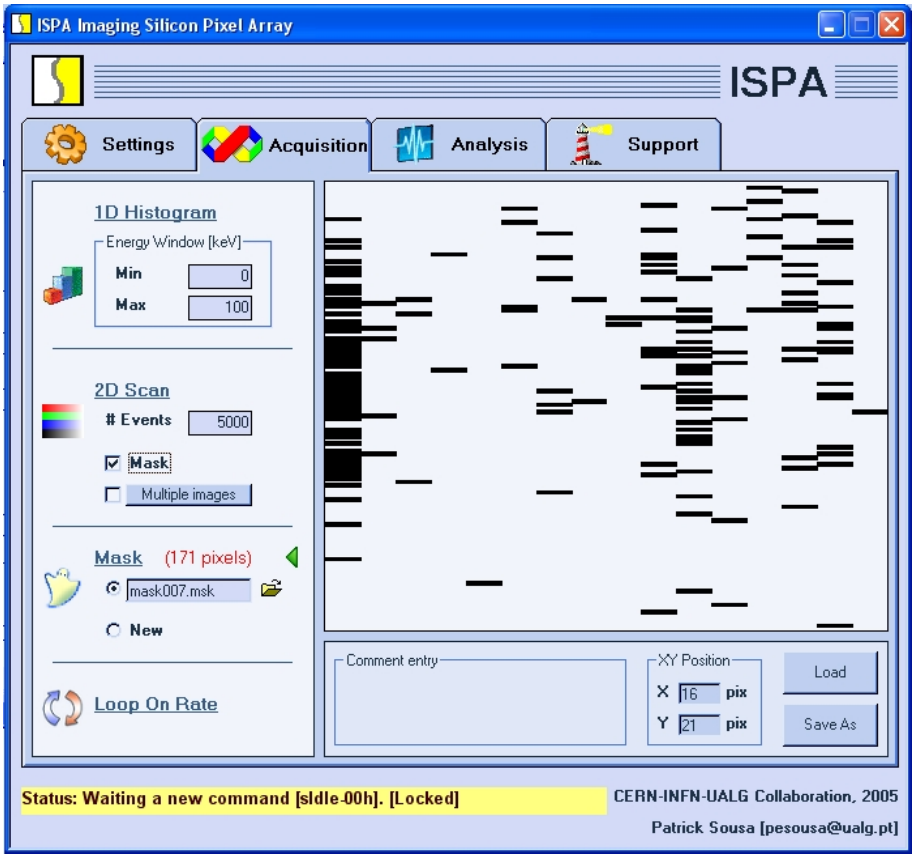

Figure 5-4: Screenshot of the data acquisition option menu. The chart shows bad pixels that are masked.

For the 1D histogram, an energy spectrum of the radioactive element present in the study can be acquired, allowing the user to set an energy window (min, max). Values are expressed in keV. To make a 2D scan, three data entries must be supplied: with/no mask, maximum number of events and multiple images. The multiple images option calls a general module (stepper motor controller – see Figure 5.1) that sets the parameters of a XY positioning for wide area scanning. The final image is a set of

reconstructed mosaic images and is discussed later in subsection 5.3 (wide area scanning system). The 2D scan takes into account the total energy window of the 1D histogram, i.e. the lower and upper limits which define the total energy window outside of which events will be rejected. A mask map operation is also available. This operation makes recognition of unwanted or noisy pixels that can be tagged and excluded for analysis purposes. The loop on rate function checks the efficiency detection (number of firing pixels) of the present application for the selected calibration parameters. The values of the efficiency are written on the event log window at a self-triggered rate. It can be performed using the read out electronics with the detector input, or alone using the test input.

5.1.4 The data analysis panel

The *data analysis* panel (Figure 5-5) provides the tools to make analysis and reconstruct the gamma image from loaded 2D binary maps. Analysis parameters such as the number of single photon events and the min/max hit pixels per event can be set.

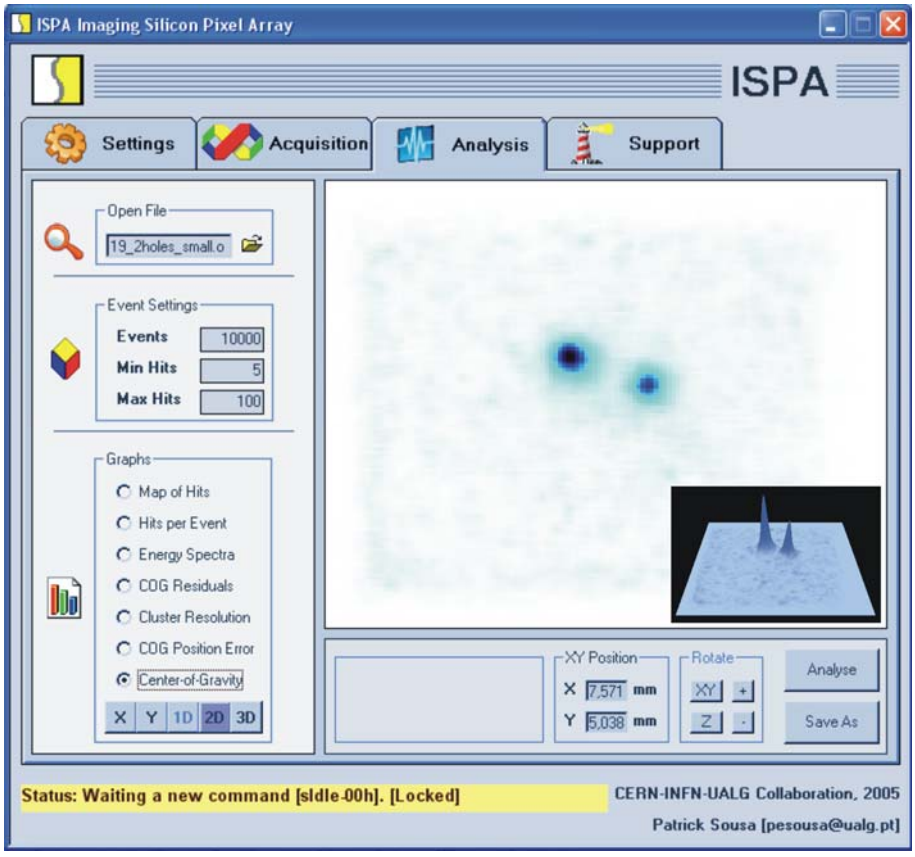

Figure 5-5: Screenshot of the data analysis option menu. The 2D/3D contour maps shows the reconstructed image obtained by processing the centre of gravities of 10000 events. Each event corresponds to a 2D binary map of hit pixels.

The numerical analysis application allows the visualization of various graphs, e.g. map of hits, hits per event, energy spectra, centre of gravity residuals, cluster resolution, centre of gravity position error, and centre of gravity. Some types of graph allow the user to sort X, Y, 2D or 3D plots. Images can be saved in a JPEG format or in a data file. This form module calls a standard module with all the procedures for the image reconstruction (see Figure 5.1). The step method necessary to estimate the XY position of the incoming photon from a 2D binary map is explained in section 5.2.

5.1.5 The support panel

The *support* panel provides a more technical interface with four panel options (main, maps, voltages and images) and a command utility (reset, read and write) to access directly the register file addresses. This panel was first developed to test the source code implemented in the FPGA with an easy way to understand communication and operation problems. It is divided in four subpanels: main, maps, voltages and images.

In the *main* panel (Figure 5-6), the number of packages sent or received is visible with a communication speed display of the input/output transmission. It is useful in that way to check and confirm the package transmission.

The *maps* panel (Figure 5-7) provides an access to the register file addresses of the fine delay map adjustment, the test input flip-flops map adjustment and the mask flip-flops map adjustment. In this panel, a full display of the pixel matrix of the chip (2048 pixels) allows to set each pixel value individually by the simple click of the mouse.

The *voltages* panel (Figure 5-8) provides progress bars to set manually the chip control bias voltages.

In the *images* panel (Figure 5-9), the strobe signal delay length and width can be set. And finally, for efficiency tuning adjustment, the 2D hit map of the firing pixels can be downloaded and visualized. An option sets the number of consecutive maps to acquire.

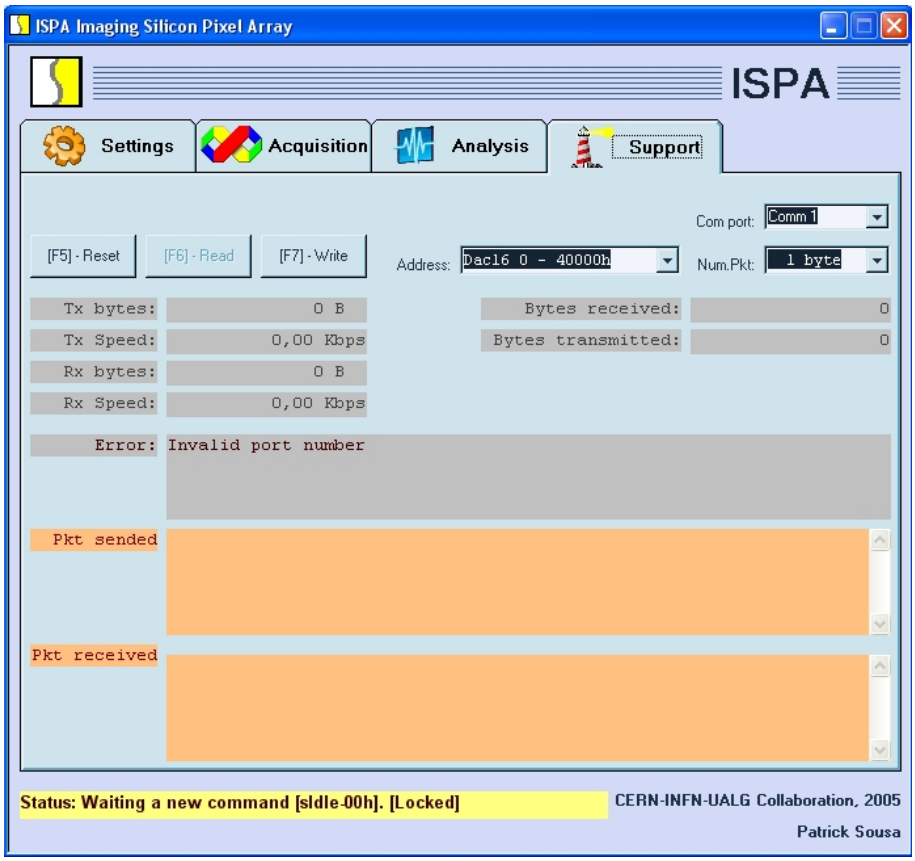

Figure 5-6: Screenshot of the support's *main* panel.

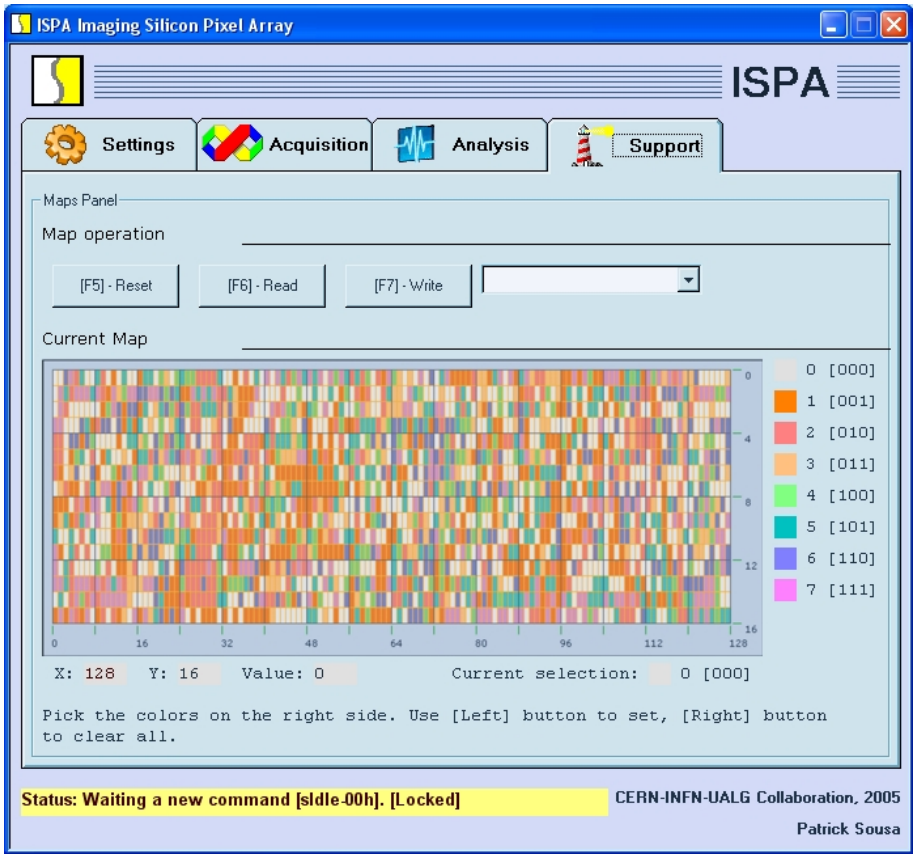

Figure 5-7: Screenshot of the support's *maps* panel.

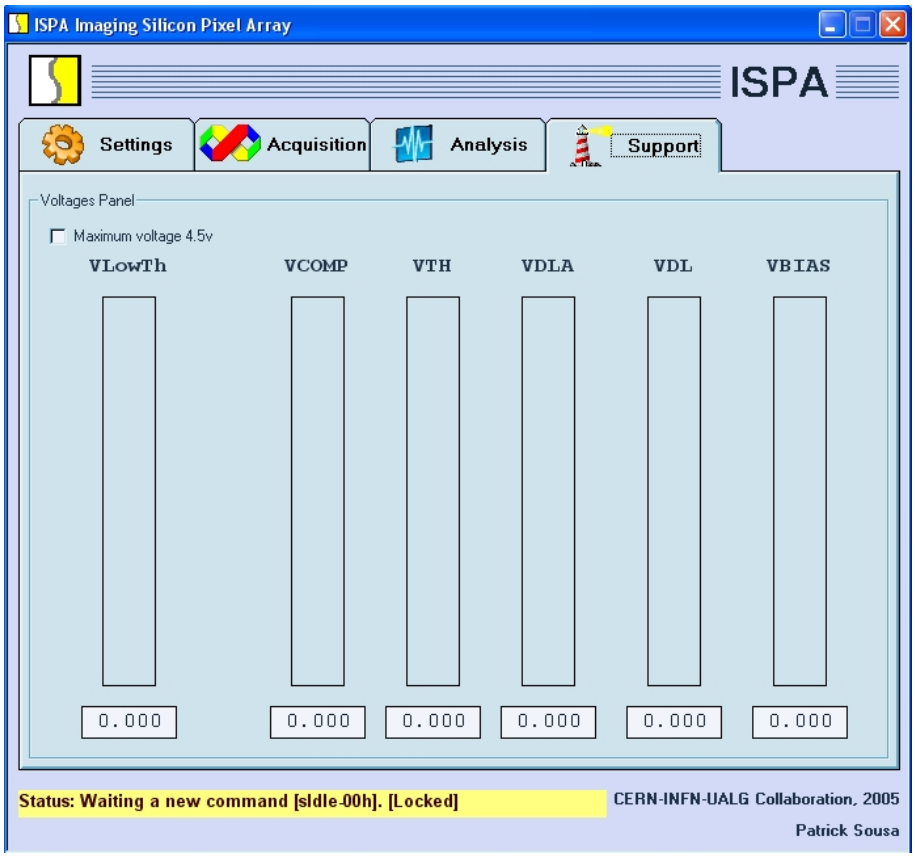

Figure 5-8: Screenshot of the support's *voltages* panel.

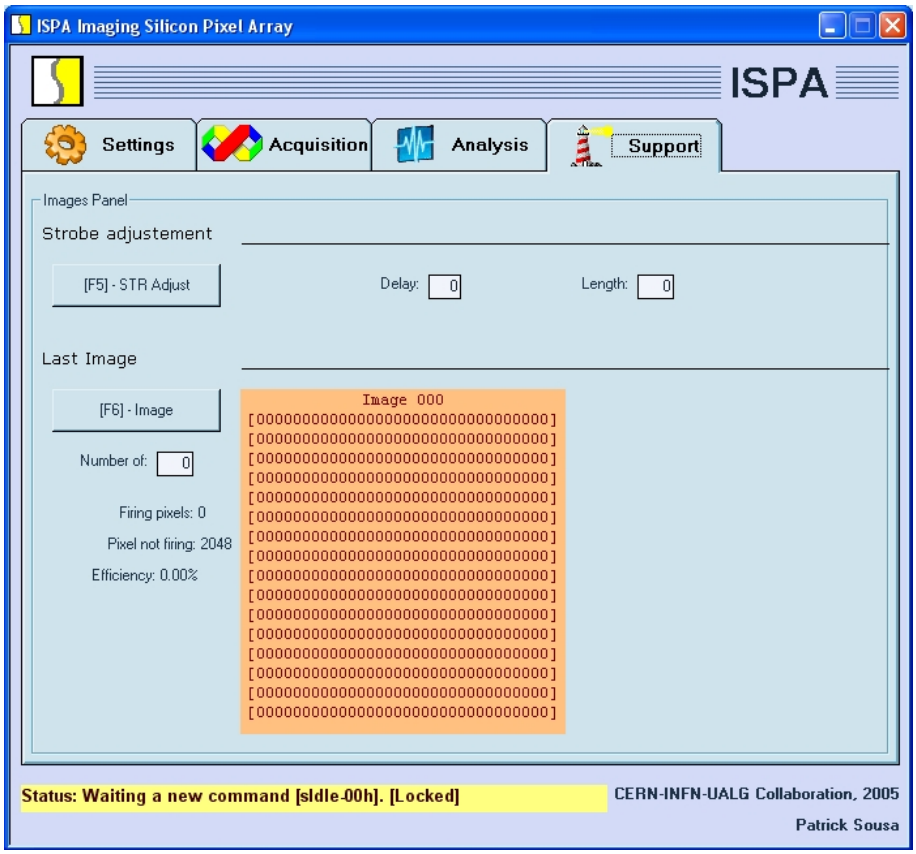

Figure 5-9: Screenshot of the support's *images* panel.

5.2 Position estimation and image reconstruction

The ISPA-tube uses the single photon counting technique to determine the spatial distribution of a radioactive isotope that has been, for example, administered to a patient. Each individual photon hitting the camera is directly sampled by making physical measurements on the detector system. This direct sampling follows a probability distribution because it results from several stochastic processes starting with the conversion of the gamma ray energy into scintillation photons at the scintillator stage, until the generation of position signals within the 2D silicon anode. For example, if we consider a perfect object point, the image of this object will consist of a spot of several pixels, with a maximum probability density in the center that decreases away from it. This image function is characterized by a point spread function (PSF) and the two-dimensional image reconstruction will then consist in a collection of XY coordinate maps of possible position estimates of the incoming photons.

In this application we assume the point spread function can be approximated by a Gaussian spatial distribution. The choice of this conventional method of reconstruction for binary maps depends significantly on linear position signals across the system. For example, a non-uniformity of the electric field within the tube would result in variations in signal amplification at different locations of the silicon anode. Another example on the ISPA-tube design, described previously in section 3.2 (Crystal Scintillator), has demonstrated that the scintillator exhibits good linearity up to the boundary of the edge region, and consequently its diameter must be larger than the field of view of the detector. The behaviour of the ISPA-tube present good linearity results allowing the correct application of this analytic reconstruction method.

A demonstration of the reconstruction process with the mathematics applied in the image reconstruction follows.

During a data acquisition, for each detected event, the deposition energy is registered and, after a real-time energy discrimination to select good events, the corresponding binary (pixel) matrix is stored as a discrete two-dimensional image. At this stage, most of the firing pixels carry relevant information free from scattered and background effects, but one must account for the *noisy* pixels. With time, some pixels of a detector

may become out of order and start to produce outputs not triggered by an incoming photon, i.e. to become noisy.

The first step then is to remove noisy pixels. Part of this process is simply done by eliminating the particular pixels whose count rate is too high relatively to the system count rate (Figure 5-10a).

The other part of the process is to identify those whose count rate is acceptable but are not correlated with its neighbours at the single event level. This is done by selecting a cluster of firing pixels and by calculating the mean and the standard deviation of the region. We then compare the position of each firing pixel with the mean of the selected cluster. If their absolute difference is larger than some threshold, we tag the pixel as defective (Figure 5-10b). This process is repeated for all pixels. The threshold is set to a number between two and three times the standard deviation of the group of pixels.

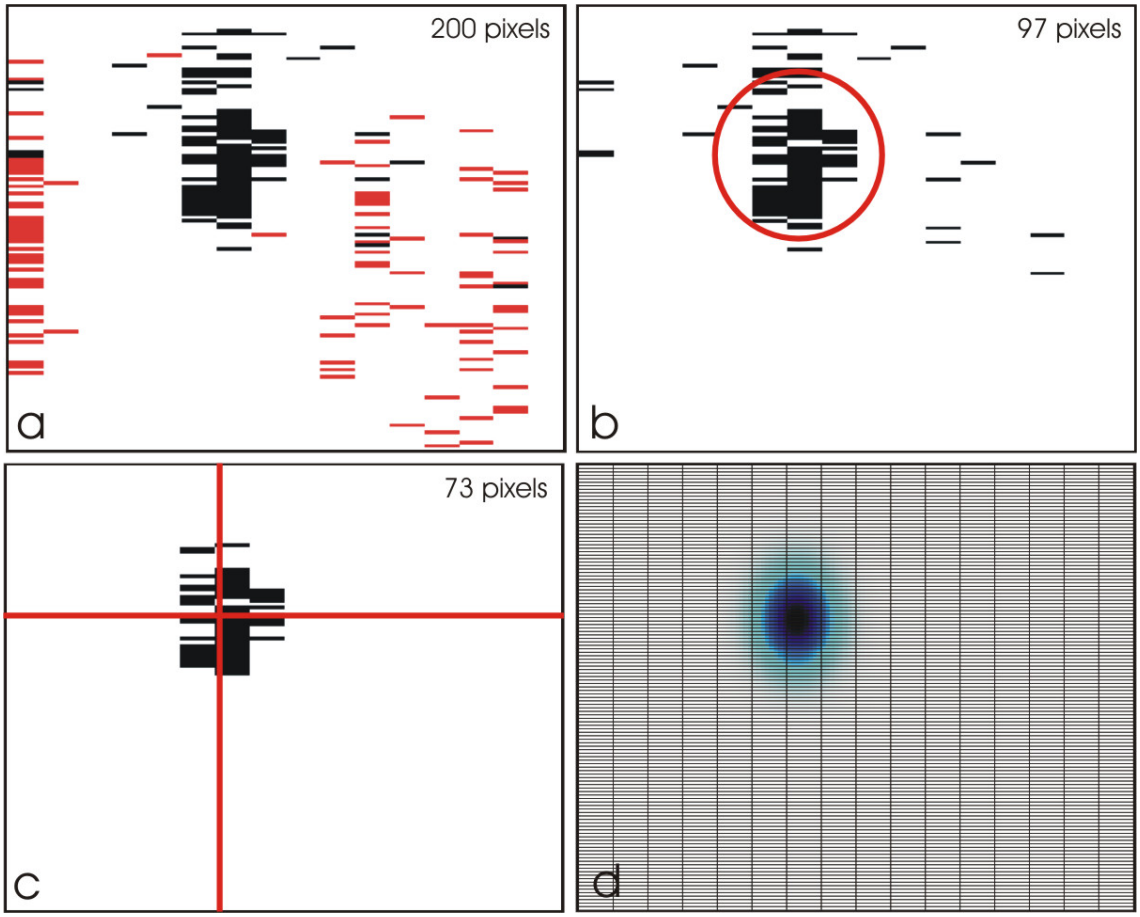

Figure 5-10: (a) Raw image obtained from one single photon event in the ISPA tube (16 x 128 pixels). A total of 200 hits are registered, where 103 pixels (red colour) are tagged noisy; (b) Raw image obtained after removing noisy pixels. A total of 97 hits is registered, where 24 pixels are considered isolated; (c) Centre of gravity position of the 73 remaining pixels; (d) Distribution of the variance of the hit pixels around the centre of gravity, assuming a Gaussian probability density distribution of 99.7% ($\pm 3\sigma_{X,Y}$).

Free from noisy and isolated hits, we can now proceed by calculating the centre of gravity $COG_{X,Y}$ for the remaining pixels (Figure 5-10c) and compute the sample standard deviation $S_{X,Y}$ defined by:

$$COG_{X,Y} = \frac{\sum_i (X_i, Y_i)}{N} \tag{5-1}$$

$$S_{X,Y} = \sqrt{\frac{\sum_i \left((X_i, Y_i) - COG_{X,Y}\right)^2}{N-1}} \tag{5-2}$$

where N is the total number of firing pixels.

The sample standard deviation is a measure of variation and is based on the squared deviation of the firing pixel positions around the centre of gravity. For a binary detection system, the position estimation deviation must be combined with the spatial precision given by the pitch of the detection element l divided by $\sqrt{12}$. The standard deviation is therefore defined by

$$\sigma_{X,Y} = \sqrt{S_{X,Y}^2 + \sigma_{Pitch_{X,Y}}^2} \tag{5-3}$$

The distribution of the variance of the hit pixels around the centre of gravity, assuming a Gaussian probability density distribution is illustrated in Figure 5-10d.

Now that we know how much variation was found around this particular estimate of the mean, what we need to know is how good is our estimate of the centre of gravity. We finally do this by calculating the standard error of the centroid

$$\sigma_{COG_{X,Y}} = \frac{\sigma_{X,Y}}{\sqrt{N}} \tag{5-4}$$

And finally, for image processing, we compute a Gaussian distribution (Figure 5-11) for the position estimation around the centroid COG with standard error $\sigma_{COG_{X,Y}}$

$$f(X,Y) = \frac{1}{\sigma_{COG_X} \cdot \sigma_{COG_Y}} e^{-\frac{1}{2}\frac{(X-COG_X)^2}{\sigma_{COG_X}^2}} e^{-\frac{1}{2}\frac{(Y-COG_Y)^2}{\sigma_{COG_Y}^2}} \tag{5-5}$$

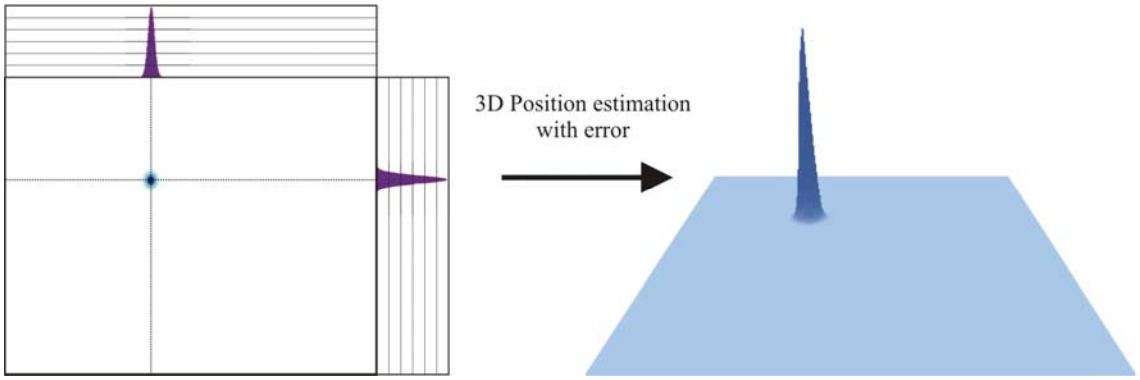

Figure 5-11: Position estimation of a single photon event convolved with a Gaussian point spread function. Projections along X and Y axes are also shown.

As mentioned above, the final image is a result of the combination of successive single-photon position events, i.e. a collection of processed XY maps of hits. This complete analysis is done in the image reconstruction module of the Visual basic program (see Figure 5.1). The basic steps identified in the fluxogram are presented in Figure 5-12.

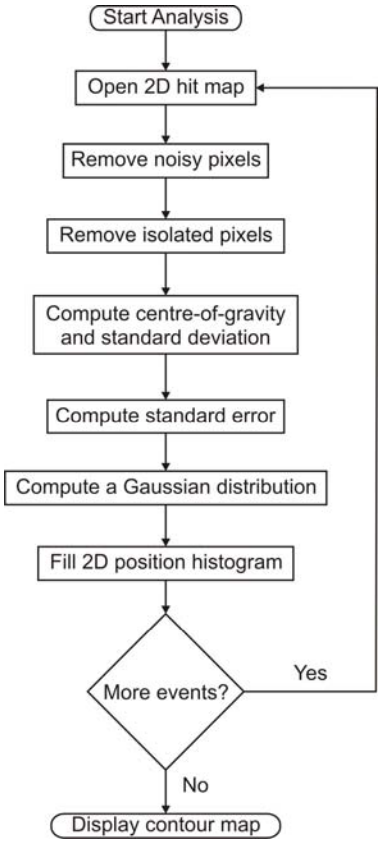

Figure 5-12 Fluxogram of the methodology used in the image reconstruction analysis.

Subsequently, a high number of single photon events results in a more accurate and better image reconstruction, as is shown in the example below.

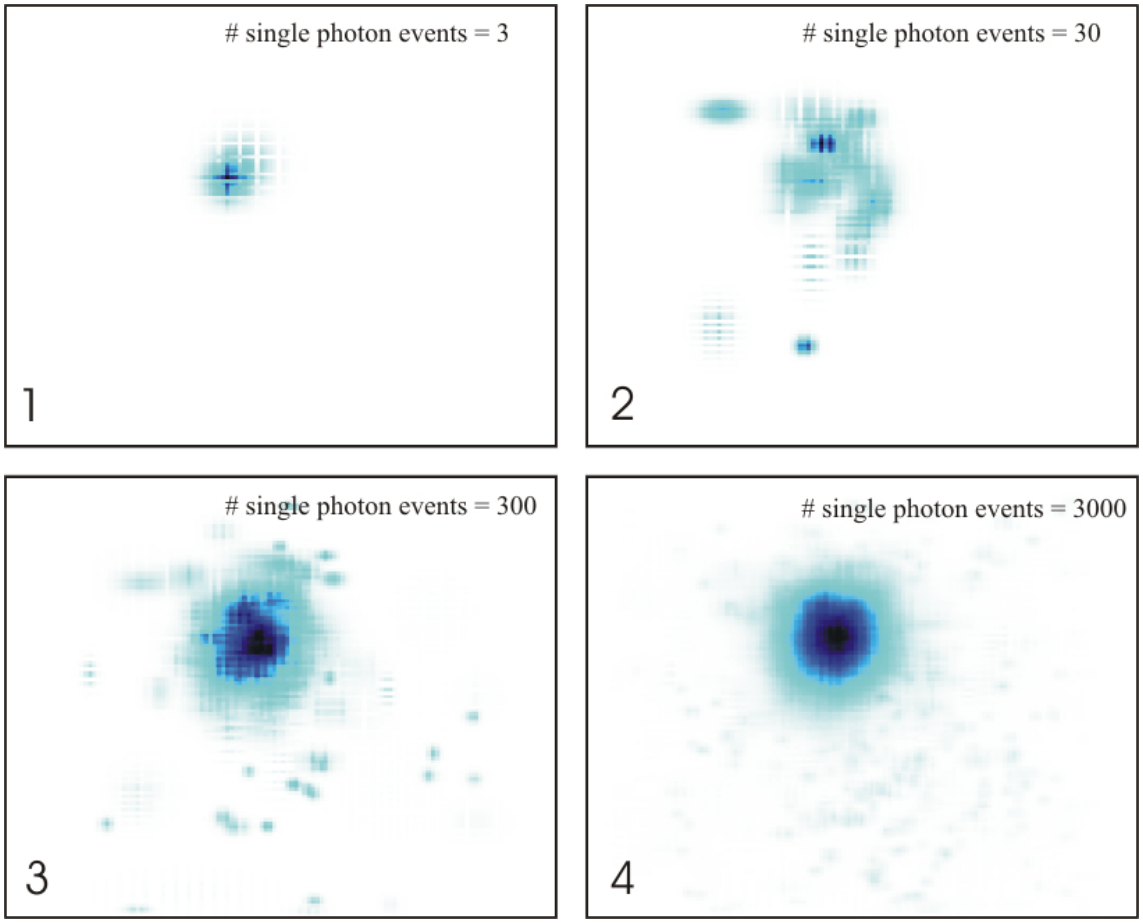

Figure 5-13: Image reconstruction of a 1 mm hole collimator, processed with a different number of single photon events.

5.3 Wide area scanning system

An electromechanical scanning system has been implemented that may be useful to produce a complete set of small 2D images and thus create an image mosaic of a larger active region. This system is not yet optimized for other particular applications besides laboratory tests, but it allows precise location measurements of the object to be imaged.

For the XY motion we use a commercial dual step motor system[1] that accomplishes motion control with a PC through parallel printer port and a custom made I/O card to sink current up to 1A required for the coils in the stepper motors. This I/O card is fed by an external +5V power supply. The XY positioning table has linear resolution of 127±1

[1] Dual step motor model XY-9 from Arrick Robotics, http://www.robotics.com

μm in both axis and in half step mode. The maximum technical scanning area is 22×22 cm^2 but for our application only a small area such as the mouse liver size (around 3 cm^2) is initially foreseen. In this system, the ISPA camera is fixed and it is the object under study that moves (Figure 5-14). To control the scanning system, a visual basic module (see Figure 5.1) has been specifically developed for our application to be implemented with the acquisition software (Figure 5-15).

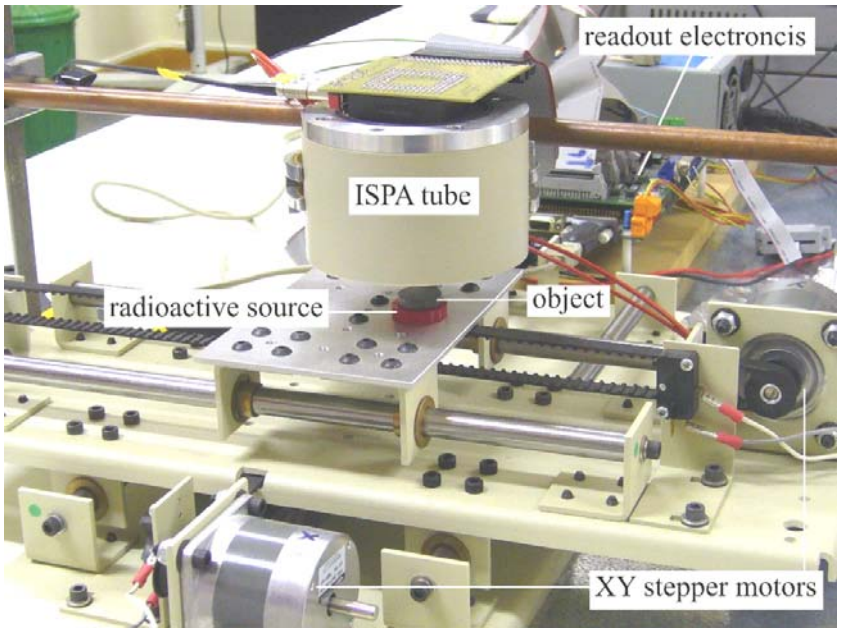

Figure 5-14: Photograph of the ISPA setup with the XY positioning table.

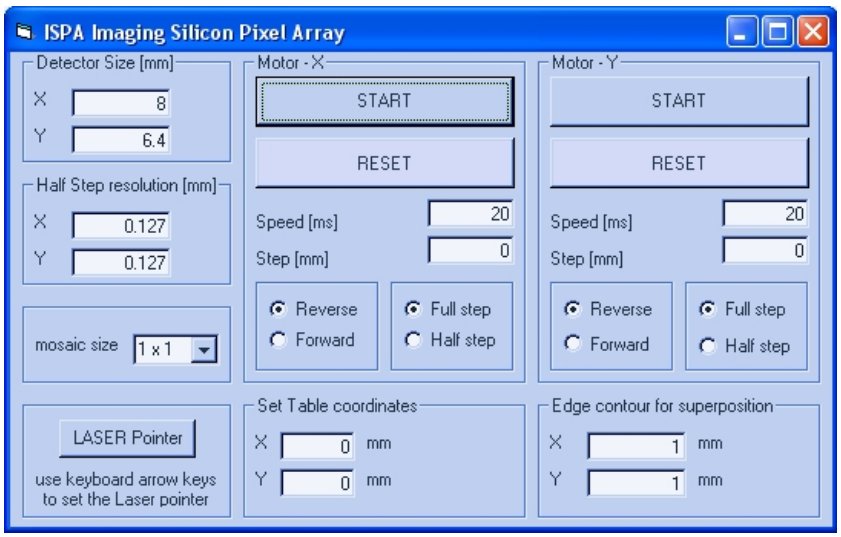

Figure 5-15: Screenshot of the XY positioning control module. This form is a call out module from the "multiple image" button on the data acquisition panel (refer to Figure 5.4). It allows setting all the parameters needed to achieve a mosaic image of multiple sizes of the detector active region. Each axis can be individually controlled with regard to its speed motor, rotational direction, step size and step mode (full/half).

To guide accurately the detector over the area to scan, we have implemented a laser pointer positioned at a fixed distance relative to the centre of the tube. From there the user can set in the software the size of the image mosaic to be captured. For a correct edge fitting of the images to get the mosaic image, the active region of the chip may be reduced leaving an edge contour for superposition. This assures that each image within a mosaic accurately aligns with adjacent images and each pixel on each mosaic corresponds to the same physical point on the target.

5.4 Summary discussion

Visual Basic was a remarkable asset in this project. The application software developed has an easy-to-use UI (user interface). At the moment real time imaging is not possible, the data analysis and the image processing are post-acquisition operations and are achieved on the PC. To explore this possibility, the mathematical calculations of the center-of-gravity of each event that lead to the reconstruction of the image, should be implemented locally in the processor of the S9007 electronic board. As referred in Chapter 4, this processor is not in use at the present. It is known that the time for the image reconstruction is strongly dependent on the RAM and the processor speed of the system where the analysis is running, and also on the complexity of the data event distribution. For our post-acquisition analysis software running on a 2.6 GHz processor, a data rate analysis between 200 and 700 events/s has been registered from some accomplished examples.

For accurate imaging position control of the ISPA-tube, we have implemented a XY table. For small area imaging of objects restrained in the active region of the detector, it reveals very useful information. However, its capabilities for wide area scanning have not yet been well explored. By acquiring multiple mosaic images and concatenating them we expect to be able to scan wider areas. The problem that arises with multiple images acquisition is time delay between them. For example in nuclear medicine, if the concentration distribution of the radiopharmaceutical in the organ under study suffers fast modifications in comparison with the acquisition time needed for each slice or each projection then the image will appear as an unmatched mosaic stack. If this concentration distribution of the radiopharmaceutical is due to the radionuclide physical or biological half-lives, the solution is solved by applying a correction factor to the intensity profile for each projection.

Chapter 6

ISPA-tube performance

The detector allows two types of acquisitions: analog and digital. The first will be used to create a trigger signal that determines whether or not to start a new digital acquisition, necessary in order to produce a precise 2-dimensional information of the same event that has generated the trigger signal. For this reason the analog signal must be faster than the digital one and the system must be well designed in order to get the right amount of data at the right time. In Chapter 4 (Readout Electronic System) we saw that a separate circuit digitalizes the analog signal on which the user can support the trigger decision based upon a specific region of interest. Only valid information will then be used for the image reconstruction. Another way to remove non-valid information without using a pre-trigger acquisition is to acquire continuously analog and digital data to memory and process it later, but this will considerably decrease the detection efficiency. In both cases the detection efficiency is optimised on calibration measurements conducted to determine the best possible performance of the ISPA system with respect to imaging. The signal to noise ratio, the threshold uniformity and the delay in the pixels are some of the parameters investigated. This chapter presents the measurements carried out at room temperature.

6.1 Laboratory setup

Figure 6-1 (left) shows the layout of the test setup. A schematic overview of the electronic boards was previously shown in Figure 4.4. This system uses 1 power supply to bias the detector, and 3 power supplies to feed the ISPA back card, the Piggy back board and the S9007 back board. An extra high voltage power supply is required when using the ISPA tube. Noise shielding is a key issue for this design which places active digital lines, analog lines and power buses in proximity to the detector. To eliminate ground loops, a grounded metallic plate covers the entire setup (Figure 6-1 right). To avoid noise induced, aluminium foils were also used to shield some of the connections.

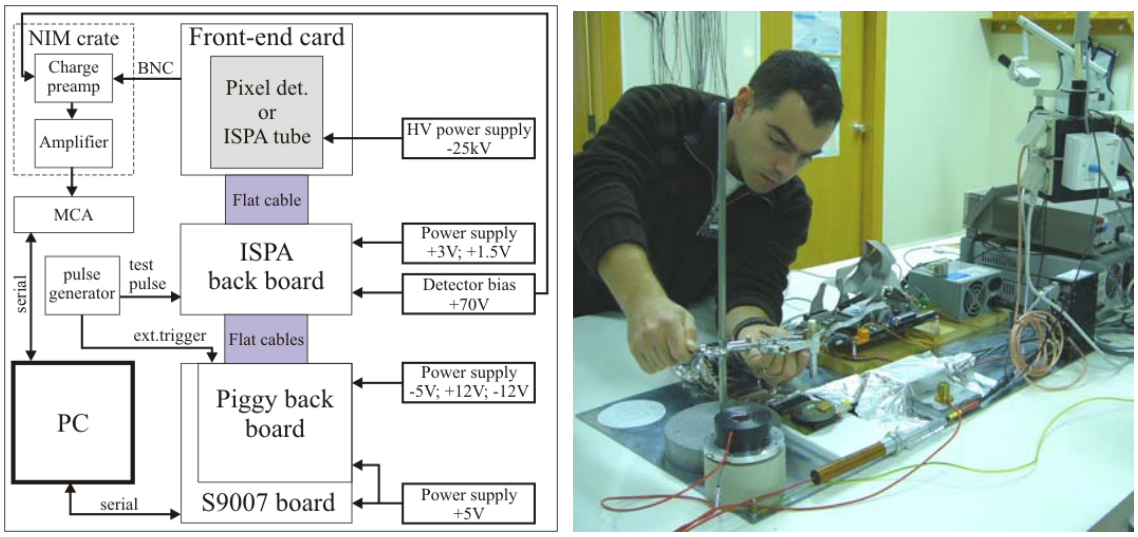

Figure 6-1: (left) Schematic overview of the laboratory setup; (right) Photograph of the setup mounted at the UALG physics laboratory. A radioactive source alignment centred on top of the test detector is being performed.

Two LHC1/Omega3 detectors were used, one sealed in the ISPA tube and one mounted on a circuit board. The first will be mostly used for analog measurements and imaging with gamma sources since it benefits from the photon-electron conversion. The second will be used for electrical test pulse measurements and imaging with a beta source (Sr-90). For comprehensibility the word *detector* refers to the silicon sensor bump-bonded on a readout chip. For analog measurement and due to the noise problems reported in Chapter 4, a second line that features NIM modules is also used. Energy spectra are acquired using a portable multichannel analyser. Table 6-1 describes the equipment models available in this setup.

Designation	**Model**	**Function**
Charge Preamplifier	Canberra model 2005 or Ortec 142[a]	Low-noise charge sensitive preamplifier for semiconductors
Amplifier	Ortec 571 or 472	pulse-height amplifier
Crate NIM	Ortec	NIM modules power supply
Multichannel analyser	Amptek Pocket MCA 8000A	16-bit ADC for energy spectrum
DC Power supply	HP E3631A	+5V for S9007 board with current protection
DC Power supply	Standard desktop PC supply	-5V; +12V; -12V for ISPA back board
DC Power supply	TT*i* EX752M	+3V; +1.5V for the chip electronics
DC Power supply	Keithley model 2400	+70V for detector bias
HV power supply	CPS 2591NEG	-25kV for the electrostatic tube
Pulse generator	Fluke PM 5786	+5V test pulse with trigger out

Table 6-1: Overview of the equipment models available in the ISPA laboratory setup.

6.2 Radioactive source measurements on silicon sensor

In order to make a first estimate of the quality performance of the silicon sensor that suffered a bump bonding process, noise estimation and measurements with radioactive sources were performed.

6.2.1 Leakage current

The detector sensor is reverse-biased, and due to the applied electric field, a small leakage current flows in the reverse direction across the diode. The value of the leakage current is of interest, because it has temperature dependence and the electronic noise increases with increasing leakage current. The Keithley 2400 source meter used to bias the detector provides a nanoampere meter. To obtain the leakage current, the test detector was characterized using I-V measurements (see Figure 6-2).

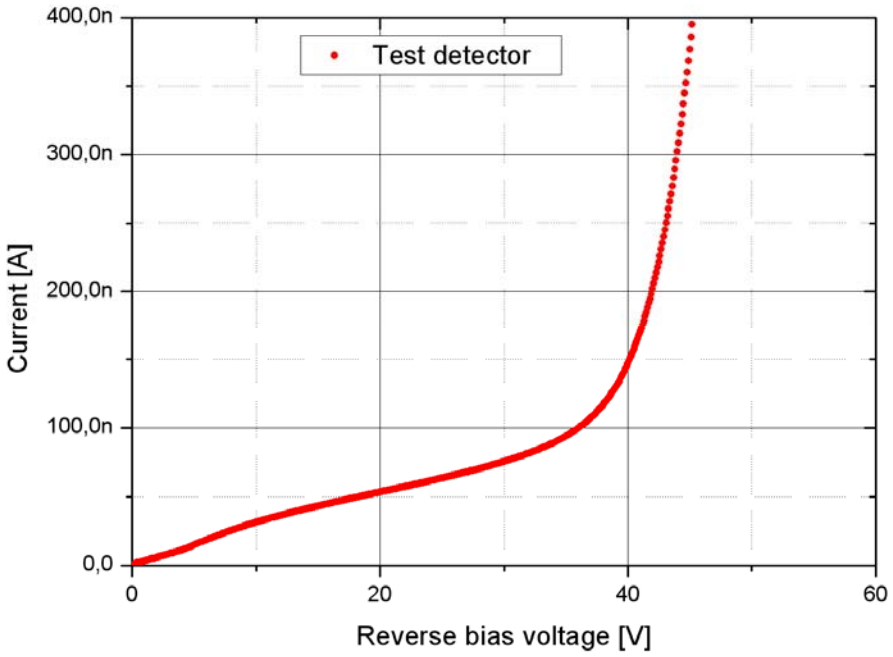

Figure 6-2: I-V characteristics of the test detector.

We found that the reverse breakdown voltage in the test detector is quite low and occurs at 35V. Below this value the leakage current is in the order of tens nA. Considering 2048 pixels, the load of leakage current per cell is extremely low.

6.2.2 Sensor depletion voltage

One technique for the measurement of the depletion voltage is using α particles. The range of 5.5 MeV α particles from an Am-241 radioactive source in silicon is about 30 μm. Directing them on the back-plane of the test detector they are detected only if the depletion region is extended from the junction over the whole detector. By increasing the bias voltage step by step and monitoring on a oscilloscope the charge signal at the output of the preamplifier, it appears stable from 15 V indicating the starting point of the plateau and thus the full depletion voltage at this value.

A second method, but much more precise is using CV (capacitance versus voltage) and RV (dynamic resistance versus voltage) measurements. The capacitance C was measured as a function of the bias voltage for a frequency of 1 kHz using the Fluke RCL meter model PM6306. The quantity $1/C^2$ was plotted as a function of the bias and the depletion voltage is determined as the intercept of the slope with a line corresponding to a capacitance adjustment. This is shown in Figure 6-3 (left) for the test detector.

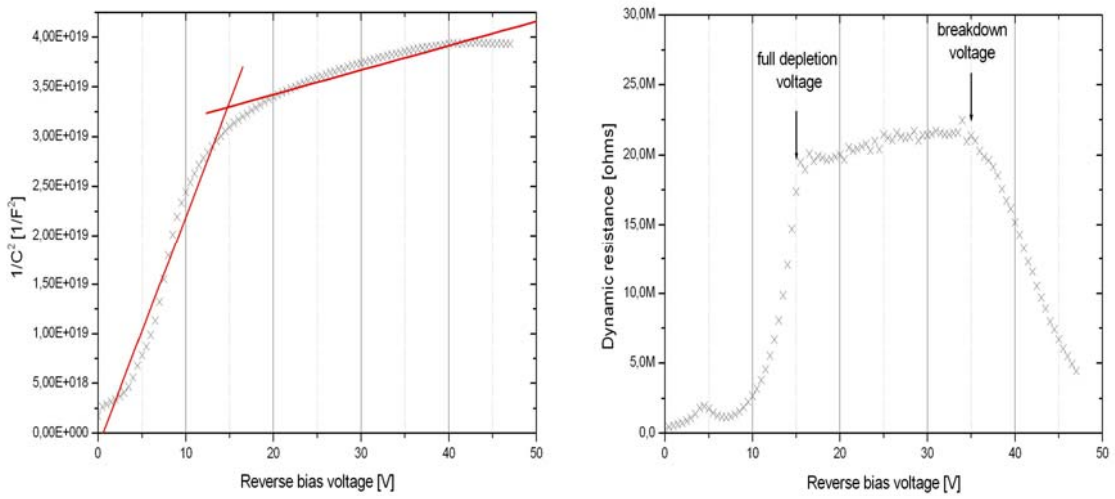

Figure 6-3: Test detector (left) CV and (right) RV measurements at 1 kHz frequency. The full depletion occurs at 15 V.

To determine the full depletion of the ISPA tube detector, this method was not successful since at the maximum applied voltage of the Fluke RCL meter (+47V) the full depletion voltage was still not reachable. Neither the first method with the Am-241 source was effective, because the tube entrance window totally absorbs α particles. Instead, using a gamma source and applying a 20 kV high voltage, the 20 keV

photoelectrons produced are stopped within the first few microns of silicon (see section 3.5.2).

A bias voltage scan (see Figure 6-4) illustrates the detector becoming sensitive at about 40 V only, corresponding to the beginning of charge collection in the back-plane region. At ~60 V the collected charges gain starts to stabilize indicating the starting point of the plateau and thus the full depletion voltage. Overdepleting the detector will not increase by much the size of the signal but it will improve charge collection at high fluence.

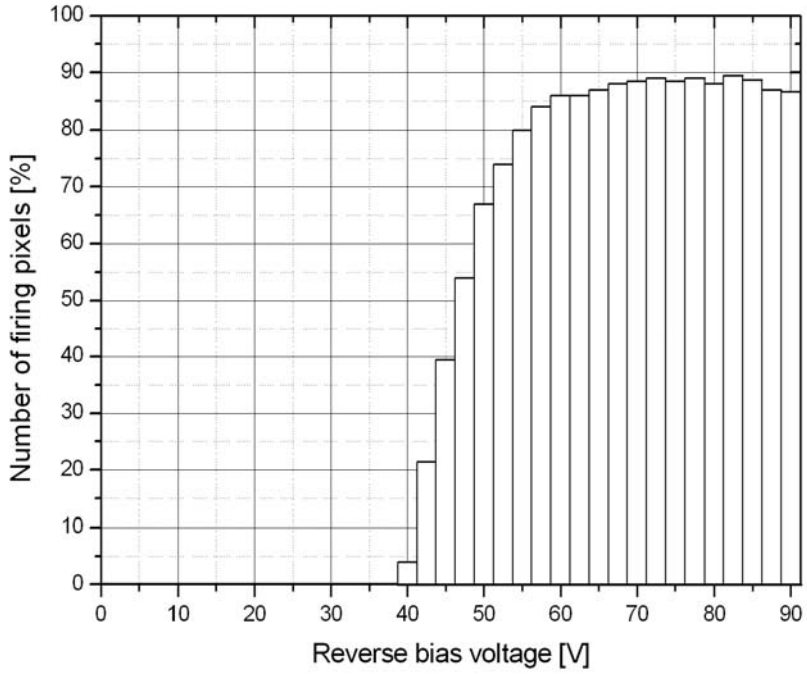

Figure 6-4: ISPA tube pixel chip response versus sensor bias voltage at 20 kV high voltage. Around 10% of the pixels are noisy or corrupted.

6.2.3 Electrostatic tube high voltage adjustment

The tube high voltage is set with the sensor fully depleted (above 60 V) and its intensity will define the number of charges generated whose value must be at a minimum above the detector offset (describe shortly in section 6.3.1) to be detected. A high voltage scan illustrates the maximum efficiency detection being reached at 20 kV (Figure 6-5). A minimum high voltage of 20 kV is then necessary to operate the tube. We record that the use of proper casing is required to insulate the external housing and to avoid electrostatic discharges.

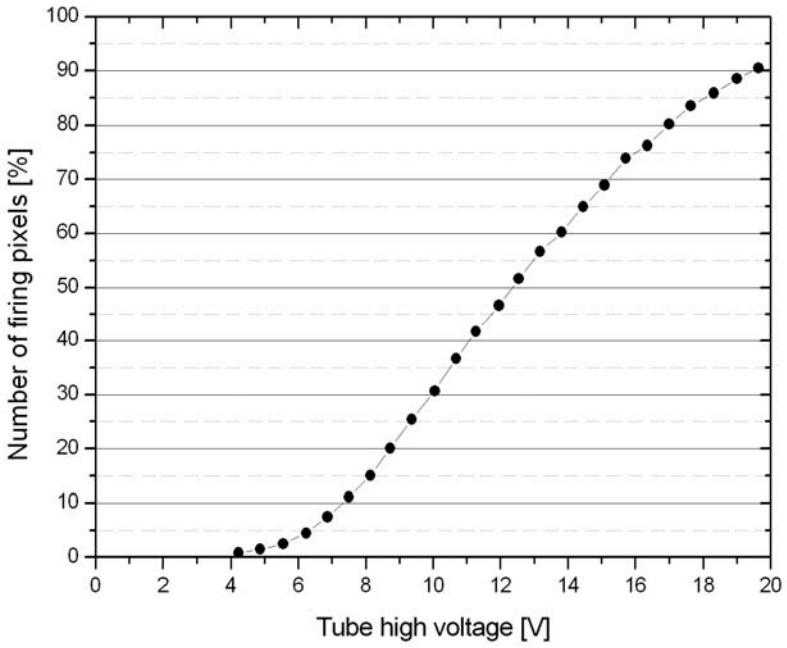

Figure 6-5: ISPA-tube pixel chip response versus high voltage applied with the sensor in full depletion mode. Around 10% of the pixels are noisy or corrupted.

6.2.4 Energy spectrum analysis

The ISPA-tube was tested using the radioactive point sources indicated in Table 6-2. The proximity tube was covered with the polypropylene shield and the tungsten collimator was removed in order to increase the detection intensity. Moreover, a 3 mm hole lead collimator (with adjustable thickness between 0.5 cm and 5.0 cm) was used to centre and focus the photons on to the entrance window.

Radionuclide	Assignment	E (keV)
Cd -109	Ag X-rays	22.1
	γ	88.0
Am-241	γ	59.5
Co-57[1]	Fe X-rays	6.5
	γ	14.4
	γ	122.1
	γ	136.5
Eu-152	Sm X-rays	39.9
	γ	121.8
	γ	244.7
	γ	(…)

Element	E (keV)
Rb	13.4
Mo	17.4
Ba	32.1
Tb	44.2

Table 6-2: (left) gamma sources; (right) Americium-241 XRF (X-ray fluorescence) source.

[1] Radioactive source provided by courtesy of the Mössbauer group at the Department of Physics, University of Algarve, Portugal.

The first analog measurements were performed with an external electronic chain consisting of an ORTEC 142A preamplifier with typical noise equivalent[2] of 1.37 keV and an ORTEC 472 spectroscopy amplifier with 0.5 shaping time and variable gain. For each source, a spectrum was recorded corresponding to the analog signal height distribution taken from the ISPA silicon chip rear contact. All the spectrums are shown on the following plots.

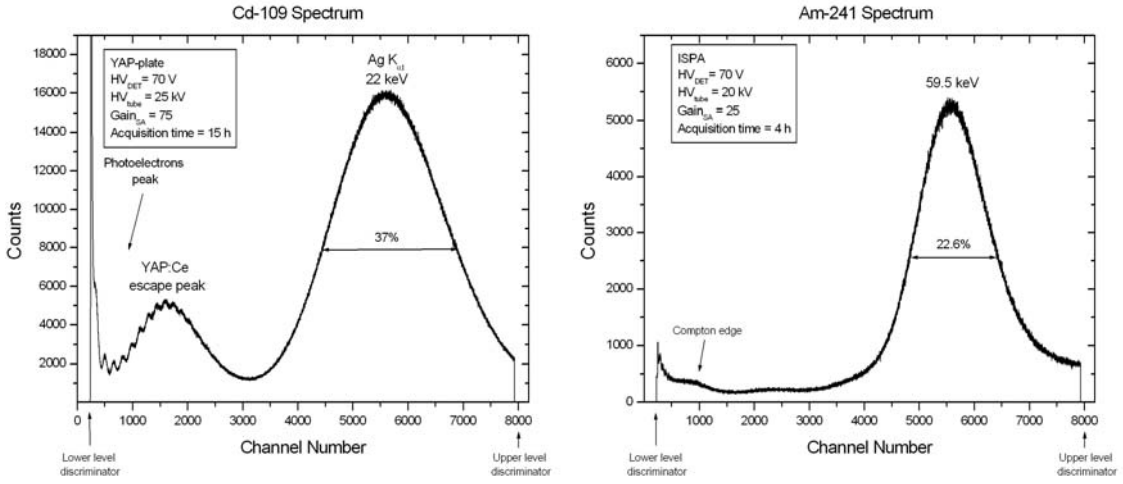

Figure 6-6: (left) Cadmium-109 spectrum. The combined X-ray peak (21.9, 22.1 and 24.9 keV) with the intensity based on the yield ratio is clearly visible. With an energy of the incoming X-rays greater than the absorption edge of the crystal scintillator, a characteristic X-ray from the YAP:Ce window is produced; (right) Americium-241 spectrum. An energy resolution of 22.6% FWHM at 59.5 keV most probable energy value was calculated.

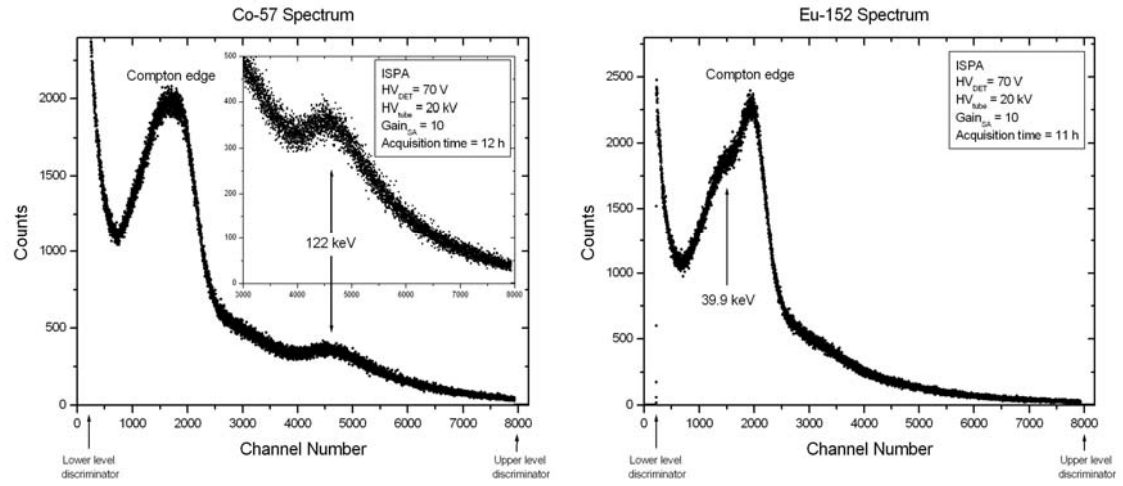

Figure 6-7: (left) Cobalt-57 spectrum of a weak source; the gamma emission line corresponding to 122 keV is located around channel 4500. Clearly visible is the Compton edge due to 122 keV photons scattering in the detector before escaping; (right) Europium-152 spectrum. A distorted shape of the combined X-ray lines (39.5 and 40.1 keV) in superposition with the Compton edge due to 122 keV photons scattering is visible.

[2] For a silicon anode capacity of 90 fF the noise of the preamplifier based on silicon equivalent of ε=3.6 eV is 1.37 keV, see model 142A preamplifier operating and service manual.

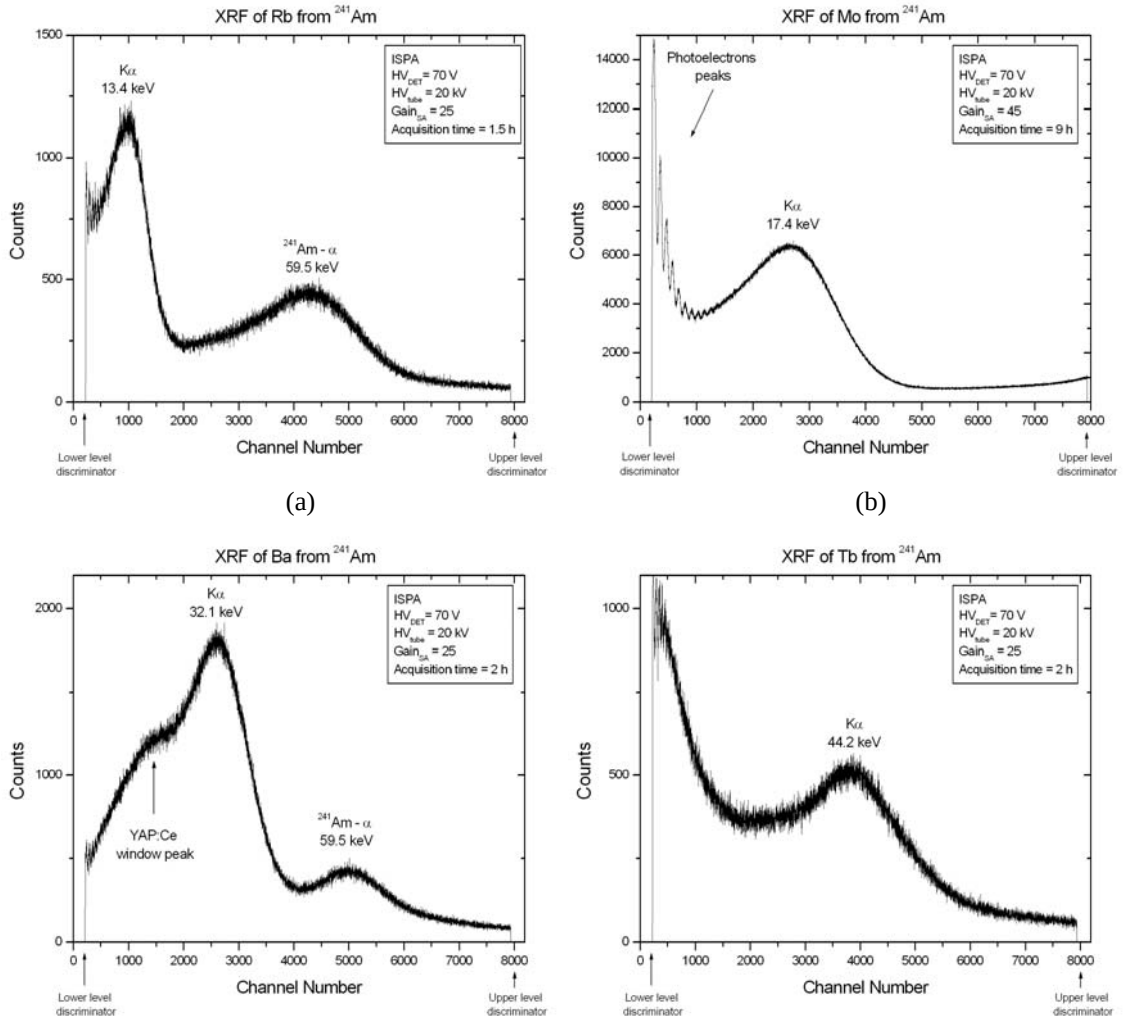

Figure 6-8: X-ray fluorescence of (a) Rubidium, (b) Molybdenum, (c) Barium and (d) Terbium. The gamma emission peak of the Americium excitation source is visible in some spectra.

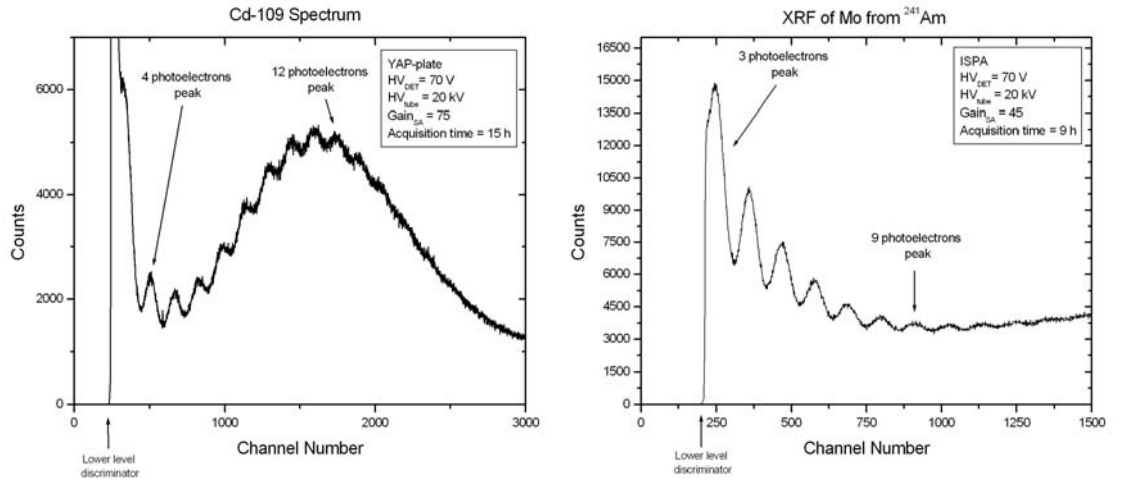

Figure 6-9: Zoom of the spectral distribution of the (left) Cd-109 radioactive source and the (right) Mo-42 XRF; Photoelectron peaks are visible with a minimum of 2 photoelectrons just above the electronic noise cut off.

The most probable energy peaks of each radioactive source were fitted with a Gaussian distribution. The main purpose of the analysis was to examine the linearity and energy resolution of the ISPA-tube. The photoelectrons peaks visible in the Cd-109 spectrum and in the X-ray fluorescence of Mo-42 (Figure 6-9) were also considered for linearity study.

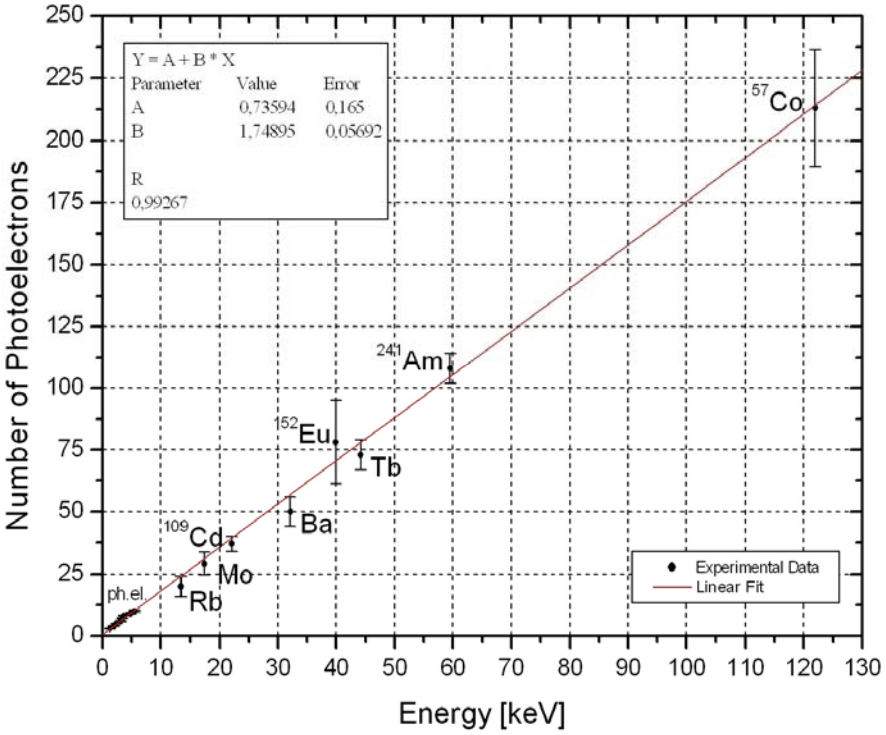

Figure 6-10: Photoelectron numbers versus the energies of total absorption peaks for several gamma and X-ray emissions.

As a gamma detector, the ISPA-tube features good energy linearity, as shown in Figure 6-10. The data are fitted with: No. of photoelectrons = 1.75 × energy [keV] + 0.74, where 1.75 means the slope in photoelectrons/keV and 0.74 the intercept with the photoelectron axis. An electron conversion efficiency of about 1.8 photoelectrons per keV was measured at the silicon anode stage.

This gamma detector also features low noise, as demonstrated in Figure 6-9. The lower level discriminator was set to cut off the electronic noise below 3 photoelectrons. With the same amplifier gain configuration, we calibrated a preamplifier test input pulse of about 2.1 mV that indicated on the multichannel analyser the signal created by a three photoelectron peak. With a preamplifier test input capacitor of 1 pF we calculate a charge input of 2×10^{-15}C corresponding to a signal of 13125 e^- for three photoelectrons and therefore 4375 e^- for one photoelectron of 20 keV.

6.3 Electrical measurements on readout chip

In the architecture of the readout electronics (Figure 3-4), we have seen that each cell is equipped at the preamplifier input with a capacitor that gives the possibility to test the electronics without using the detector. The capacitors are linked to an input pad that is called *test input*. By applying a voltage step ΔU_{test} to this test input a defined charge is injected and it is possible to test the function of the readout. The readout of the pixel array is performed with 16 shift registers at the 16 columns of 128 bits. The contents of a column are shifted towards the bottom of the chip and the clock signal has to be provided for this purpose. We use frequencies up to 12.5 MHz for this signal, so we were able to read out the chip in time of 1.28 μs. For multiple reads the data goes directly to the application software interface and our readout speed suffers from the download of the data that is limited to the serial port baud rate.

6.3.1 Detector noise offset

An important calibration measurement prior to any further application of the Omega3/LHC1 readout chip concerned the offset threshold value starting from which the readout can operate free from noise. Three noise sources are generally present, current shot noise, thermal generated current and the leakage current in electronics. So even with no test input signal, the comparator output is ambiguous.

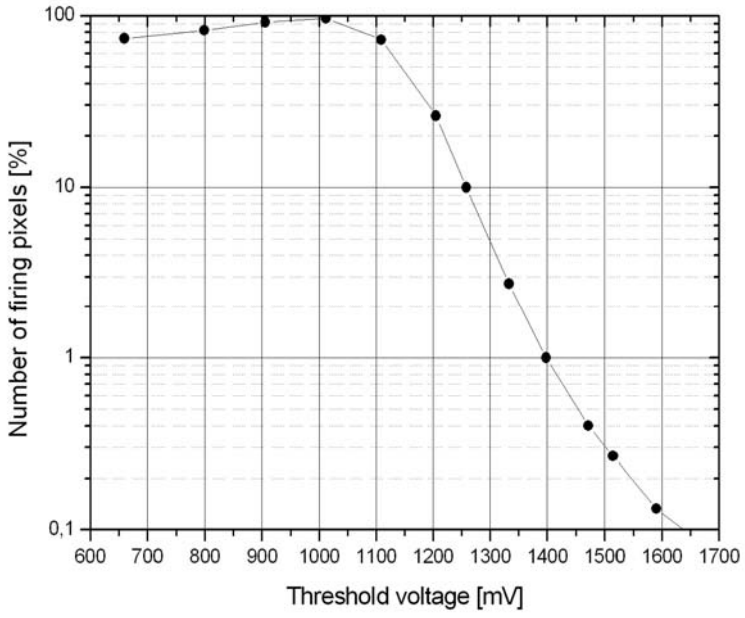

Figure 6-11: Variation of the average firing pixels as a function of the amplitude of the threshold voltage for an offset measurement at room temperature. Neither a pulse nor charge was injected at the test input.

The threshold voltage of the comparator is regulated externally and must be set above the offset value. This is done with no test input and making a random strobe readout increasing the threshold voltage until all the pixels stop responding (see Figure 6-11).

6.3.2 Timing calibration

To match the internal timing, the input signals have to be delivered with the correct delays with respect to each other and with respect to the strobe for coincidence. Figure 6-12 shows the timing diagram for the test input signal, delay output signal, strobe signal and clock out. The strobe signal has to cover the time that follows the event after the delay time. Then the pixel contents are written into the shift register cells. Secondly, the clock signal should have a low-high transition when the strobe is active. Otherwise there is some probability for a hit to be slightly out of time.

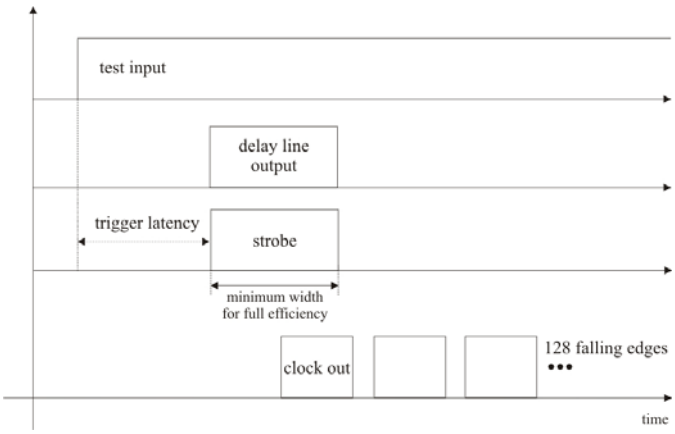

Figure 6-12: Required timing for the signals test, strobe, delay output and clock out.

The time of the delay stage that follows the discriminator in all pixels has been investigated. Starting with a large delay between input signal and strobe, this was decreased until a response to the input pulses appeared at the output. A test pulse of 5 V was used. As soon as it happened, the internal globally adjustable delay of the pixel was the same as the one between the input signal and the strobe.

As referred to in Chapter 3.6 (Readout chip), this global delay is common to all pixels and can be adjusted via the control voltage[3] V_{dl} between 1.5 and 3.3 μs, and

[3] Increasing V_{dl} we reduce the delay.

according to the trigger latency time of the application. Because the electronics behave differently from cell to cell, and to obtain even better internal delay uniformity, a 3-bit delay fine trimming individual to each pixel can be adjusted between 60 and 300 ns (V_{dla}). This fine calibration is only necessary at very high counting rates over 3 MHz defined by the strobe width. In our application, we do not reach this frequency and our detection efficiency remains unaffected by the delay trimming. For more details refer to [E. Cantatore et al., 1998].

6.3.3 Threshold measurements

A calibration is carried out to get a one to one correspondence between the threshold voltage and the number of electrons injected at the preamplifier input. The number of electrons corresponding to the test pulse can be calculated since the design value of the capacitance C_{test} at the test input is known[4]. The number of electrons is given by:

$$\#electrons = \frac{Q_{test}}{e^-} = \frac{V_{test} \times C_{test}}{e^-} \tag{6-1}$$

with $e^- = 1.6 \times 10^{-19}$ C, V_{test} in [V] and C_{test} in [F].

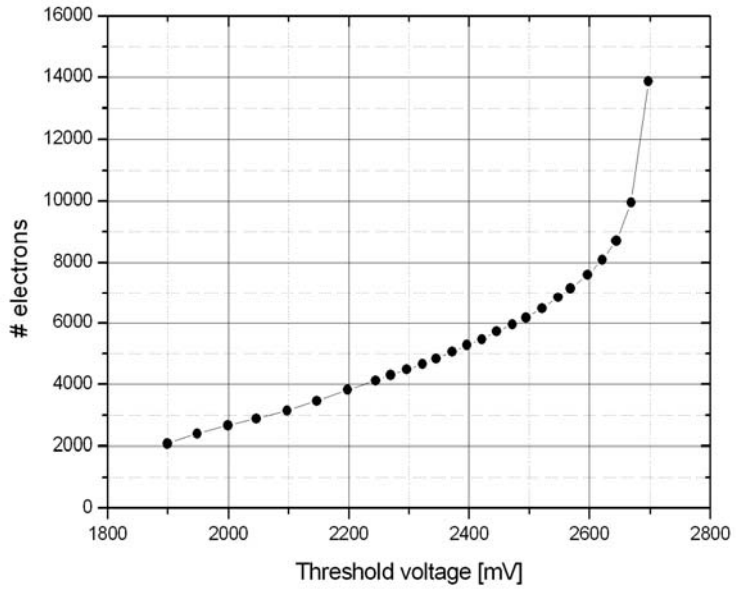

Figure 6-13: Threshold calibration measurements for an applied voltage steps at the test input of one row. Starting from the offset threshold value, the threshold is moving linearly until ~6000 e^- and then the dependence becomes exponential.

[4] The design value of the capacitance is 25 ± 1 fF. However in some measured samples the average test injection capacitance has been found to be 11 ± 3 fF [I. Ljubljana, 2000]. This is due to some variations in the production process that always result in considerable inaccuracies.

For this measurement the global threshold adjustment voltage V_{th} was changed step by step and for each of the threshold voltage settings the test pulse amplitude ΔU_{test} had to be found at which an efficiency of 50% is obtained. In Figure 6-13 the measurement for the readout cell of the tube is shown.

The efficiency is defined as the number of times a pixel cell responds divided by the number of input signals on this pixel, at a certain threshold. An ideal comparator switches exactly when a signal passes a set threshold. In practice, the applied comparator threshold as well as the input signal amplitude varies randomly around an average value, referred to as noise. As stated earlier, one type of noise is the leakage current of the electronics. This noise current in the electronics is mainly caused by fluctuations in the signal from the input to the comparator and appears to be Gaussian; and because it is symmetrically distributed, the test pulse amplitude at which a pixel cell responds by 50% to the number of applied triggers corresponds to the set threshold.

For a readout noise measurement, we keep constant the global threshold adjustment V_{th} while the amplitude of the electrical test-signal ΔU_{test} is varied. For every test pulse amplitude, we record the number of positive responses of an addressed readout cell for a constant number of applied trigger (Figure 6-14 left).

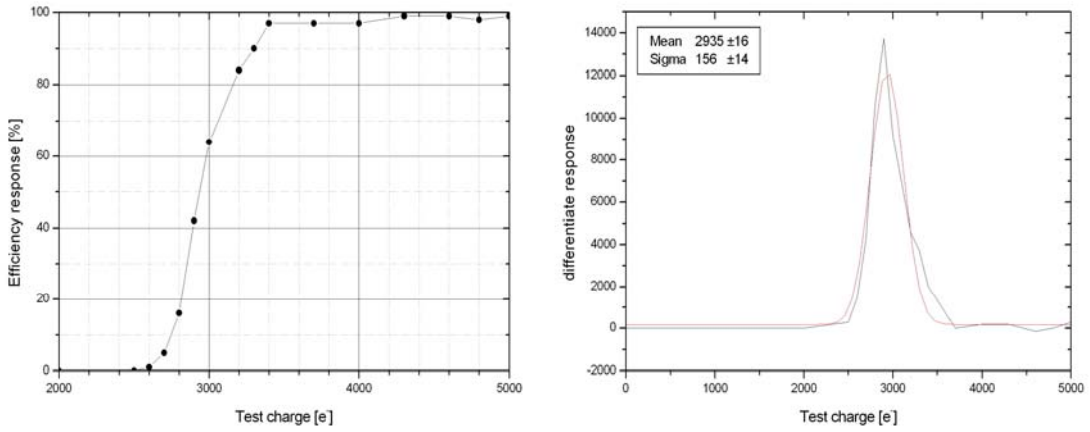

Figure 6-14: (left) test-pulse response curve of a single readout cell; (right) Numerically differentiated response curve data with Gaussian data fit.

The threshold and the noise can be alternatively obtained if the response curve data is numerically differentiated. The threshold is given by the peak and the readout noise ($ENC_{readout}$) is provided by the variance σ of an applied Gaussian fit. It means that the

difference in input test signal between 2% and 98% response corresponds to 4 σ of the cell noise distribution. Figure 6-14 (right) illustrates the Gaussian distributed and the cell noise without input signal has been found to be

$$ENC_{readout} = 156 \pm 14\ [e^-]$$

6.4 Position measurements

After a complete characterization of the ISPA tube that comprised numerical, analytical and experimental studies of the detection process, we demonstrate the ability of such a system to make 2-dimensional images. The measurements consist of locating the radioactivity of a point source with low energy gamma photons that are dispersed through a two-hole phantom. With this gamma radiography, the spatial resolution can be determined.

6.4.1 Setup procedure

Figure 6-15 shows the schematic of the position measurement setup for measuring the extrinsic spatial resolution. A 60 keV gamma energy source (^{241}Am) is placed at a distance of ~5 cm centred in front of the detector. Directly on the top of the polypropylene shield, a lead phantom with a parallel hole pattern is used for the imaging measurements described below. The lead phantom is a 5 mm-thick planar disc containing two holes of ~0.35 mm in diameter and distant of ~1 mm (the holes may be somewhat bigger and not exactly circular, since lead is very soft and therefore difficult to machine). To study the intrinsic resolution, an image is also acquired with the tungsten collimator removed and with the lead phantom placed directly on top of the crystal scintillator.

Figure 6-16 displays the pulse height distribution of the analog signal arising from the bias contact of the ISPA-tube detector chip. It represents the spectra of the ^{241}Am source calibrated in photoelectrons. The total absorption line peaks at 104 photoelectrons with 23 % FWHM energy resolution.

An important feature for the data acquisition is the setting of two discriminator levels, which define the appropriate energy window for triggering the strobe readout of the tube. The lower level discriminator (LLD) and the higher level discriminator (HLD) were set to select only the total gamma absorption peak and thus, to eliminate the

unwanted environmental and Compton background. This trigger mode becomes vital if ISPA cameras are applied in medical diagnosis where such background are present. The tuning parameters of the ISPA-tube for this test measurement are printed in Table 6-3.

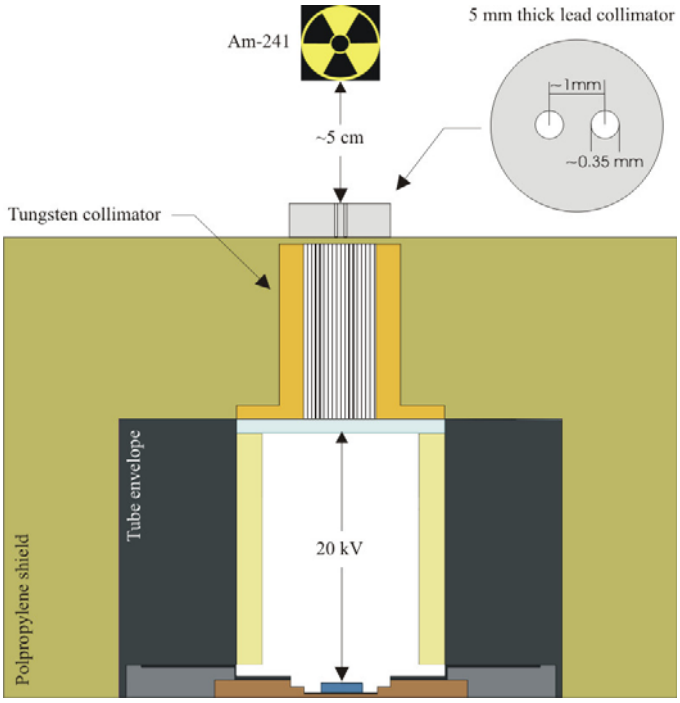

Figure 6-15: Experimental schema of the position measurement setup with details of the two-hole phantom lead collimator. With this configuration setup, the extrinsic spatial resolution can be studied.

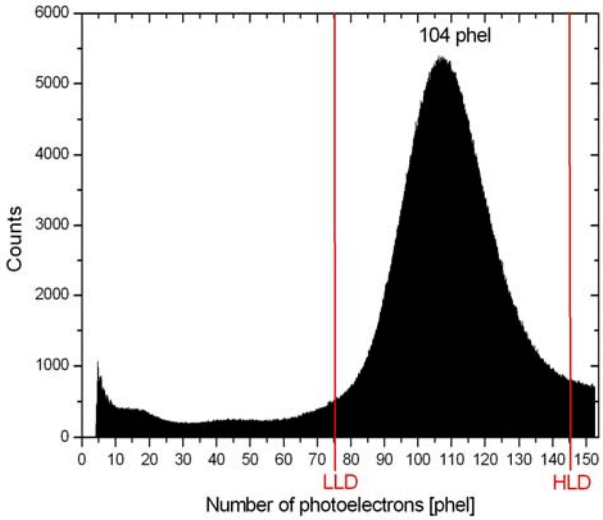

Figure 6-16: Spectrum of the ^{241}Am. The full energy peak corresponding to 60 keV centers at N_{meas} = 104 photoelectrons.

V_{Th} [mV]	V_{comp} [mV]	V_{bias} [mV]	V_{DL} [mV]	V_{DLA} [mV]	Strobe delay [µs]	Strobe width [µs]	Det bias [V]	Tube HV [kV]
1700	3300	2000	3500	3500	1250	2000	70	20

Table 6-3: Bias voltages for the tube operation.

The high voltage is the last parameter to set and must be ramped up slowly (500V/sec) to avoid electrostatic discharge. Before the acquisition readout, a mask of noisy pixels is done. The mask map is created by marking all pixels that fire on a set of random strobe acquisitions with no radioactive source. Now the system is ready to acquire an image of the two-hole phantom. For a selected 20 000 events and for each accepted gamma event, the hit pattern created on the pixel array is recorded (Figures 6.17 and 6.18 left) and its center-of-gravity calculated, together with its precision. The accumulation of the 20 000 events finally forms the image. Figures 6.17- and 6.18-right show the images that were acquired by the ISPA-tube with and without using the tungsten collimator.

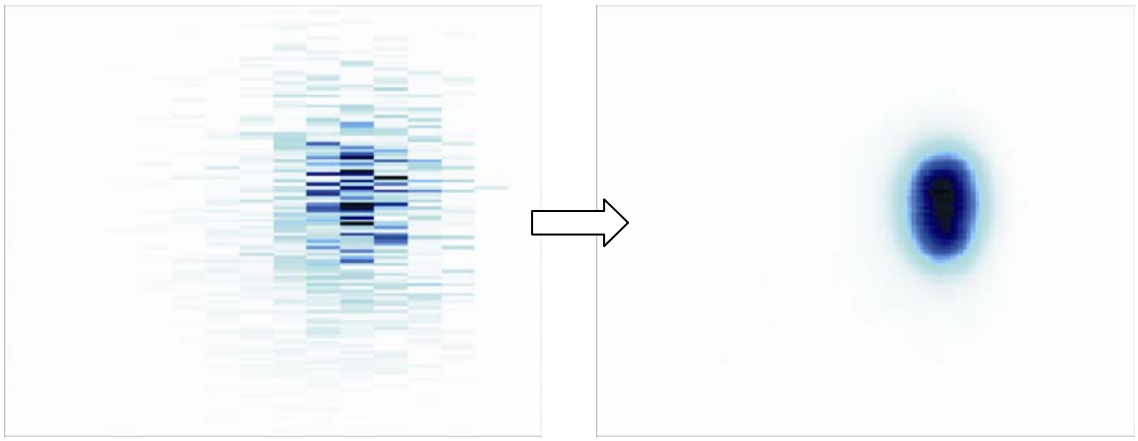

Figure 6-17: (left column) Sum of all the matrix (16 × 128) hit patterns (20 000 events) acquired using the tungsten collimator; (right column) Reconstructed image of the two-hole phantom (~0.35 mm in diameter and distant of ~1mm). The image (8.0 × 6.4 mm^2) is obtained by accumulating the center-of-gravity of 20 000 gamma events. Image pixel size: 62.5 × 50.0 μm^2.

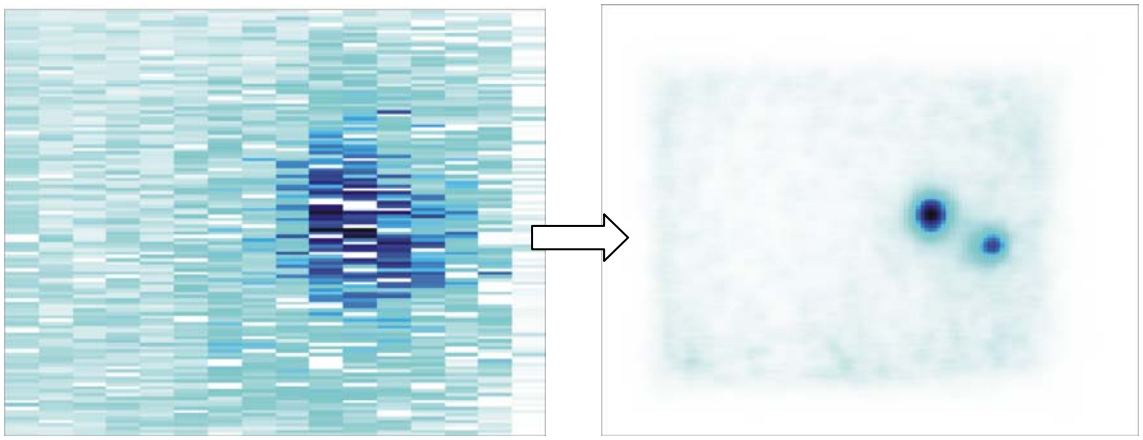

Figure 6-18: (left column) Sum of all the matrix (16 × 128) hit patterns (20 000 events) acquired without using the tungsten collimator. The phantom is placed directly on top of the crystal scintillator. The mask map of unwanted pixels that corresponds to the white pixels on the bottom image is visible. 171 pixels are registered as noisy; (right column) Reconstructed image of the two-hole phantom (~0.35 mm in diameter and distant of ~1mm). The image (8.0 × 6.4 mm^2) is obtained by accumulating the center-of-gravity of 20 000 gamma events. Image pixel size: 62.5 × 50.0 μm^2.

6.4.2 Cluster size and spatial resolution

Each gamma event produces a cluster of photoelectrons released by the photocathode (on average with number N_{phel}) and can be related to the number of firing pixels (on average with number N_{hit}). Considering the data acquisition of both images on Figures 6.17 and 6.18, the distribution of the number of firing pixel per event is plotted in Figure 6-19.

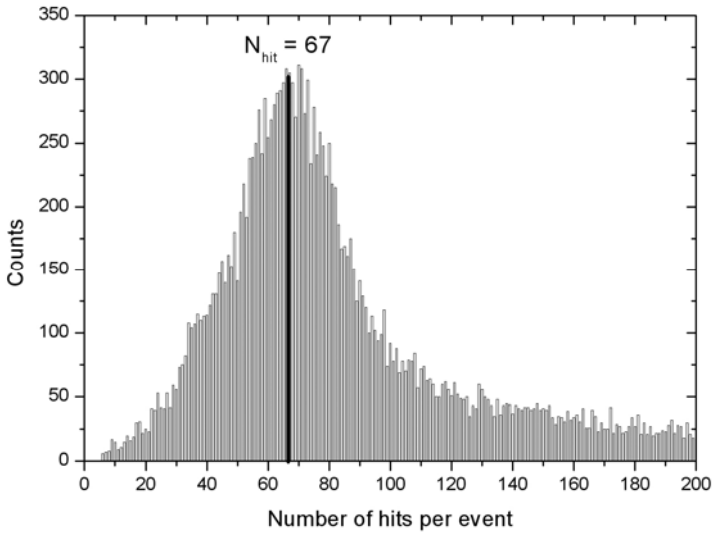

Figure 6-19: Number of hits per gamma event. The average number N_{hit} is 67 hits/event.

The resulting 20 000 event distribution yields an average number of hits per event N_{hit} = 67. This value is considerably different from the measured photoelectron N_{meas} = 104 (see Figure 6-16). This difference can be mostly explained by three factors:

- Backscattering of photoelectrons on the silicon: a percentage of the impinging photoelectrons are backscattered on the detector surface, releasing an energy lower than discriminator threshold of the pixel electronics and therefore are lost (see section 3.5.2 for a complete description).
- Overlap hits: since the pixel response is binary, two photoelectrons hitting the same pixel yield the same signal as only one.
- Charge sharing: the charge created at the detector backplane by one photoelectron can be shared between two or more adjacent pixels due to the spread occurring in the drift process resulting in a loss of efficiency.

To solve the overlap hits a bit depth in each pixel would be required. This limitation of our system introduces inaccuracy in the hit coordinates therefore a weight factor should be introduced in the calculation of the center-of-gravity.

The effect of charge sharing can be reduced by increasing the threshold voltage. A photoelectron generates 4423 e^- taking into account the backscattered energy lost (see section 3.5.2). The amount of charge collected in the pixels is proportional to the position of the photoelectron in between pixels. If the threshold increases above 2212 e^-, only the pixel with more charge will be activated longer. Thus an increasing threshold voltage will decrease the number of double hits and the cluster size will no longer be affected by charge sharing.

The cluster size is a very important parameter, its center-of-gravity determines the event hit coordinates. In addition, the distribution of the pixel residuals (relative coordinates of each firing pixel with respect to the centre of gravity) is also calculated, representing the electron cloud dimension on the pixel array for each gamma event. From the $FHWM_{res}$ of the distribution of residuals (Figure 6-20), we get an average cluster diameter of 1.7 mm.

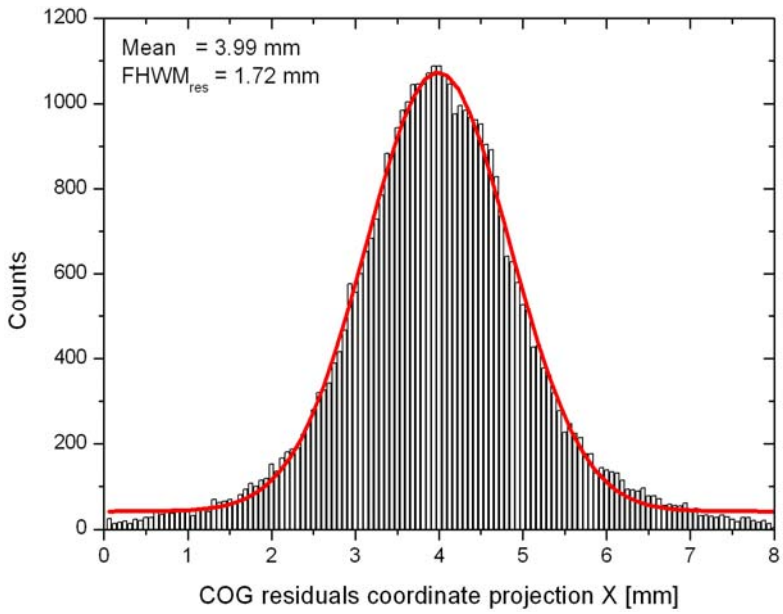

Figure 6-20: Centre of gravity residuals projection along the X-axis. The FWHM value is indicated.

Lastly, we plot the intensity profiles of the two-hole phantom images displayed in Figures 6.17- and 6.18-right, and we estimate the spatial resolution by fitting each peak with a Gaussian.

Figure 6-21 shows the intensity profile of the image acquired using the configuration setup with the tungsten collimator. From both X and Y profiles, an extrinsic spatial resolution FWHM of ~0.7 mm is measured.

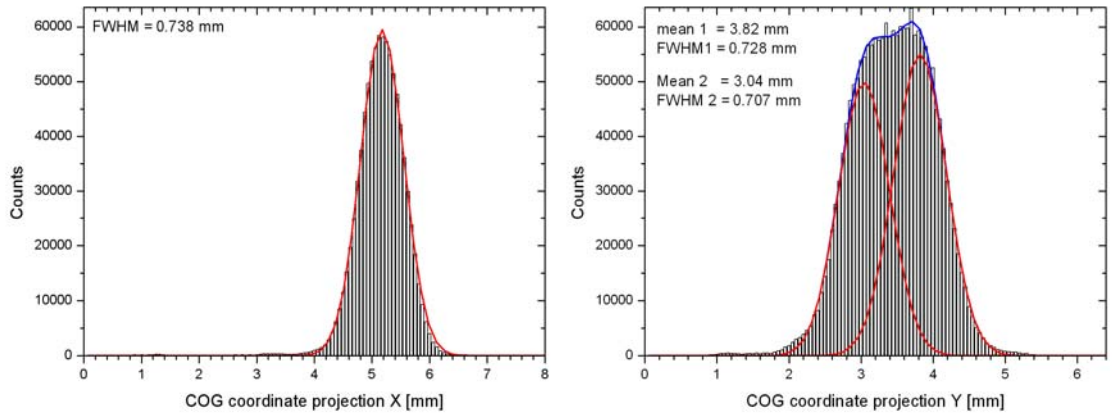

Figure 6-21: Intensity distribution of the two-hole phantom image taken along X and Y axis.

Figure 6-22 shows the intensity profile of the image acquired using the configuration setup without the tungsten collimator. We measure a distance between the two holes of ~0.9 mm and we get an average FWHM of the two holes image of ~0.350 mm. As referred to earlier, the phantom contains two holes of ~0.35 mm in diameter and distant of ~1 mm. The result is in perfect agreement with the reality. Therefore we expect that the intrinsic spatial resolution of the ISPA-tube is lower than the FWHM measured. The height difference between both peak intensities is due to non-alignment of the radioactive source with respect to their middle position. This detail related with the counting statistic in each hole affects the baseline contrast in the image contour plot and creates the visual effect of different hole sizes.

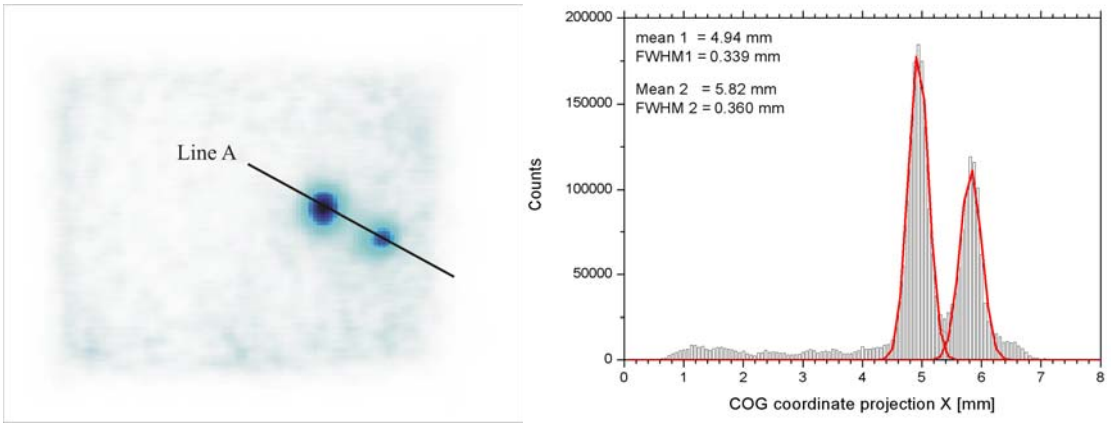

Figure 6-22: Intensity distribution of the two-hole phantom taken along line A.

6.5 Image comparison evaluation

The ISPA system is capable of acquiring conventional 2-D (planar) static images. In order to compare ISPA gamma camera potentiality with a conventional Anger camera SPECT, a phantom study was carried out to assess resolution and sensitivity detection. The lead phantom with two holes referred to earlier was used. In both cases, no collimator was used and the phantom was placed on top of the scintillator to minimize the distance between them and allow for maximum spatial resolution (Figure 6-23).

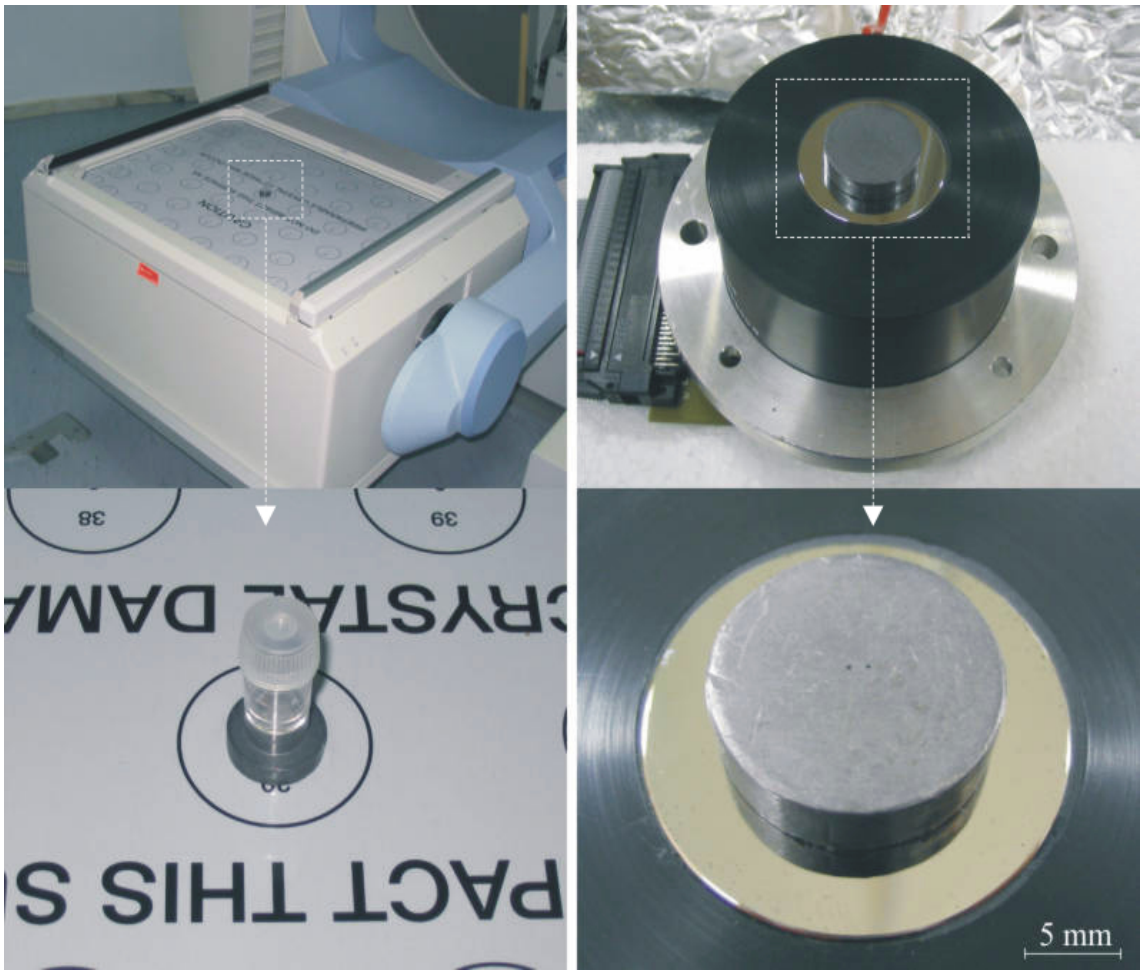

Figure 6-23: (left) Photographs of the setup using the Anger camera. The collimator is centred and aligned on top of a one of the 59 photomultiplier tubes symbolized with circle marks. A small container with the radioactive substance inside is placed on top of the collimator; (right) Photographs of the setup using the ISPA camera. The two 1 mm distant holes on the lead phantom are visible.

The first comparison of the ISPA image with a SPECT system took place at a medical facility[5]. In this procedure, a small container with a cotton ball inside soaked with technetium-99m and an activity concentration of 48 MBq (1.3 mCi) was used. The

[5] Facility provided courtesy of *Hospital Particular do Algarve*, Alvor, Portugal

energy spectrum of Tc-99m (Figure 6-24) presents a characteristic photopeak at 140 keV with 89% emission line intensity. Figure 6-25 shows the image of the two-hole phantom reconstructed from the Tc-99m window projection data when it passes through the holes. The standard clinical system presents a large field of view, 31×31 cm^2.

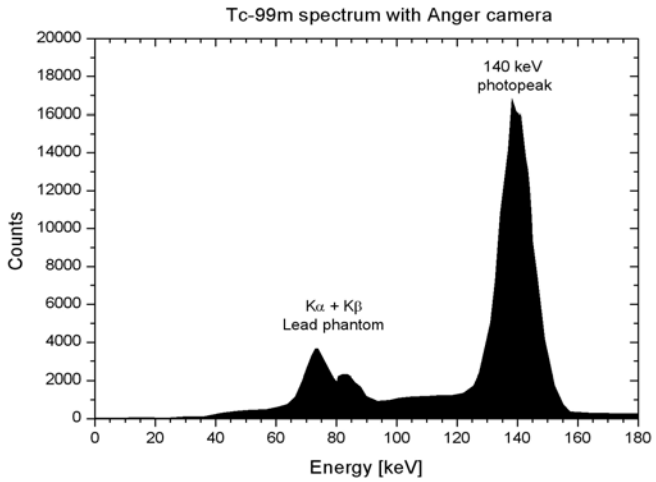

Figure 6-24: Spectrum of the Tc-99m isotope obtained with the Anger gamma camera SPECT. K-lines x-ray fluorescence of the lead phantom are visible.

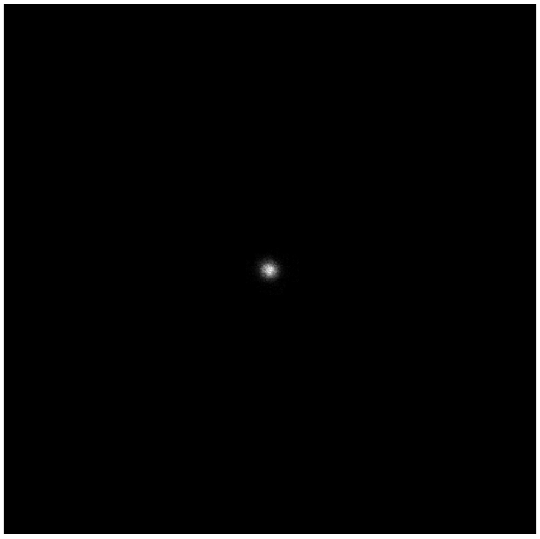

Figure 6-25: Phantom image taken with the conventional Anger camera SPECT. Image acquisition parameters: Tc-99m (48 MBq)**,** 5 minutes static, 512×512 matrix, image pixel size = 0.6×0.6 mm^2, FoV = 307.2×307.2 mm^2, counting rate = 2800 cpm.

The second comparison of the ISPA image was done with the ISPA tube at CERN's laboratory facility. Due to the impossibility at the time of getting a technetium-99m generator, one existing radioactive source in the laboratory inventory with low-energy emissions has been identified as well matched for imaging comparison with the ISPA

camera system: Cobalt-57. The Co-57 radioactive source presents two characteristic photopeaks at 122 keV and 136 keV, with 86% and 11% emission line intensities (Figure 6-26). The activity of the source was 89 MBq (2.4 mCi). Figure 6-27 shows the image of the two-hole phantom reconstructed from the Tc-99m window projection data when radiation passes through the holes.

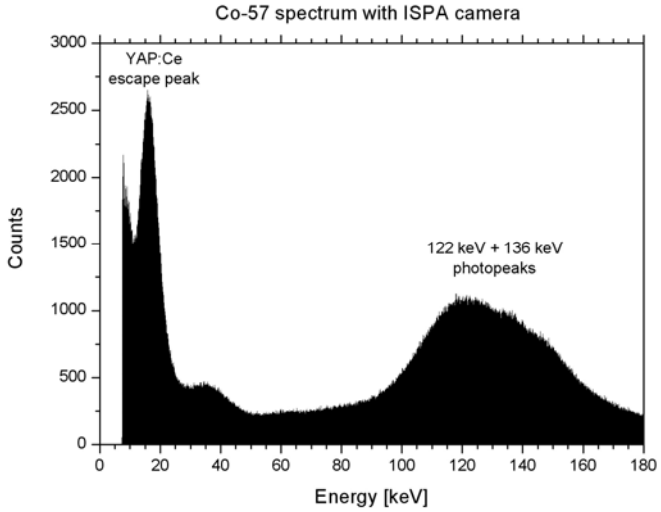

Figure 6-26: Spectrum of the Co-57 source obtained with the ISPA gamma camera.

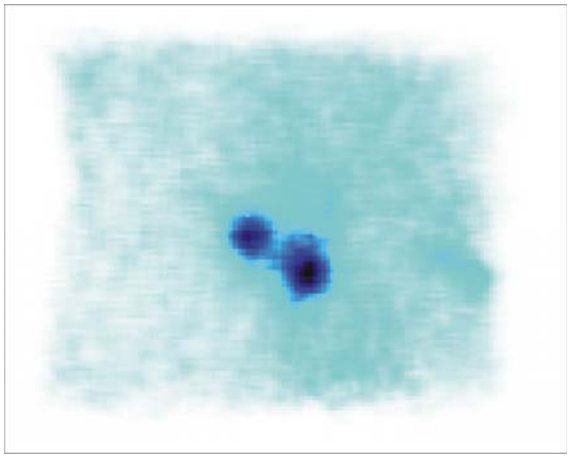

Figure 6-27: Phantom image taken with the ISPA gamma camera. Image acquisition parameters: 10 minutes static, 128 × 128 matrix, image pixel size = 62.5 × 50.0 μm^2, FoV= 8.0 × 6.4 mm^2, counting rate = 1400 cpm.

In order to compare the sensitivity detection of both systems and because radiation detection is not 100% efficient, the efficiency of the detector must be determined in order to find the relation between counts per minute in the detection system and disintegrations per minute in the radiation source**.** Due to the differences in the sources' activity and energy in both systems, an aspect that will affect the number of photons

that reach the detection system, a normalization of the ISPA image with respect to the acquisition time of the SPECT image was done. This type of normalization must take into account the photopeak energy, the absorption efficiency of the ISPA-YAP crystal and the intensity of the emission line energy. It was found that an acquisition time of 5 minutes (300s) with 48 MBq of Tc-99m in the SPECT system corresponds to approximately 2 minutes (120s) with 89 MBq of Co-57 in the ISPA system. The procedure followed to arrive at this result is described below.

The photon rate S of energy E of a radioactive point source n that reach the detector is given by

$$S_{n,E_i}\left[photons/s\right] = A_n \cdot \sum_{E_i} y_{E_i} \tag{6-2}$$

where A_n is the source activity in MBq (disintegration/second), and y_E is the intensity of the emission line of energy E (photons/disintegration). The ratio between the photon rate of the Tc-99m source and the Co-57 source gives the equivalent rate factor F_r

$$F_r = \frac{S_{\mathrm{Tc99m}}}{S_{\mathrm{Co57}}} = \frac{A_{Tc99m} \cdot y_{140\mathrm{keV}}}{A_{\mathrm{Co57}} \cdot \left(y_{122\mathrm{keV}} + y_{136\mathrm{keV}}\right)} = \frac{48\mathrm{MBq} \cdot 89\%}{89\mathrm{MBq} \cdot \left(86\% + 11\%\right)} = 0.5 \tag{6-3}$$

Since the absorption efficiency of the ISPA scintillator crystal is energy dependent (Figure 3.7), a correction factor F_{YAP} regarding the number of incident photons that will interact with the detection system must be introduced. For 122 keV and 136 keV gamma ray photons, around 35% of the incident photons will be absorbed in the crystal and for 140 keV photons the absorption percentage is 28 %. The correction factor is then

$$F_{YAP} \approx \frac{28\%}{35\%} \approx 0.8 \tag{6-4}$$

The equivalence between the two sources and therefore the acquisition time correction factor between both systems under comparison, conventional SPECT and ISPA cameras, is thus obtained by multiplying F_r by F_{YAP}

$$t_{ISPA,Co57} = t_{SPECT,Tc99m} \cdot F_{YAP} \cdot F_r = 5\mathrm{min} \cdot 0.5 \cdot 0.8 = 2\mathrm{min} \tag{6-5}$$

This way, 5 minutes acquisition with 49 MBq of Tc-99m in the SPECT system is equivalent to 2 minutes acquisition with 89 MBq of Co-57 in the ISPA system. Figure 6-28 shows the normalized images for the final comparison. Both images are represented in the same scale and with a field-of-view of 20 × 20 mm^2. The total number of gamma events detected is 14000 counts for the SPECT system and 2800 counts for the ISPA system.

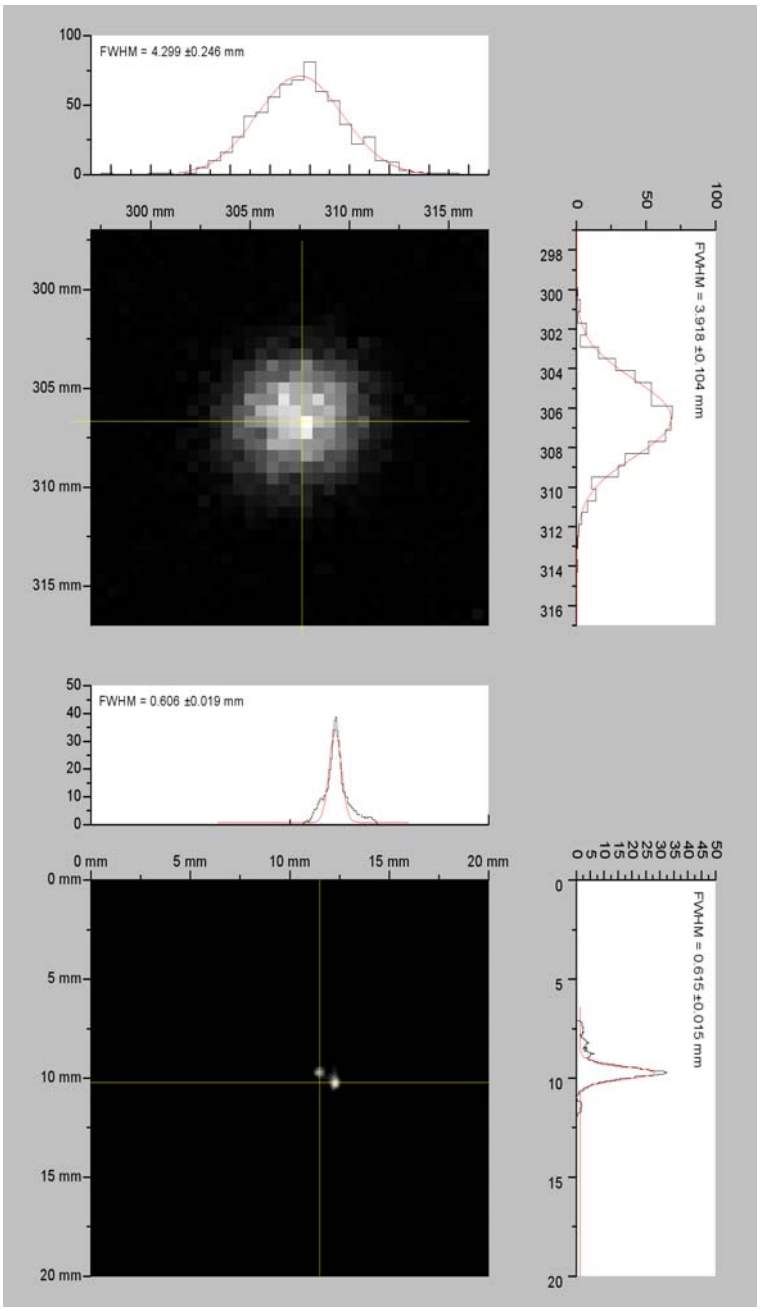

Figure 6-28: Image comparison between (top) a standard Anger camera (NaI) and (bottom) the ISPA-tube. Data are produced by using a two-hole lead phantom of ~0.35 mm distant of ~1 mm. Collection times are 5 minutes equivalent. The number of gamma events detected is 14000 counts for the SPECT system and 2800 counts for the ISPA system. Note that the profile intensities in X- and Y- axis of the two images are not related to single gamma events.

6.6 Summary discussion

A full characterization of the ISPA-tube has been completed in order to calibrate the absolute detection efficiency of the detector. Radioactive source and electrical test measurements have resulted in the tuning parameters presented in Table 6.3. A tube high-voltage of 20kV and a detector bias of 70V are recommended. With the detector in full depletion mode, a 20 keV photoelectron produces a charge signal of 4375 e^-. This result is consistent with the simulated value (4423e^-) obtained at the silicon anode (see section 3.5.2 – Photoelectron response). The electronic noise per readout cell was found to be 156e^-.

The ISPA-tube presents good linearity over the range assayed (from few keV to 122 keV). An electron conversion efficiency of about 1.8 photoelectrons per keV was measured at the silicon anode. This result could be in good agreement with the expected number of photoelectrons released by the photocathode achieved from simulations (1.6 phe/keV), if we do not consider the backscattering effect. Due to their backscattering onto the silicon anode, the number N_{phe} of photoelectrons released by the photocathode differs from the number N_{meas} of counted photoelectrons, that is

$$N_{meas} \approx 0.81\, N_{phe} \Leftrightarrow N_{phe} \approx 1.2\, N_{meas} \tag{6-6}$$

This means that the average energy absorbed in the silicon anode corresponds to 81% of the initial photoelectron energy, and thus, this relation is also valid if we consider the number of photoelectrons per keV, which results in the following relation:

$$N_{phe}/keV \approx 1.2\, N_{meas}/keV \approx 1.2 \times 1.8\ phe/keV \approx 2.2\ phe/keV \tag{6-7}$$

This result suggests that the YAP:Ce crystal implemented in the ISPA-tube, presents an intrinsic light output higher than 10000 ph/MeV as first considered and defined in the simulation conditions.

From 60 keV gammas of an ^{241}Am source, we measured a total absorption peak N_{meas} of 104 phe. From Equation 6.6, and taking the backscattering into account, the number N_{phe} of photoelectrons released by the photocathode corresponds to 128 phe. According to [C. D'Ambrosio and H. Leutz, 2000] the $FWHM_E$ energy resolution in hybrid photodetector tubes is given by

$$FWHM_E = 1.043 \cdot \frac{2.36 \cdot N_{meas}}{\sqrt{N_{phe}}} = 23\% \quad (6\text{-}8)$$

This result is in perfect agreement with the value measured (see Figure 6.6 right).

Following, we get an average number of hit pixels per 60 keV gamma event of N_{hit} = 67, distributed in an average cluster diameter of 1.72 mm. The average number N_{pix} of pixels involved in the photoelectron cluster is equal to

$$N_{pix} = \frac{\pi \cdot 0.86^2}{0.05 \cdot 0.5} \cong 93 \quad (6\text{-}9)$$

where 0.05 × 0.5 mm^2 means the area of one pixel. Compared with the measured number of hit pixels N_{hit}, several pixels are being hit by two or more photoelectrons, giving the same signal as for one hit. Finally, taking into account the average number N_{hit} and the $FHWM_{res}$ of the distribution of the pixel residuals (Figure 6-20), we get the intrinsic spatial resolution of the ISPA tube for 60 keV gamma photons,

$$FWHM_{ISPA} \cong \frac{FWHM_{res}}{\sqrt{N_{hit}}} \cong \frac{1.72\,mm}{\sqrt{67}} \cong 0.210\,mm \quad (6\text{-}10)$$

According to this relation, the spatial ISPA resolution improves with N_{hit}. When N_{hit} approximates to N_{pix} we get the limiting resolution of the ISPA tube,

$$FWHM_{ISPA} \cong \frac{FWHM_{res}}{\sqrt{N_{pix}}} \cong \frac{1.72\,mm}{\sqrt{93}} \cong 0.178\,mm \quad (6\text{-}11)$$

With analogue (or two bits) response for the pixels, the spatial resolution would not be limited by the number of hit pixels. When coupling the ISPA-tube with the parallel hole rippled-foil tungsten collimator, the total spatial resolution is ~0.7 mm.

To evaluate the potentiality of the ISPA camera in nuclear medicine imaging in association with a standard SPECT gamma camera, a two-hole phantom image was acquired and compared in both system. The results obtained indicate that the resolution

of the ISPA camera is better than a standard SPECT gamma camera by approximately a factor of 7 times higher, moreover achieving sub-millimeter resolution. With a larger statistical counting and an Am-241 radioactive source, a FWHM resolution of 0.35 mm was achieved, corresponding to the size of the hole diameter of the lead phantom used. However, direct comparison of the results obtained indicates that the SPECT camera provides superior efficiency than the ISPA camera (more than 5 times larger). The low collection efficiency of the ISPA camera will certainly limit the contrast sensitivity of the system and thus limit its use in applications that require low doses.

References

[C. D'Ambrosio and H. Leutz, 2000] C. D'Ambrosio and H. Leutz, **Photoelectrons backscattering from silicon anodes of hybrid photodetector tubes**, IEEE Trans. Nucl. Sci., Vol. 47, 1685-1690, No. 4, 2000.

[E. Cantatore et al., 1998] E. Cantatore et al., **Uniformity of response of the LHC1 large area pixel detector system**, *Nucl. Instr. Meth. In Phys. Res. A* 409, 119-128, 1998.

[I. Ljubljana, 2000] I. Ljubljana, **An investigation of silicon pixel tracking detectors and their application in a prototype vertex telescope in the CERN NA50 heavy-ion experiment**, Ph.D. Thesis, Bergische University of Wuppertal, WUB-DIS 99-20, 2000.

Chapter 7

Discussion and Conclusion

7.1 Conclusion

A small planar imaging system was developed in the framework of the ISPA collaboration at CERN in view of the application in molecular and small-animal imaging. At present, this system consists of a hybrid photodetector, the ISPA-tube (with the Omega3/LHC1 chip), coupled to a tungsten rippled foils collimator and controlled by readout FPGA logic. The system is compact and hand held. The readout system is not yet suited for full operation with the ISPA-tube, however, it proved to be an excellent tool to study the imaging performance of the ISPA-tube together with the old NIM readout system. The measurements carried out with low-energy photons showed an extrinsic spatial resolution (collimator + ISPA-tube) of 0.7 mm FWHM. Without the collimator, the intrinsic spatial resolution appears to be 0.2 mm based on a centroid position estimation method. An energy resolution of 23% FWHM @60 keV and a photon-to-electron conversion efficiency of about 1.8 per keV was measured at the silicon anode. The measurements done are in almost perfect agreement with simulations. One imaging application of the gamma camera has demonstrated its usefulness in low-energy imaging and it has been able to produce small planar images, with a good spatial resolution, higher comparable with planar SPECT ones. However its main limitations are imposed by the low detection efficiency and the small FoV (8×6.4 mm^2). The present readout frequency implemented in the FPGA logic is responsible for this low detection efficiency. By solving the readout electronic crosstalk noise and increasing the speed of the programmable logic significant improvements can be made, and the system can meet the requirements of higher counting rate application. The small FoV can be overcome by using a scanning system. Still, it is only effective for science research facilities that require high resolution imaging down to submillimeter and not for medical diagnosis where acquisition time is limited.

7.2 Scientific research contributions

The work presented in this thesis on behalf of the ISPA Collaboration at CERN has led to the production of scientific reports, public presentations and papers in the past 5 years that are stated below in chronological order:

- **A high resolution imaging detector for nuclear medicine**
  C. Abreu, P. Rato Mendes, P.Sousa; BioEng´2001 – 6th Portuguese Conference on Biomedical Engineering, Faro, Portugal, June 2001

- **A compact, high resolution camera for nuclear medicine**
  C. D'Ambrosio, C. Ortigão, E. Rosso, F. Cindolo, L. Peralta, M. Abreu, P. Rato Mendes, P. Sousa; 12th General Conference of the European Physical Society, EPS-12 P1-167-C, Budapest, Hungary, August 2002.

- **Uma Câmara Gama de Alta Resolução para Medicina Nuclear**
  M. C. Abreu, C. Ortigão, L. Peralta, P. Rato Mendes, P. Sousa; SPF 2002 – Sociedade Portuguesa de Física, Évora, Portugal, September 2002.

- **Gamma spectroscopy and optoelectronic imaging with hybrid photon detector**
  C. D'Ambrosio, M. Abreu, V. Cencelli, F. Cindolo, F. De Notaristefani, H. Leutz, J. Mares, M. Nikl, D. Piedigrossi, D. Puertolas, P. Rato Mendes, E. Rosso, P. Sousa; Nucl. Instr. Meth. in Phys. Res. A 497, p. 186-197, 2003.

- **Readout electronics development for the ISPA-tube**
  M. Abreu, C. D'Ambrosio, V. Cencelli, F. Cindolo, F. De Notaristefani, C. Ortigão, L. Peralta, P. Rato Mendes, E. Rosso, P. Sousa; BioEng'2003 – 7th Portuguese Conference on Biomedical Engineering (Poster), Lisbon, Portugal, June 2003.

- **A Monte Carlo study of a YAP:Ce γ-camera**
  M. C. Abreu, C. D'Ambrosio, C. Ortigão, L. Peralta, P. Rato Mendes, E. Rosso, P. Sousa; BioEng'2003 – 7th Portuguese Conference on Biomedical Engineering, Lisbon, Portugal, June 2003.

- **Further developments on a nuclear imaging system with an ISPA-tube**
  M. C. Abreu, C. D'Ambrosio, V. Cencelli, F. Cindolo, F. De Notaristefani, C. Ortigão, L. Peralta, P. Rato Mendes, E. Rosso, P. Sousa; 9th IPEM (Institute of

Physics and Engineering in Medicine) Annual Scientific Meeting, University of Bath, England, September 2003.

- **A Monte Carlo Study of a YAP:Ce gamma-camera coupled to an ISPA tube**
  M. C. Abreu, C. D'Ambrosio, C. Ortigão, L. Peralta, P. Rato Mendes, E. Rosso, P. Sousa; 9th IPEM (Institute of Physics and Engineering in Medicine) Annual Scientific Meeting, University of Bath, England, September 2003.

- **Further readout electronics development for the ISPA gamma camera**
  M. C. Abreu, V. Cencelli, F. Cindolo, E. D'Abramo, C. D'Ambrosio, F. De Notaristefani, G. Hull, H. Leutz, C. Ortigão, L. Peralta, P. Rato Mendes, E. Rosso, P. Sousa; Nuclear Science Symposium Conference Record, 2003 IEEE Volume 4, Page(s):2335 - 2338, October 2003.

- **Analog tests of the new ISPA-tube readout system**
  M. C. Abreu, V. Cencelli, F. Cindolo, E. D'Abramo, C. D'Ambrosio, F. De Notaristefani, G. Hull, H. Leutz, C. Ortigão, L. Peralta, P.R. Mendes, E. Rosso, P. Sousa; Nuclear Science Symposium Conference Record, 2004 IEEE Volume 7, Page(s):4182 – 4184, October 2004.

7.3 Future developments

It is clear that, the technology advancments associated with particle detection nowadays makes any innovate electronic system design obsolete in less than two years. However, the flexibility of dedicated readout system can prolong its application. For instance, the architecture of the ISPA readout electronic system is prepared to adapt to a new ASIC (Application-Specific Integrated Circuit) chip under development at INFN laboratories and is also prepared to adapt to the so expected ALICE-chip[1] (developed by the microelectronics group at CERN). On August 2006 we received a new ISPA-tube prototype that features the ALICE-chip. It was built by the number one supplier of image intensifier devices in Europe, Delft Electronic Products B. V. (DEP). The chip was successfully tested with the LHCb test setup. The ALICE-chip is faster and presents an active region 3 times larger than the Omega3 chip. It will improve the detection efficiency and increase its utility in other research and medical applications.

[1] ALICE – A Large Ion Collider Experiment at CERN LHC; http://aliceinfo.cern.ch/index.html

One of the initial proposed goals was to complete in four years an imaging system that fulfils authorized requirements to work in a clinical environment, but a lot of unexpected delays associated with the electronics emerged. This idea is definitively not put aside as the Collaboration continues. Alternatively, it can be used and implemented in the research laboratory just like it has been so far. Only position measurements with point sources were achieved, and it is indispensable to test the system with radioactive phantoms with arbitrary source distribution. It will then be possible to explore the potential of this system for different applications.

Once the readout electronic system is ready to adapt the new ISPA prototype (with the ALICE-chip), the next step to achieve is focused on programming the DSP available on the S9007 board to perform real-time data analysis and thus, real-time imaging foreseeing dynamic images. After, a proper product design solution for the system appearance can be considered.

7.4 Partnership

The accomplishment of this prototype was made by the extent of the collaboration among the investigation laboratories of LIP (*Laboratório de Instrumentação e Física Experimental de Partículas)*, Lisbon, the UALG-FCT (Faculdade de Ciências e Tecnologias da Universidade do Algarve), Faro, the Technical Assistance group 2 (TA2) at CERN (*Centre Euopéen de Recherche Nucleaire*), Geneva, and the INFN-Roma 3 (*Institute Nazionale de Fisica Nuclear/Università di RomaTtre*), Rome.